Title
Development of novel bispecific antibody modalities for targeted degradation and anti-viral therapeutic applications

Author
Pance, Katarina

Publication Date
2021

Peer reviewed|Thesis/dissertation

Development of novel bispecific antibody modalities for targeted degradation and anti-viral therapeutic applications

by
Katarina Pance

DISSERTATION
Submitted in partial satisfaction of the requirements for degree of
DOCTOR OF PHILOSOPHY

in

Chemistry and Chemical Biology

in the

GRADUATE DIVISION
of the
UNIVERSITY OF CALIFORNIA, SAN FRANCISCO

Approved:

DocuSigned by:
Jim Wells
5F2F4D1A06164C2...

Jim Wells
Chair

DocuSigned by:
Jason Gestwicki

Jason Gestwicki

DocuSigned by:
Aashish Manglik
4C1E8A184D2E493...

Aashish Manglik

Committee Members

This work is dedicated to my parents, Aleksandar and Gordana, who have unconditionally supported me throughout all the ups and downs – including when I told them I was pursuing a PhD instead of medical school - and to Tommy, who constantly reminds me that luck is a function of both creativity and perseverance.

Acknowledgements

There have been several individuals who have played roles in impacting both my professional and personal development throughout the course of completing this work. “It takes a village” is a gross understatement. Without the support of these individuals, it is difficult to imagine that I would have grown into the scientist I am today. They have pushed me to think more creatively and critically, to question the boundaries of what is scientifically possible, and to work diligently in producing convincing data to support my hypotheses.

First, I thank my parents, Aleksandar and Gordana, to whom this work is dedicated to. Your continued support has propelled me throughout my scientific career, and you inspire me to pursue my greatest ambitions. Second, I thank Tommy, to whom this work is also dedicated. You have been my rock through all the trials and tribulations that come with pursuing a PhD.

There are many people to specifically thank who have been part of the community that has supported me at UCSF. To Dr. Jim Wells, my PhD mentor – thank you for creating a lab environment that encourages coming up with and testing crazy ideas. Without that, this work surely would not have been possible. I look forward to many more years working together. To Drs. Jason Gestwicki and Aashish Manglik, my thesis committee members – thank you for your support and thoughtful questions and suggestions throughout my PhD. I would also like to thank additional members of my qualifying exam committee, Drs. Adam Renslo and Charly Craik.

Alongside the professors that have supported me, I am grateful to the various members of the Wells lab that have helped me along the path of obtaining my PhD. This list is long and speaks to the unique environment that has been created in our lab – Susanna Elledge, my rotation mentor who I continued to bother over the years; Dr. Jamie Byrnes, who taught me how to refine project proposals and everything I know about T cells; Lisa Kirkemo, my go to for any cancer biology

questions and career discussions; Dr. Shion Lim, my former bay-mate and fellow skiing enthusiast; Dr. Josef Gramespacher and Adam Cotton, who are fellow "Degrader Team" members; Dr. Xin Zhou and Sophie Kong, my bay-mates who were always willing to sit down and brainstorm; Irene Lui and Nick Rettko, additional lab members I would bombard with questions about all things antibodies and cells; and Dr. Jeff Glasgow, who was a walking encyclopedia of knowledge.

Outside of my labmates, there were many peers at UCSF that made this a fun environment to pursue our PhDs in. These include my good friends and cohort buddies Quinn Edmondson, Arthur Tran, Jack Strickland (honorary member), Letitia Sarah, Larry Zhu, and Matt Callahan. It would be impossible to get through this PhD without our laughs, frustrations, long bike rides, and tennis playing.

I'd like to also thank my former mentors from the University of Pennsylvania who helped shape me into the beginnings of an independent scientist before coming to UCSF. These include my incredible former PIs Drs. Megan Matthews, Zhaolan Zhou, and Steven Spiegel. Without you taking the time to teach me how to perform high quality, rigorous research, I cannot imagine where I would be today. I also learned a tremendous amount from various graduate students in these labs. Specifically, I thank Dr. Jacque Faylo, who was my collaborator in the Christiansen lab and taught me X-ray crystallography, and Dr. Sheng Tang, who was my mentor in the Zhou lab.

Finally, I'd like to thank the institutions who believed in my work enough to provide funding for it. Specifically, the NIH Ruth L. Kirschstein National Research Service Award (F311F31CA265080-01) and the UCSF Discovery Fellows program supported my training and the work presented herein.

Contributions

Chapter 1: Adapted version of unpublished work that has been submitted for publication. The contributors and title of this work are: **Pance, K**, Gramespacher, J.A., Salangsang, F., Serrano, J.A.C., Cotton, A.D., Steri, V., Wells, J.A. Cytokine receptor targeting chimeras for degradation of extracellular proteins.

Chapter 2: Unpublished work that has not yet been submitted for publication. Katarina Pance performed the synthesis of adenosine 2a receptor agonist conjugates, bioconjugation, and degradation experiments for both adenosine 2a receptor. James A. Wells oversaw the project.

Chapter 3: Adapted version of the following published manuscript: Lim, S.A.*, Gramespacher, J.A.*, **Pance, K.*,** Rettko, N.J., Solomon, P., Jin, J., Lui, I., Elledge, S.K., Liu, J., Bracken, C.J., Zhou, Simmons, G., X.X., Leung, K.K., and Wells, J.A. Bi-specific VH/Fab antibodies targeting neutralizing and non-neutralizing Spike epitopes demonstrate enhanced potency against SARS-CoV-2. *mAbs*, 2021. *Denotes equal contribution to this work.

Development of novel bispecific antibody modalities for targeted degradation and anti-viral therapeutic applications

Katarina Pance

Abstract

Monoclonal antibodies have created tremendous value for patients, with six of the top ten selling FDA approved drugs being monoclonal antibodies. Generally, monoclonal antibodies work by blocking protein function or inducing cell death via effector functions, such as antibody-dependent cellular toxicity. Though monoclonal antibodies have been greatly successful for various targets and diseases, some disease contexts could benefit from added functionality. For example, on-target, off-tumor toxicity is common when using a monoclonal antibody to target a disease protein that is also expressed on normal cells, as is the case with human epidermal growth factor receptor in breast cancer. Bispecific or bifunctional antibodies, which can recognize two different antigens or have dual functionalities, have the potential to offer greater selectivity, efficacy, and functionality compared to monoclonal antibodies. Various forms of bispecific antibodies exist to date, including bispecific IgGs, which add disease specificity by targeting a disease-specific protein and the target protein simultaneously, bispecific T cell engagers, which enable recruitment of cytotoxic T cells to tumor cells, and antibody-drug conjugates, which involve the tumor specific delivery of a highly cytotoxic small molecule payload using antibody-induced receptor internalization. Here, I describe three novel approaches using bifunctional antibody-based technologies. In Chapter 1, I describe the use of bispecific antibody-cytokine fusions, termed KineTACs, which can be applied as a novel strategy for the targeted degradation of cell surface and extracellular proteins. In Chapter 2, I highlight an orthogonal targeted degradation approach

using antibody-drug conjugates in which the antibody recruits a cell surface E3 ligase, and the small molecule binds a cell surface multi-pass membrane protein, enabling its degradation. In Chapter 3, I describe the use of bispecific VH-Fab IgGs targeting different epitopes on the Spike protein as a novel anti-viral strategy against SARS-CoV-2 virus.

Table of Contents

List of Figures

List of Tables

List of Abbreviations

A2AR – Adenosine 2a receptor

AbTAC – Antibody-based PROTAC

ACE2 – Angiotensin-converting enzyme II

ADC – Antibody-drug conjugate

ADC-TAC – Antibody-drug conjugate PROTAC

ATTEC – Autophagosome-tethering compound

AUTAC – Autophagy targeting chimera

BLI – Biolayer interferometry

cAMP – Cyclic AMP

CDCP1 – CUB-domain containing protein 1

CDR – Complementarity determining region

CPE – Cytopathic effect

D_{max} – Maximal degradation

EGFR – Epidermal growth factor receptor

GPCR – G protein-coupled receptor

HER2 – Human epidermal growth factor receptor 2

IMiD – Immunomodulatory imide drug

K_D – Binding affinity

K_{off} – Dissociation rate

K_{on} – Association rate

KIH – Knob-in-hole

KineTAC – Cytokine receptor targeting chimera

LYTAC – Lysosome targeting chimera

PD-1 – Programmed death protein 1

PD-L1 – Programmed death ligand 1

PROTAC – Proteolysis targeting chimera

RBD – Receptor binding domain

SA – Streptavidin

S_{ecto} – Spike ectodomain

TNFa – Tumor necrosis factor alpha

TROP2 – Tumor-associated calcium signal transducer 2

VEGF – Vascular endothelial growth factor

VH – Variable heavy

Chapter 1

Cytokine receptor targeting chimeras for the degradation of extracellular proteins

Abstract

Targeted protein degradation is a promising therapeutic strategy that overcomes many limitations of traditional inhibitors, such as inhibiting both catalytic and scaffolding functions, and the ability to target "undruggable" proteins.[1] The majority of targeted degradation strategies harness the ubiquitin-proteasome system to facilitate degradation. Though these have shown success for intracellular protein degradation, the extracellular and cell surface proteome remain largely out of reach. Given the vast number of therapeutically relevant disease targets that reside extracellularly[2], there is a critical need for the development of degraders capable of engaging this important class. Though a handful of degraders utilizing the lysosome pathway have been described to address these targets[3–6], these approaches remain limited due to lack of modularity, ease of development, and applicability to both cell surface and extracellular proteins. Here, we describe a novel lysosomal degradation strategy, termed cytokine receptor targeting chimeras (KineTACs). KineTACs are fully genetically encoded bispecific antibodies consisting of a cytokine arm, which targets its cognate cytokine receptor, and a target binding arm. We show that CXCL12 bearing KineTACs can utilize cytokine-mediated receptor internalization of the decoy receptor CXCR7 to deliver target proteins to the lysosome. The target scope of KineTACs is vast – here alone we demonstrate successful degradation of programmed death ligand 1, human epidermal growth factor receptor 2, epidermal growth factor receptor, programmed death protein 1, CUB-domain containing protein 1, tumor-associated calcium signal transducer 2, vascular endothelial growth factor, and tumor necrosis factor alpha. Thus, KineTACs represent a highly modular, selective, and simple strategy for inducing lysosomal delivery of extracellular and cell surface targets. Given their ease of production and target applicability, we anticipate KineTACs to have broad therapeutic and research applications.

Introduction

Targeted protein degradation has emerged over the last two decades as a promising therapeutic strategy with advantages over conventional inhibition.[7] Unlike inhibitors, which operate through occupancy-driven pharmacology, degraders can enable catalytic and durable knockdown of protein levels using event-driven pharmacology. Most degrader technologies, such as proteolysis targeting chimeras (PROTACs)[8] and immunomodulatory imide drugs (IMiDs)[9], co-opt the ubiquitin proteasome system to degrade traditionally challenging proteins. Intracellular small molecule degraders have demonstrated success in targeting over 60 proteins and several are currently being tried in the clinic.[10] However, due to their intracellular mechanism of action, these approaches are limited to targeting proteins with ligandable cytosolic domains. To expand targeted degradation to the cell surface and extracellular proteome, two recent lysosomal degradation platforms have been developed. One, lysosome targeting chimeras (LYTACs), utilizes IgG-glycan bioconjugates to co-opt lysosome shuttling receptors.[4,11] LYTAC production requires complex chemical synthesis and *in vitro* bioconjugation of large glycans which are preferentially cleared in the liver, limiting the applicability of this platform. A second extracellular degradation platform, called antibody-based PROTACs (AbTACs), utilizes bispecific IgGs to hijack cell surface E3 ligases.[3] Due to the dependence on intracellular ubiquitin transfer, AbTACs are limited to targeting cell surface proteins, leaving the secreted proteome undruggable. Thus, there remains a critical need to develop additional degradation technologies for extracellular proteins. Here, we have developed a novel targeted degradation platform, termed cytokine receptor targeting chimeras (KineTACs). KineTACs are fully recombinant bispecific antibodies built of human scaffolds that utilize cytokine-mediated internalization of its cognate receptor to enable highly selective lysosomal delivery of both cell surface and extracellular proteins. To demonstrate the utility of this

platform, chemokine CXCL12 was chosen as it specifically binds the atypical chemokine receptor CXCR7, a decoy receptor that constitutively internalizes and recycles.[12] We show that KineTACs bearing CXCL12 can efficiently utilize CXCR7 internalization for lysosomal degradation applications and are generalizable against various therapeutically relevant proteins (**Fig. 1.1a**).

Results

KineTACs mediate the degradation of various therapeutically relevant cell surface proteins

To demonstrate proof-of-concept that CXCL12 bearing KineTACs can degrade cell surface proteins, we first targeted programmed death ligand 1 (PD-L1). Overexpression of PD-L1 on cancer cells leads to inhibition of checkpoint protein programmed death protein 1 (PD-1) and suppression of cytotoxic T cell activity.[13] First, we generated knob-in-hole bispecifics[14] in which the human CXCL12 chemokine was N-terminally fused to the knob Fc domain and the antibody sequence for atezolizumab (Tecentriq), an FDA approved inhibitor of PD-L1, was fused to the hole Fc (**Fig. 1.1a**). CXCL12 bearing bispecifics are not limited by the light chain mispairing problem, which is common to bispecific IgGs with Fabs on both arms, enabling full assembly of KineTACs during mammalian expression.[15,16] A His tag was introduced on the knob arm to allow purification of the formed bispecific from unwanted hole-hole homodimers that may form. Next, we confirmed that the PD-L1 targeting KineTAC (herein termed CXCL12-Atz) retains binding to PD-L1 using biolayer interferometry (BLI) (**Fig. 1.1b**). Furthermore, an isotype control of the CXCL12 KineTAC, which incorporates a Fab arm to the SARS-CoV-2 spike protein[17], retained binding to endogenous CXCR7 expressed on triple negative breast cancer cell line MDA-MB-231 (**Fig. 1.1c**). This data suggested that both anti-PD-L1 and CXCL12 arms of the KineTAC were functional in the bispecific context. To determine whether CXCL12-Atz could degrade PD-L1, MDA-MB-231 cells were treated with varying concentrations of the KineTAC. After 24 hr

treatment, levels of PD-L1 were quantified using western blotting, demonstrating that both glycosylated forms of PD-L1 were substantially degraded, with a maximal percent degradation (D_{max}) of roughly 70% (**Fig. 1.1d-e**). Control antibodies, such as atezolizumab Fab or CXCL12 isotype, do not induce the degradation of PD-L1 either alone or in combination, indicating that PD-L1 degradation is dependent on the bispecific KineTAC scaffold (**Fig. 1.1f, Fig. 1.2a-b**). Finally, flow cytometry and western blotting was used to verify that the PD-L1 degradation observed is due to depletion of cell surface PD-L1(**Fig. 1.2c-d**).

We next sought to determine whether the KineTAC platform could be generalized to degrade other therapeutically relevant cell surface proteins. First, we targeted human epidermal growth factor receptor 2 (HER2), which is frequently upregulated in cancer and linked to breast cancer invasiveness and tumor progression.[18] To develop a KineTAC targeting HER2, we incorporated the antibody sequence for trastuzumab (Herceptin), an FDA approved HER2 inhibitor, into the KineTAC scaffold (herein termed CXCL12-Tras). Various breast cancer cell lines endogenously expressing HER2 were incubated for 24 hr with CXCL12-Tras. Substantial degradation of HER2 was observed in MCF7 and MDA-MB-175VII cells, with D_{max} of 51 and 62%, respectively (**Fig. 1.1g-h, Fig. 1.3a**). Unsurprisingly, lower percent degradation was observed in SK-BR-3 cells, which overexpresses HER2 relative to CXCR7[19] (**Fig. 1.1h, Fig. 1.3b**), suggesting that the maximal percent degradation mediated by KineTACs could be dependent on the expression of the target protein relative to CXCR7. Next, we targeted epidermal growth factor receptor (EGFR) for degradation. EGFR is implicated as a driver of cancer progression, and EGFR inhibitors are approved for use in non-small cell lung, colorectal, and gastric cancers.[20–22] We developed KineTACs targeting EGFR by incorporating cetuximab (Erbitux), an FDA approved EGFR inhibitor, into the KineTAC scaffold (herein termed CXCL12-Ctx). Following 24 hr

treatment with CXCL12-Ctx, EGFR levels were dramatically reduced in HeLa cells, with a D_{max} of 84% observed (**Fig. 1.1i-j**). This result was recapitulated in various breast and lung cancer cell lines, including MDA-MB-231, A431, and NCI-H292 (**Fig. 1.1j, Fig. 1.3c-e**).

We found that the KineTAC scope can be expanded beyond receptor tyrosine kinases. Using a previously described antibody against CUB domain-containing protein 1 (CDCP1)[23], we observed near complete degradation of CDCP1 after 24 hr treatment of HeLa cells, with a D_{max} of 93% (**Fig. 1.3f**). KineTACs also enabled the degradation of tumor-associated calcium signal transducer 2 (TROP2), the overexpression of which has been linked to tumor progression in a variety of tumors.[24,25] In MCF7 cells, we observed a D_{max} of 51% after treatment with TROP2 targeting KineTAC (**Fig. 1.3g**). We then tested whether KineTACs are active to degrade the checkpoint protein PD-1 in CD8+ T cells isolated from primary human peripheral blood mononuclear cells. T cells were then activated, causing overexpression of PD-1 on the cell surface along with other activation markers (**Fig. 1.4a-b**). Activated T cells were then treated for 24 hr with a PD-1 targeting KineTAC, which incorporates the antibody sequence for nivolumab (Opdivo), an FDA approved PD-1 inhibitor (herein termed CXCL12-Nivo). Following treatment with CXCL12-Nivo, cell surface PD-1 levels were dramatically reduced, with a D_{max} of 82%, compared to nivolumab isotype control, which is known to induce slight internalization of PD-1 (**Fig. 1.1k, Fig. 1.4c**).[26] Overall, these results demonstrate the generality of the KineTAC platform for degrading a variety of cell surface proteins for degradation (**Table 1.1**).

Requirements for efficient KineTAC-mediated degradation

Next, we sought to determine which properties, such as binding and receptor signaling, of the KineTAC are critical for efficient degradation. Alongside CXCR7, CXCL12 binds the signaling

receptor CXCR4, which upon agonism will cause downstream signaling followed by receptor internalization and degradation. Signaling through CXCR4 could be counter-productive if using KineTACs to target cancer drivers, as CXCR4 overexpression and agonism is linked to tumor metastasis.[27] Thus, avoiding CXCR4 signaling could be an important consideration in developing KineTACs for therapeutic purposes. To test this, KineTACs bearing previously described antagonistic variants of CXCL12 (ΔKP, ΔKPVS, and R8E), that retain binding to both CXCR7 and CXCR4 but prevent CXCR4 signaling, were incorporated into the KineTAC scaffold with atezolizumab.[12,28] Following 24 hr treatment in MDA-MB-231 cells, all three antagonistic variants retained the ability to degrade PD-L1 to a similar degree compared to $CXCL12^{WT}$ (**Fig. 1.5a-b**). This data suggests that CXCL12 signaling through CXCR4 is not critical for degradation, allowing flexibility to include or eliminate it depending on the biology we wish to affect. Next, the dependence on binding affinity to target receptor was probed by introducing alanine mutations into key interacting residues of atezolizumab's complementary determining regions known to interact with PD-L1 based on the known structure of the complex. We generated a library of alanine-scanned mutants of atezolizumab with a range of binding affinities (K_D, 0.33-458 nM) and corresponding kinetic parameters (k_{on} and k_{off}) to PD-L1, as measured with BLI (**Table 1.2**). The atezolizumab mutants were then introduced into the KineTAC scaffold with $CXCL12^{WT}$ and tested for their ability to degrade PD-L1 (**Fig. 1.5c, Fig. 1.6a**). Correlating the PD-L1 levels post-treatment to the different kinetic parameters of these binders, we find that degradation is correlated to the K_D (R^2=0.638) and the dissociation rate (k_{off}, R^2=0.804), but not to the association rate (k_{on}, R^2=0.036) (**Fig. 1.5d-f**). Of the mutants tested, wild-type atezolizumab had the highest binding affinity and induced the greatest level of PD-L1 degradation. Therefore, over this affinity range,

the levels of degradation are dependent on the binding affinity of the antibody arm to the target protein.

To determine whether a pH-dependent antibody binder against the target protein would affect degradation, BMS936559, an anti-PD-L1 antibody reported to release PD-L1 in acidic (pH<6.0) conditions[29], was introduced into the KineTAC scaffold. Treatment with CXCL12-BMS936559 compared to CXCL12-Atz showed that pH-dependent release of PD-L1 slightly decreases the maximal level of degradation observed (**Fig. 1.5g**). This result is not due to differences in K_D as atezolizumab and BMS936559 are reported to have similar binding affinities to PD-L1.[30] To investigate whether the binding epitope on the protein of interest could impact degradation, we introduced additional HER2 and EGFR targeting antibodies into the KineTAC scaffold that have been described to bind different epitopes. For HER2, pertuzumab (Perjeta), which is known to bind a distinct epitope from trastuzumab on HER2[31], was introduced into the KineTAC scaffold (herein termed CXCL12-Ptz). Following 24 hr treatment of MCF7 cells, we find that CXCL12-Tras is superior to CXCL12-Ptz at lower concentrations, indicating that epitope can alter the dose response to KineTACs (**Fig. 1.5h**). For EGFR, we introduced five different anti-EGFR binders (depatuxizumab, nimotuzumab, panitumumab (Vectibix), necitumumab (Portrazza), and matuzumab)[32] into the KineTAC scaffold. Following 24 hr treatment of HeLa cells, we observe that some epitope binders, such as necitumumab and matuzumab, retain similar levels of EGFR degradation compared to CXCL12-Ctx, while other epitope binders, such as depatuxizumab, nimotuzumab, and panitumumab, abrogate or impair the ability to degrade EGFR (**Fig. 1.5i**). Further, the degradation observed for each binder is not correlated to binding affinity (R^2 = 0.008, **Fig. 1.6b**). This data highlights the dependence of KineTAC-mediated degradation on target binding epitope.

Next, we asked whether glycosylation of the KineTAC Fc domain at the N297 position would impact degradation. The N297G mutation is commonly introduced into IgGs to produce an aglycosylated form to eliminate effector function. However, glycosylation at N297 can impart greater stability and favorable pharmacokinetic properties.[33] The glycosylation site at N297 was re-introduced to the CXCL12-Atz scaffold and the degradation efficiency between the glycosylated and aglycosylated forms compared. We find that glycosylation at N297 does not significantly impact PD-L1 degradation levels (**Fig. 1.6c**). Thus, the improved stability and pharmacokinetic properties of KineTACs can be utilized for *in vivo* use without major disruption to degradation efficiency. Finally, we determined whether the bispecific antibody construct used could influence levels of degradation. To this end, a Fab fusion construct in which CXCL12 is fused to the N-terminus of the atezolizumab Fab heavy chain via a flexible Avidin tag linker was co-expressed with atezolizumab Fab light chain (**Fig. 1.6d**). The CXCL12-Atz Fab fusion retained binding to PD-L1 Fc fusion as measured by BLI (**Fig. 1.6e**). After 24 hr treatment in MDA-MB-231, the levels of PD-L1 were measured by western blotting. While the bispecific IgG construct caused significant degradation of PD-L1, the Fab fusion was unable to induce significant degradation, with a D_{max} of only 20% observed (**Fig. 1.6f**). The differences in degradation between these two constructs could be due to several factors, including construct rigidity and linker length. Overall, this data highlights that the bispecific IgG is a useful KineTAC scaffold.

Mechanism and selectivity of KineTAC-mediated degradation

We next sought to evaluate the mechanism of KineTAC-mediated degradation. To determine whether KineTACs catalyze degradation via the lysosome or proteasome, MDA-MB-231 cells were pre-treated with either media alone, bafilomycin (an inhibitor of lysosome acidification), or

MG132 (a proteasome inhibitor). After 1 hr pre-treatment, cells were treated with CXCL12-Atz for 24 hrs. We observed that bafilomycin pre-treatment inhibited degradation of PD-L1, while MG132 had no effect, demonstrating that KineTACs mediate degradation via delivery of target proteins to the lysosome (**Fig. 1.7a**). Immunofluorescent microscopy revealed complete removal of EGFR from the cell surface following 24 hr CXCL12-Ctx treatment as compared to the cetuximab isotype, further highlighting that KineTACs induce robust internalization of target proteins (**Fig. 1.7b**). Furthermore, KineTAC-mediated degradation occurs in a time-dependent fashion, beginning after 6 hrs post-treatment with CXCL12-Atz, with the levels of PD-L1 continuing to decrease over time to near complete degradation at 48 hrs (**Fig. 1.7c-d**). We next wished to determine which of the two receptors is more important for degrading surface proteins in the context of KineTACs. To confirm that KineTAC mechanism of action occurs via CXCR7 and not CXCR4, RNA interference was used to knockdown the levels of CXCR4 in HeLa cells. After 48 hr transfection with CXCR4-targeting or control siRNA pools, cells were treated with CXCL12-Ctx for 24 hrs (**Fig. 1.7e**). Western blotting analysis revealed that EGFR degradation levels are unchanged with CXCR4 knocked down. This data highlights that CXCR4 is not necessary for efficient degradation and suggests that KineTACs operate through CXCR7-mediated internalization (**Fig. 1.7f**). Furthermore, KineTACs bearing CXCL11, a chemokine that specifically binds CXCR7 and CXCR3 but not CXCR4[34], are capable of degrading both PD-L1 and EGFR (**Fig. 1.7g, Fig. 1.8a-d**). This result further highlights that CXCR7 is the receptor responsible for KineTAC-mediated degradation and demonstrates the exciting opportunity for using alternative cytokines in the KineTAC scaffold to degrade target proteins.

We next used quantitative mass spectrometry to determine whether proteome-wide changes occur following KineTAC treatment. Both the surface-enriched and whole cell lysates

were analyzed following 48 hr CXCL12-Atz or CXCL12-Ctx treatment compared to PBS treated control in MDA-MB-231 or HeLa cells, respectively. For PD-L1 degradation, the surface-enriched sample revealed no significant changes to the proteome, with PD-L1 being the only protein downregulated in CXCL12-Atz treatment compared to control (**Fig. 1.7h**). Whole cell proteomics also revealed that no major changes are occurring (**Fig. 1.7i**). PD-L1 was not detected in the whole cell sample, likely due to low abundance of cell surface proteins relative to cytosolic proteins. Similar results were observed for EGFR degradation, with no major proteome-wide changes occurring and EGFR being virtually the only proteins significantly downregulated in CXCL12-Ctx treatment compared to control in both the surface-enriched and whole cell proteomics (**Fig. 1.7j-k**). Interestingly, a previously published proteomics dataset of LYTAC-mediated EGFR degradation identified additional proteins significantly up- or down-regulated following LYTAC treatment.[4] Comparing to our experiment in the same cell line suggests that KineTACs are more selective in degrading EGFR. As there is large overlap in peptide IDs observed between the two datasets, the observed greater selectivity is not due to lack of sensitivity of the KineTAC proteomics experiment (**Fig. 1.9a-b**). CXCR4 and CXCR7 peptide IDs were not altered in the surface-enriched sample, and CXCR4 IDs were also unchanged in the whole cell sample, indicating that treatment with KineTAC does not significantly impact CXCR4 or CXCR7 levels. Furthermore, protein levels of GRB2 and SHC1, which are known interacting partners of EGFR[4], were also not significantly changed. Together, these data demonstrate the exquisite selectivity of KineTACs for degrading only the target protein and not inducing unwanted, off-target proteome-wide changes.

To elucidate whether KineTAC-mediated degradation could impart functional cellular consequences, cell viability of HER2 expressing cells was measured following treatment with

CXCL12-Tras. MDA-MB-175VII breast cancer cells are reported to be sensitive to trastuzumab treatment, and as such serve as an ideal model to test the functional consequence of degrading HER2 compared to inhibition with trastuzumab IgG.[37] To this end, cells were treated with either CXCL12-Tras or trastuzumab IgG for 5 days, after which the cell viability was determined using a modified MTT assay. Reduction in cell viability was observed at higher concentrations of CXCL12-Tras and was significantly greater than trastuzumab IgG alone (**Fig. 1.7l**). These data demonstrate that KineTAC-mediated degradation has functional consequences in reducing cancer cell viability *in vitro* and highlights that KineTACs could provide advantages over traditional antibody therapeutics which bind but do not degrade.

Finally, we asked whether KineTACs would have similar antibody clearance to IgGs *in vivo.* To this end, male nude mice were injected intravenously with 5, 10, or 15 mg/kg CXCL12-Tras, which is a typical dose range for antibody xenograft studies. Western blotting analysis of plasma antibody levels revealed that the KineTAC remained in plasma up to 10 days post-injection with a half-life of 8.7 days, which is comparable to the reported half-life of IgGs in mice (**Fig. 1.7m, Fig. 1.10a**).[38] Given the high homology between human and mouse CXCL12, we tested whether human CXCL12 isotype could be cross-reactive. Human CXCL12 isotype binding to mouse cell lines MC38 and CT26, which endogenously express mouse CXCR7, was confirmed (**Fig. 1.10b-c**). Together, these results demonstrate that KineTACs have favorable stability and are not being rapidly cleared despite cross-reactivity with mouse CXCR7 receptors. Since atezolizumab is also known to be cross-reactive, CXCL12-Atz ability to degrade mouse PD-L1 was tested in both MC38 and CT26. Indeed, CXCL12-Atz mediates near complete degradation of mouse PD-L1 in both cell lines (**Fig. 1.10d-f**). Thus, PD-L1 degradation may serve as an ideal mouse model to assay the efficacy of KineTACs *in vivo*.

KineTACs are generalizable to targeting extracellular soluble ligands

Having demonstrated the ability of KineTACs to mediate cell surface protein degradation, we next asked whether KineTACs could also be applied towards the degradation of soluble extracellular proteins. Soluble ligands, such as inflammatory cytokines and growth factors, have been recognized as an increasingly important therapeutic class. Of these, vascular endothelial growth factor (VEGF) and tumor necrosis factor alpha (TNFa) represent the most targeted soluble ligands by antibody and small molecule drug candidates, highlighting their importance in disease.[39] Thus, we chose VEGF and TNFa as ideal proof-of-concept targets to determine whether KineTACs could be expanded to degrading extracellular soluble ligands (**Fig. 1.11a**). First, we targeted VEGF by incorporating bevacizumab (Avastin), an FDA approved VEGF inhibitor, into the KineTAC scaffold (herein termed CXCL12-Beva). Next, HeLa cells were incubated with VEGF-647 or VEGF-647 and CXCL12-Beva for 24 hr. Following treatment, flow cytometry analysis showed a robust increase in cellular fluorescence when VEGF-647 was co-incubated with CXCL12-Beva, but not bevacizumab isotype which lacks the CXCL12 arm (**Fig. 1.11b-c**). To ensure that the increased cellular fluorescence was due to intracellular uptake of VEGF-647 and not surface binding, we determined the effect of an acid wash which removes any cell surface binding after 24 hr incubation (**Fig. 1.11d**). We found that there was no significant difference in cellular fluorescence levels between acid and normal washed cells. This data suggests that KineTACs successfully mediate the intracellular uptake of extracellular VEGF. Similar to membrane protein degradation, KineTAC-mediated uptake of VEGF occurs in a time-dependent manner, with robust internalization occurring before 6 hrs and reaching steady state by 24 hrs (**Fig. 1.11e**). Furthermore, the levels of VEGF uptake are dependent on the KineTAC:ligand ratio and saturate at ratios greater than 1:1 (**Fig. 1.11f**). We next tested the ability of CXCL12-Beva to promote

uptake on other cell lines and find that these cells also significantly uptake VEGF (**Fig. 1.11g**). Moreover, the extent of uptake is correlated with the transcript levels of CXCR7 in these cells (R^2 = 0.555, **Fig. 1.12**). These data suggest that KineTACs directed against soluble ligands can promote broad tissue clearance of these targets as compared to glycan- or Fc-mediated clearance mechanisms.

To demonstrate the generalizable nature of the KineTAC platform for targeting soluble ligands, we next targeted TNFa by incorporating adalimumab (Humira), an FDA approved TNFa inhibitor, into the KineTAC scaffold (herein termed CXCL12-Ada). Following 24 hr treatment of HeLa cells, significant increase in cellular fluorescence was observed when TNFa-647 was co-incubated with CXCL12-Ada compared to adalimumab isotype (**Fig. 1.13a-b**). Consistent with the VEGF uptake experiments, acid wash did not alter the level of cellular fluorescence increase observed, and uptake was dependent on the KineTAC:ligand ratio (**Fig. 1.13c-d**). Thus, KineTACs are generalizable in mediating the intracellular uptake of soluble ligands, significantly expanding the target scope of KineTAC-mediated targeted degradation.

Discussion

In summary, our data suggest that KineTACs are a versatile and modular targeted degradation platform that enable robust lysosomal degradation of both cell surface and extracellular proteins. We find that KineTAC-mediated degradation is driven by recruitment of both CXCR7 and target protein, and that factors such as binding affinity, epitope, and construct design can affect efficiency. Other factors, such as signaling competence and pH dependency for the protein of interest, did not impact degradation for CXCL12 bearing KineTACs. These results provide valuable insights into how to engineer effective KineTACs going forward. Furthermore, we show

that KineTACs operate via time-, lysosome-, and CXCR7-dependence and are exquisitely selective in degrading target proteins with minimal off-target effects. Initial experiments with an alternative cytokine, CXCL11, highlight the versatility of the KineTAC platform and the exciting possibility of using various cytokines and cytokine receptors for targeted lysosomal degradation. KineTACs are built from simple genetically encoded parts that are readily accessible from the genome and published human antibody sequences. Given differences in selectivity and target scope that we and others have observed between degradation pathways, there is an ongoing need to co-opt novel receptors for lysosomal degradation, such as CXCR7, that may offer advantages in terms of tissue selectivity or degradation efficiency. Thus, we anticipate ongoing work on the KineTAC platform to offer new insights into which receptors can be hijacked and to greatly expand targeted protein degradation to the extracellular proteome for both therapeutic and research applications.

Methods

Cell lines

Cell lines were grown and maintained in T75 (Thermo Fisher Scientific) flasks at 37ºC and 5% CO_2. MDA-MB-231, MDA-MB-175VII, HeLa, and A-431 cells were grown in DMEM supplemented with 10% fetal bovine serum (FBS) and 1% penicillin/streptomycin. MCF7 and NCI-H292 cells were grown in RPMI-1640 supplemented with 10% FBS and 1% penicillin/streptomycin. SK-BR-3 cells were grown in McCoy's 5A supplemented with 10% FBS and 1% penicillin/streptomycin.

Protein expression

Fabs were expressed in *E. coli* C43(DE3) Pro+ grown in an optimized TB autoinduction media at 37ºC for 6 hrs, then cooled to 30ºC for 18 hrs, and purified by Protein A affinity chromatography. IgGs and bispecifics were expressed and purified from Expi293 BirA cells using transient transfection (Expifectamine, Thermo Fisher Scientific). Enhancers were added 20 hrs after transfection. Cells were incubated for 5 days at 37ºC and 8% CO_2. Media was then harvested by centrifugation at 4,000xg for 20 min. IgGs were purified by Protein A affinity chromatography and buffer exchanged into PBS by spin concentration and flash frozen for storage at -80ºC. Bispecifics were purified by Ni-NTA affinity chromatography and buffer exchanged into PBS containing 20% glycerol, concentrated, and flash frozen for storage at -80ºC. Purity and integrity of all proteins were assessed by SDS-PAGE.

Biolayer interferometry

Biolayer interferometry (BLI) data were measured using an Octet RED384 (ForteBio) instrument. Biotinylated antigens were immobilized on a streptavidin biosensor and loaded until 0.4 nm signal was achieved. After blocking with 10 μM biotin, purified antibodies in solution was used as the analyte. PBSTB was used for all buffers. Data were analyzed using the ForteBio Octet analysis software and kinetic parameters were determined using a 1:1 monovalent binding model.

Degradation experiments

Cells were plated in 6- or 12-well plates and grown to ~70% confluency before treatment. Media was aspirated and cells were treated with bispecifics or control antibodies in complete growth medium. For soluble ligand uptake experiments, biotinylated soluble ligand was pre-incubated

with streptavidin-647 at 37ºC for 30 min, then mixed with bispecific or control antibodies and added to cells. After incubation at 37ºC for the designated time point, cells were washed with phosphate-buffered saline (PBS), lifted with versene, and harvested by centrifugation at 300xg for 5 min at 4ºC. Samples were then tested by western blotting or flow cytometry to quantify protein levels.

Western blotting

Cell pellets were lysed with 1x RIPA buffer containing cOmplete mini protease inhibitor cocktail (Sigma-Aldrich) at 4ºC for 40 min. Lysates were centrifuged at 16,000xg for 10 min at 4ºC and protein concentrations were normalized using BCA assay (Pierce). 4x NuPAGE LDS sample buffer (Invitrogen) and 2-mercaptoethanol (BME) was added to the lysates and boiled for 10 min. Equal amounts of lysates were loaded onto a 4-12% Bis-Tris gel and ran at 200V for 37 min. The gel was incubated in 20% ethanol for 10 min and transferred onto a polyvinylidene difluoride (PVDF) membrane. The membrane was blocked in PBS with 0.1% Tween-20 + 5% bovine serum albumin (BSA) for 30 min at room temperature with gentle shaking. Membranes were incubated overnight with primary antibodies at respective dilutions at 4ºC with gentle shaking in PBS + 0.2% Tween-20 + 5% BSA. Membranes were washed four times with tris-buffered saline (TBS) + 0.1% Tween-20 and then co-incubated with HRP-anti-rabbit IgG (Cell Signaling Technologies, 7074A, 1:2000) and 680RD goat anti-mouse IgG (LI-COR, 926-68070, 1:10000) in PBS + 0.2% Tween-20 + 5% BSA for 1 hr at room temperature. Membranes were washed four times with TBS + 0.1% Tween-20, then washed with PBS. Membranes were imaged using an OdysseyCLxImager (LI-COR). SuperSignal West Pico PLUS Chemiluminescent Substrate (Thermo Fisher Scientific) was

then added and imaged using a ChemiDoc Imager (BioRad). Band intensities were quantified using Image Studio Software (LI-COR).

Primary human CD8+ T cell isolation

Primary human T cells were isolated from leukoreductin chamber residuals following Trima Apheresis (Blood Centers of the Pacific) using established protocols.[40] Briefly, peripheral blood mononuclear cells (PBMCs) were isolated using Ficoll separation in SepMate tubers (STEMCELL Technologies) according to manufacturer's instructions. CD8+ T cells were isolated from PBMCs using the EasySep™ Human CD8+ T cell Isolation Kit following the manufacturer's protocol. Isolated cell populations were then analyzed for purity by flow cytometry on a Beckman Coulter CytoFlex flow cytometer using a panel of antibodies (anti-CD3, anti-CD4, anti-CD8a, all from BioLegend).

CD8+ T cell activation

Following CD8+ T cell isolation, cells were stimulated with recombinant IL-2 (GoldBio), IL-15 (GoldBio), and ImmunoCult Human CD3/CD28 T cell Activation (STEMCELL Technologies) for 4 days at 37ºC. Activated CD8+ T cells were then analyzed for the upregulation of activation markers CD25 and PD-1 by flow cytometry using anti-CD25 and anti-PD-1 antibodies (BioLegend). Once activation was confirmed, cells were dosed as described above and levels of target protein analyzed by flow cytometry.

Flow cytometry

Cell pellets were washed with cold PBS and centrifuged at 300xg for 5 min. Cells were blocked with cold PBS + 3% BSA and centrifuged (300xg for 5 min). Cells were incubated with primary antibodies diluted in PBS + 3% BSA for 30 min at 4ºC. Cells were washed three times with cold PBS + 3% BSA and secondary antibodies (if applicable) diluted in PBS + 3% BSA added and incubated for 30 min at 4ºC. Cells were washed three times with cold PBS + 3% BSA and resuspended in cold PBS. Flow cytometry was performed on a CytoFLEX cytometer (Beckman Coulter) and gating was performed on single cells and live cells before acquisition of 10,000 cells. Analysis was performed using the FlowJo software package.

Flow cytometry for soluble ligand uptake

Cell pellets were washed three times with cold PBS and centrifuged at 300xg for 5 min. Cells were then resuspended in cold PBS. Flow cytometry was performed on a CytoFLEX cytometer (Beckman Coulter) and gating was performed on single cells and live cells before acquisition of 10,000 cells. Analysis was performed using the FlowJo software package.

Acid wash for soluble ligand uptake

Following 24 hr dosing of cells with soluble ligand and bispecific antibodies, cells were washed with either cold PBS (normal wash) or acid wash buffer (0.2M glycine, 0.15M NaCl, pH 3.0) three times. Cells were then lifted with versene and harvested by centrifugation at 300xg for 5 min. Cells were washed three times with cold PBS and centrifuged at 300xg for 5 min. Cells were then resuspended in cold PBS. Flow cytometry was performed on a CytoFLEX cytometer (Beckman

Coulter) and gating was performed on single cells and live cells before acquisition of 10,000 cells. Analysis was performed using the FlowJo software package.

Confocal microscopy

Cells were plated onto Mat-Tek 35 mm glass bottom petri dishes pre-treated with poly-D-lysine and grown to ~70% confluency before treatment. Media was aspirated and cells were treated with bispecifics or control antibodies in complete growth medium. For soluble ligand uptake experiments, biotinylated soluble ligand was pre-incubated with streptavidin-647 at 37ºC for 30 min, then mixed with bispecific or control antibodies and added to cells. After 24 hr incubation at 37ºC, media was aspirated, and cells were washed with PBS. Cells were then stained using standard protocols for LysoTracker Deep Red (Invitrogen), DAPI (Cell Signaling Technologies), and primary antibody. Samples were imaged using a Nikon Ti Microscope with Yokogawa CSU-22 spinning disk confocal and a 40x objective lens. 405, 488, and 647 nm lasers were used to image DAPI, primary antibody, and LysoTracker, respectively. Images were deconvoluted and processed using NIS-Element and FIJI software packages.

siRNA knockdown

HeLa cells were plated in a 6-well plate and grown to confluency. Cells were transfected with 20 pmol of siRNA (ON-TARGETplus siRNA SMARTPool, Dharmacon) and DharmaFECT 4 reagent (Dharmacon) according to manufacturer's instruction. Cells were incubated for 48-72 hrs at 37ºC under 5% CO_2 and siRNA knockdown was validated by western blotting.

Cell culture/SILAC labeling and treatment

MDA-MB-231 cells were grown in DMEM for SILAC (Thermo Fisher) with 10% dialyzed FBS (Gemini). Media was also supplemented with either light L-[12C6,14N2] lysine/L-[12C6,14N4] arginine (Sigma) or heavy L-[13C6,15N2] lysine/L-[13C6,15N4] arginine (Cambridge Isotope Laboratories, Tewksbury, MA). Cells were maintained in SILAC media for five passages to ensure complete isotopic labeling. Cells were then treated with either PBS control or 100 nM bispecific for 48 hours before cells were collected and heavy/light-labeled cells mixed at a 1:1 ratio in both forward and reverse mode. A small portion of these cells were set aside for whole cell proteomic analysis, and the remainder were used to prepare surface proteome enrichment.

Mass spectrometry sample preparation

Cell surface glycoproteins were captured largely as previously described[41], but using a modified protocol to facilitate small sample input. Briefly, cells were first washed in PBS, pH 6.5 before the glycoproteins were oxidized with 1.6 mM $NaIO_4$ (Sigma) in PBS, pH 6.5 for 20 minutes at 4°C. Cells were then biotinylated via the oxidized vicinal diols with 1 mM biocytin hydrazide (Biotium) in the presence of 10 mM aniline (Sigma) in PBS, pH 6.5 for 90 minutes at 4°C. Cell pellets were lysed with a 2X dilution of commercial RIPA buffer (Millipore) supplemented with 1X Protease Inhibitor Cocktail (Sigma) and 2 mM EDTA (Sigma) for 10 minutes at 4°C. Cells were further disrupted with probe sonication and the cell lysates were then incubated with NeutrAvidin coated agarose beads (Thermo) in Poly-Prep chromatography columns (Bio-Rad) for two hours at 4°C to isolate biotinylated glycoproteins. After this incubation, cells were washed sequentially with 1X RIPA (Millipore) plus 1 mM EDTA, high salt PBS (PBS pH 7.4, 2 M NaCl [Sigma]), and denaturing urea buffer (50 mM ammonium bicarbonate, 2 M Urea). All wash buffers were heated

to 42°C prior to use. Proteins on the beads were next digested and desalted using the Preomics iST mass spectrometry sample preparation kit (Preomics) per the manufacturer's recommendations with few modifications. First, samples were resuspended in the "LYSE" solution and transferred to fresh tubes. After incubating in "LYSE" for 10 minutes at 55°C, the "DIGEST" solution was added and beads incubated for 90 minutes at 37°C with mixing at 500 rpm. Following on-bead digest, the peptide eluate was isolated using SnapCap spin columns (Pierce) and the "STOP" solution added. The sample was then transferred to the Preomics cartridge and desalted using the manufacturer's protocol. Samples were dried, resuspended in 0.1% formic acid, 2% acetonitrile (Fisher), and quantified using the Pierce Peptide Quantification Kit prior to LC-MS/MS analysis. Whole cell lysate samples were prepared using the Preomics kit protocol for whole lysate samples. Resulting peptides were dried and quantified in the same manner as the surface enriched samples.

Mass spectrometry

LC-MS/MS was performed using a Bruker NanoElute chromatography system coupled to a Bruker timsTOF Pro mass spectrometer. Peptides were separated using a pre-packed IonOpticks Aurora (25 cm x 75 μm) C18 reversed phase column (1.6 μm pore size, Thermo) fitted with a CaptiveSpray emitter for the timsTOF Pro CaptiveSpray source. For all samples, 200 ng of resuspended peptides were injected and separated using a linear gradient of 2-23% solvent B (solvent A: 0.1% formic acid + 2% acetonitrile, solvent B: acetonitrile with 0.1% formic acid) over 90 minutes at 400 μL/minute with a final ramp to 34% B over 10 minutes. Separations were performed at a column temperature of 50°C. Data-dependent acquisition was performed using a timsTOF PASEF MS/MS method (TIMS mobility scan range 0.70-1.50 $V \cdot s/cm^2$; mass scan range 100-1700 m/z; ramp time 100 milliseconds; 10 PASEF scans per 1.17 seconds; active exclusion

24 seconds; charge range 0-5; minimum MS1 intensity 500). The normalized collision energy was set at 20.

Data analysis/Statistics

SILAC proteomics data were analyzed using PEAKSOnline (v1.4). For all samples, searches were performed with a precursor mass error tolerance of 20 ppm and a fragment mass error tolerance of 0.03 Da. The digest was considered semi-specific and up to 3 missed cleavages were allowed. For whole cell proteome data, the reviewed SwissProt database for the human proteome (downloaded December 12, 2020) was used. For surface enriched samples, a database composed of SwissProt proteins annotated "membrane" but not "nuclear" or "mitochondrial" was used to ensure accurate unique peptide identification for surface proteins, as previously described.[41] Carbamidomethylation of cystine was used as a fixed modification, whereas the isotopic labels for arginine and lysine, acetylation of the N-terminus, oxidation of methionine, and deamidation of asparagine and glutamine were set as variable modifications. Only PSMs and protein groups with an FDR of less than 1% were considered for downstream analysis. SILAC analysis was performed using the forward and reverse samples, and at least 2 labels for the ID and features were required. Proteins showing a >2-fold change from PBS control with a significance of $P<0.01$ were considered to be significantly changed.

Cell viability experiments

Cell viability assays were performed using an MTT modified assay. In brief, on day 0 15,000 MDA-MB-175VII cells were plated in each well of a 96-well plate. On day 1, bispecifics or control antibodies were added in a dilution series. Cells were incubated at 37ºC under 5% CO_2 for 5 days.

On day 6, 40 µL of 2.5 mg/mL thiazolyl blue tetrazolium bromide (GoldBio) was added to each well and incubated at 37ºC under 5% CO_2 for 4 hrs. 100 µL of 10% SDS in 0.01M HCl was then added to lyse cells and release MTT product. After 4 hrs at room temperature, absorbance at 600 nm was quantified using an Infinite M200 PRO plate reader (Tecan). Data was plotted using GraphPad Prism software (version 9.0) and curves were generated using non-linear regression with sigmoidal 4PL parameters.

Antibody in vivo stability study

Male nude nu/nu mice (8-10 weeks old, bred at the UCSF MZ Breeding Facility) were treated with 5, 10, or 15 mg/kg CXCL12-Tras via intravenous injection (3 mice per group). Blood was collected from the lateral saphenous vein using EDTA capillary tubes at day 0 prior to intravenous injection and at days 3, 5, 7, and 10 post injection. Plasma was separated after centrifugation at 700xg at 4ºC for 15 min. To determine the levels of CXCL12-Tras, 1 µL of plasma was diluted into 30 µL of NuPAGE LDS sample buffer (Invitrogen) and loaded onto a 4-12% Bis-Tris gel and ran at 200V for 37 min. The gel was incubated in 20% ethanol for 10 min and transferred onto a polyvinylidene difluoride (PVDF) membrane. The membrane was washed with water followed by incubation for 5 min with REVERT 700 Total Protein Stain (LI-COR). The blot was then washed twice with REVERT 700 Wash Solution (LI-COR) and imaged using an OdysseyCLxImager (LI-COR). The membrane was then blocked in PBS with 0.1% Tween-20 + 5% bovine serum albumin (BSA) for 30 min at room temperature with gentle shaking. Membranes were incubated overnight with 800 CW goat anti-human IgG (LI-COR, 1:10000) at 4ºC with gentle shaking in PBS + 0.2% Tween-20 + 5% BSA. Membranes were washed four times with tris-buffered saline (TBS) + 0.1% Tween-

20 and then washed with PBS. Membranes were imaged using an OdysseyCLxImager (LI-COR). Band intensities were quantified using Image Studio Software (LI-COR).

Figures and Tables

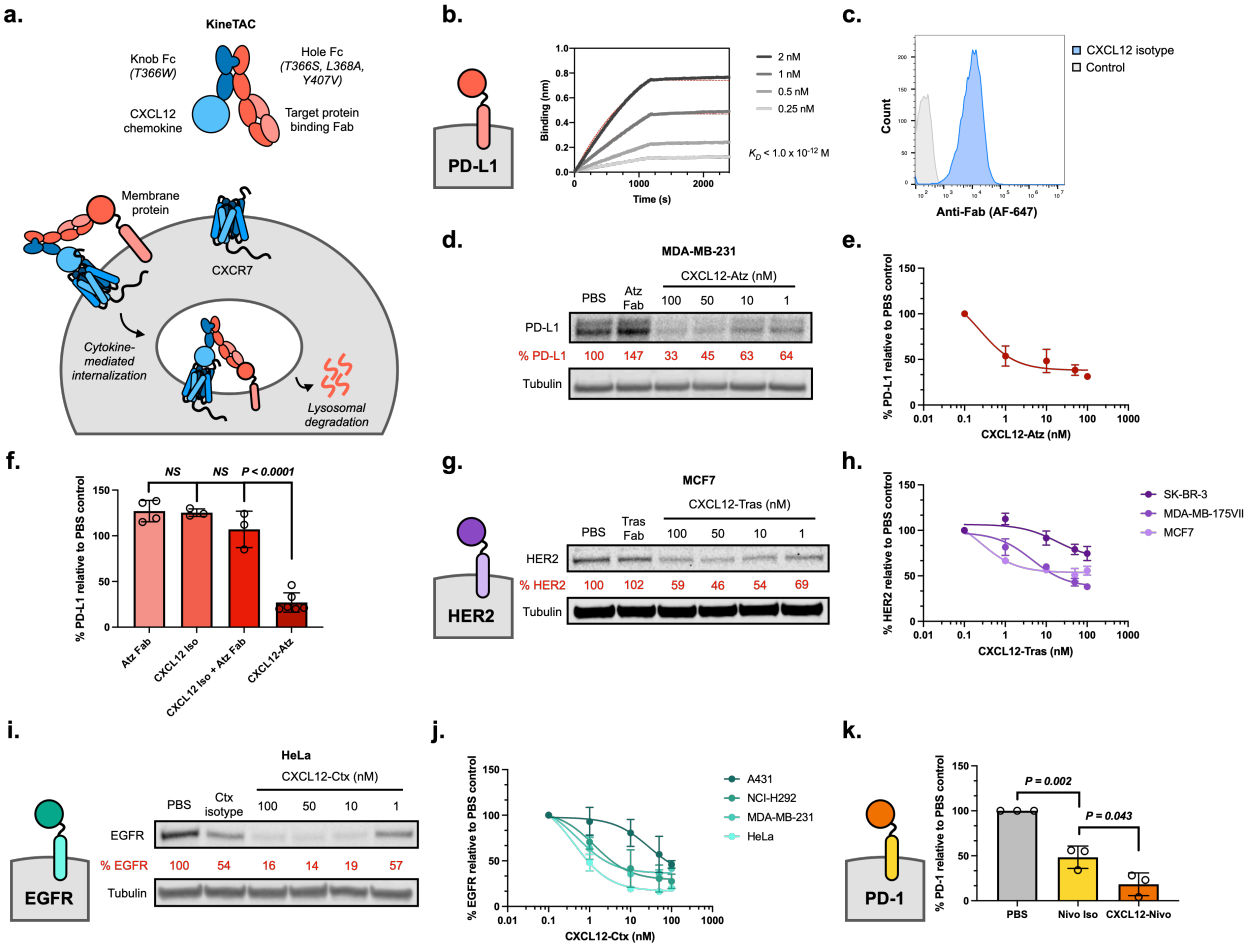

Figure 1.1: KineTAC platform can be broadly applied to targeting therapeutically relevant cell surface proteins for targeted protein degradation.
a, Schematic of the KineTAC concept for targeting cell surface proteins for lysosomal degradation via CXCL12-mediated endocytosis. **b,** Multipoint BLI measurement of CXCL12-Atz shows high affinity to PD-L1 Fc fusion. **c,** Flow cytometry showing CXCL12 isotype binding on MDA-MB-231 cells endogenously expressing CXCR7. **d-e,** Dose escalation experiment showing PD-L1 degradation in MDA-MB-231 cells after 24 hr treatment with CXCL12-Atz. **f,** PD-L1 levels as determined by western blotting after 24 hr treatment of MDA-MB-231 with 100 nM atezolizumab Fab, CXCL12 isotype, combination of Atz Fab and CXCL12 isotype, or CXCL12-Atz. **g,** Dose escalation experiment showing HER2 degradation in MCF7 cells after 24 hr treatment with CXCL12-Tras or 100 nM trastuzumab Fab. **h,** Summary of HER2 degradation in various HER2-expressing cell lines following 24 hr treatment with CXCL12-Tras. **i,** Dose escalation showing EGFR degradation in HeLa cells after 24 hr treatment with CXCL12-Ctx or 100 nM cetuximab isotype. **j,** Summary of EGFR degradation in various EGFR-expressing cell lines following 24 hr treatment with CXCL12-Ctx. **k,** Summary of flow cytometry data demonstrating degradation of cell surface PD-1 on activated primary human CD8+ T cells. Data are representative of at least

three independent biological replicates. Densitometry was used to calculate protein levels and normalized to PBS control. P-values were determined by unpaired two-tailed *t*-tests.

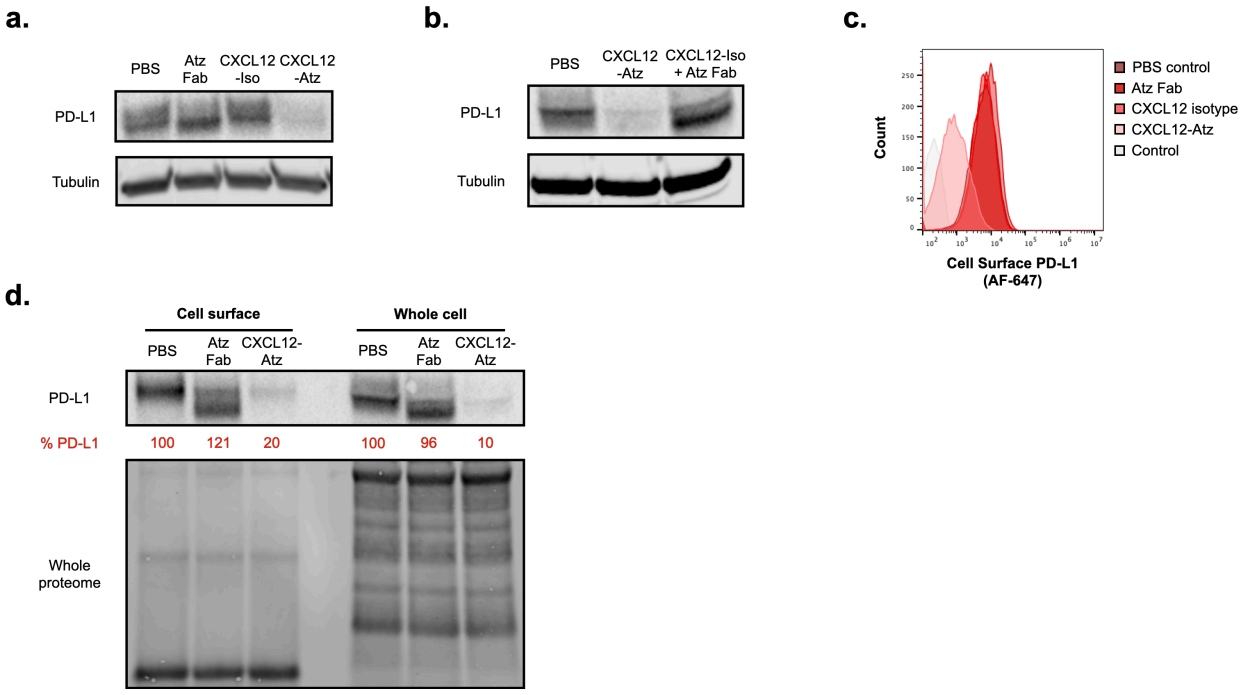

Figure 1.2: KineTACs target cell surface protein PD-L1 for degradation.
Representative western blot showing PD-L1 levels after 24 hr treatment of MDA-MB-231 cells with 100 nM of atezolizumab control, CXCL12 isotype, or CXCL12-Atz. **b,** Representative western blot showing PD-L1 levels after 24 hr treatment with MDA-MB-231 cells with 100 nM CXCL12-Atz or 100 nM CXCL12 isotype + 100 nM atezolizumab Fab. **c,** Flow cytometry showing degradation of surface PD-L1 on MDA-MB-231 cells after 24 hr treatment with 100 nM CXCL12-Atz, but not after addition of controls. **d,** Levels of cell surface and whole cell PD-L1 after 24 hr treatment of MDA-MB-231 cells with 100 nM CXCL12-Atz or atezolizumab Fab shows marginal differences between cell surface and whole cell PD-L1 levels. Data are representative of at least three independent biological replicates. Densitometry was used to calculate protein levels and normalized to PBS control.

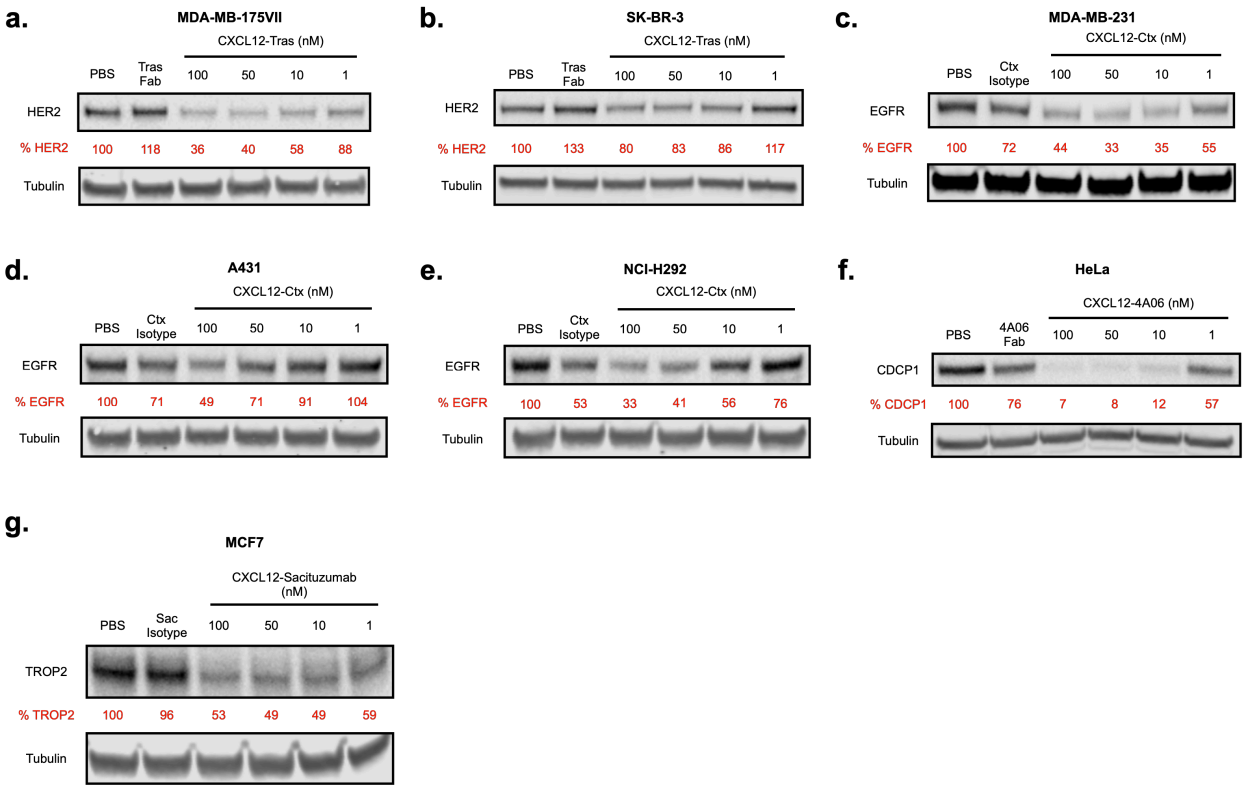

Figure 1.3: KineTACs mediate degradation of additional therapeutically relevant cell surface proteins.

Dose escalation showing HER2 degradation in **a,** MDA-MB-175VII and **b,** SK-BR-3 cells following treatment with CXCL12-Tras or 100 nM trastuzumab Fab. Dose escalation showing EGFR degradation in **c,** MDA-MB-231, **d,** A431, and **e,** NCI-H292 cells following treatment with CXCL12-Ctx or 100 nM Cetuximab isotype. **f,** Dose escalation showing CDCP1 degradation in HeLa cells following treatment with CXCL12-4A06 or 100 nM 4A06 Fab. **g,** Dose escalation showing TROP2 degradation in MCF7 cells following treatment with CXCL12-Sacituzumab or sacituzumab isotype. Data are representative of at least two independent biological replicates. Densitometry was used to calculate protein levels and normalized to PBS control.

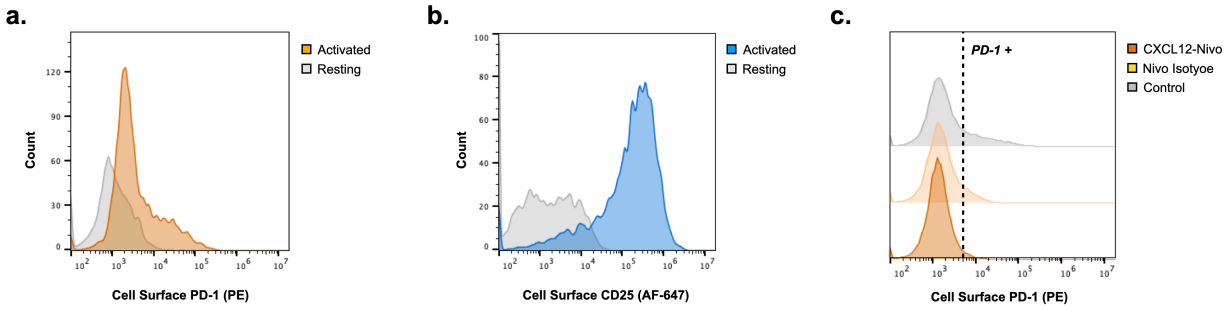

Figure 1.4: KineTACs mediate degradation of PD-1 on primary human CD8+ T cells. Representative flow cytometry showing presence of CD8+ T cell activation markers, **a,** PD-1 or **b,** CD25, following 4 day incubation with activation cocktail (IL-2, IL-15, anti-CD3, anti-CD28). **c,** Representative flow demonstrating cell surface PD-1 degradation on activated primary human CD8+ T cells following 24 hr treatment with 100 nM CXCL12-Nivo or nivolumab isotype.

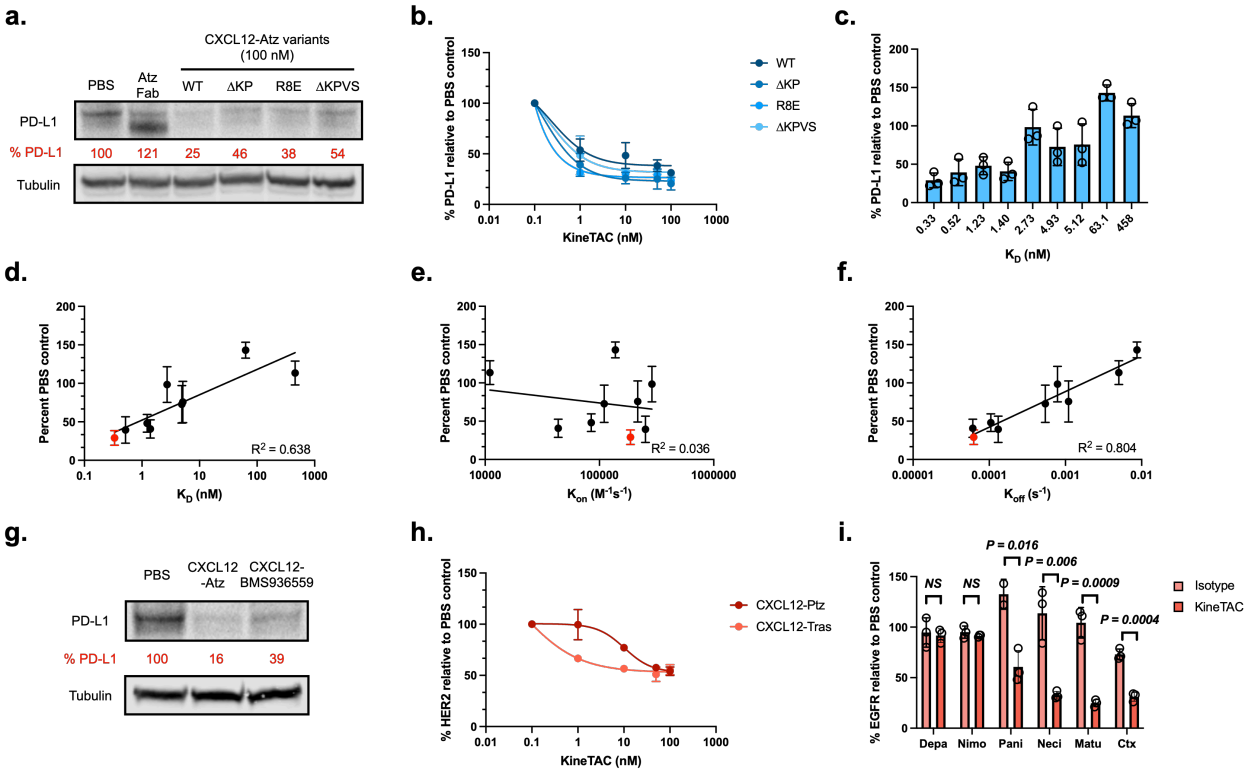

Figure 1.5: Requirements for efficient KineTAC-mediated degradation of target proteins. **a-b,** PD-L1 levels after treatment with agonistic and antagonistic 100 nM CXCL12-Atz variants for 24 hr in MDA-MB-231 cells. **c,** PD-L1 levels after treatment with 100 nM CXCL12-Atz wild-type or alanine mutants for 24 hr in MDA-MB-231 cells. Correlation of PD-L1 levels as calculated by densitometry and either **d,** K_D, **e,** K_{on}, or **f,** K_{off}. Wild-type atezolizumab is indicated in red. Error bars represent the standard deviation of three biological replicates. **g,** PD-L1 levels after treatment with 100 nM CXCL12-Atz or pH-sensitive binder CXCL12- BMS936559 for 24 hr in MDA-MB-231 cells. **h,** HER2 levels after treatment with 100 nM CXCL12-Tras or CXCL12-Ptz in MCF7 cells demonstrate that different HER2 epitope binders can be used for degradation. **i,** EGFR levels after treatment with 100 nM of CXCL12-Ctx, Depa, Nimo, Matu, Neci, or Pani in HeLa cells demonstrate that there is dependence on EGFR binding epitope for efficient degradation. Data are representative of at least three independent biological replicates. Densitometry was used to calculate protein levels and normalized to PBS control. P-values were determined by unpaired two-tailed *t*-tests. Linear regression analysis using GraphPad Prism was used to calculate the coefficient of determination (R^2) to determine correlation.

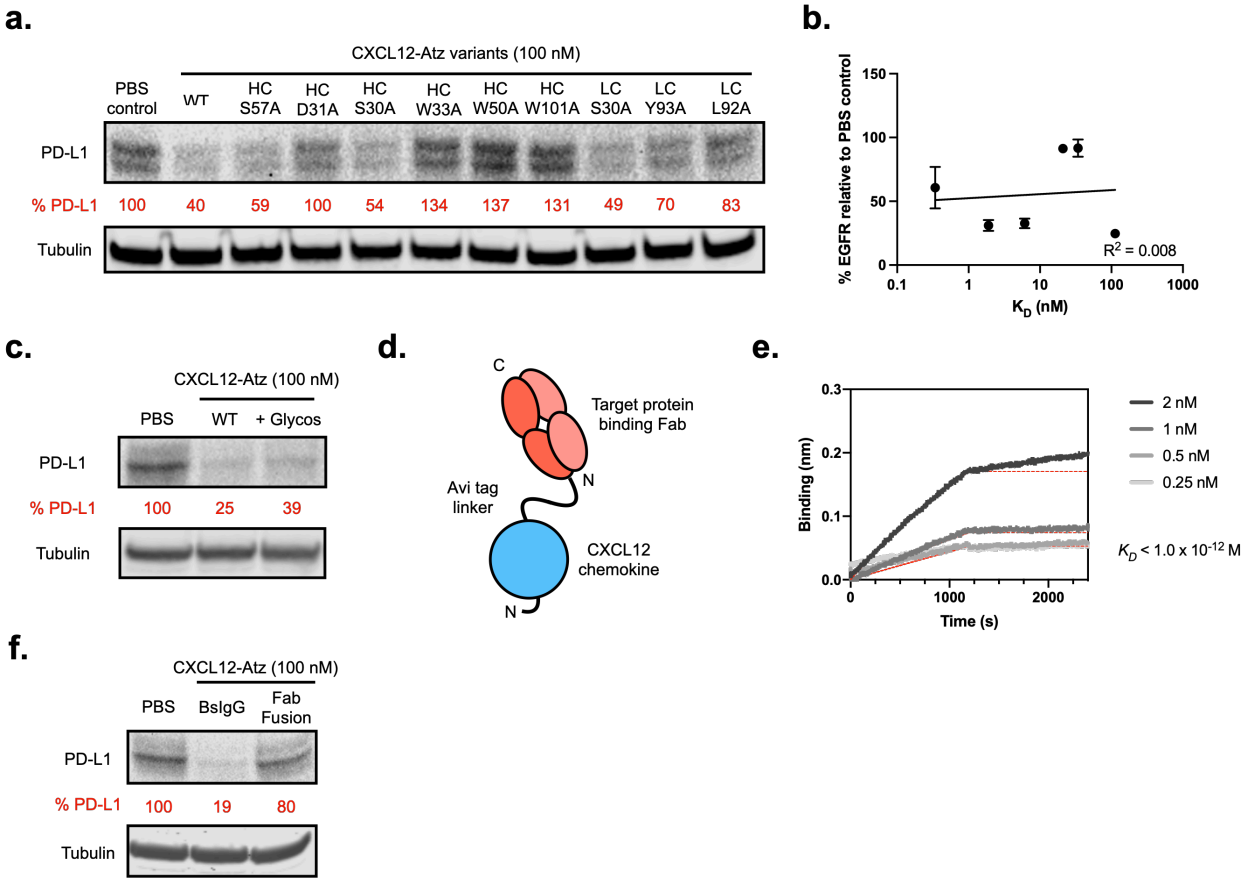

Figure 1.6: Additional requirements for efficient KineTAC-mediated degradation of PD-L1. **a,** Representative western blot showing PD-L1 levels after treatment with 100 nM CXCL12-Atz wild-type or alanine mutants for 24 hr in MDA-MB-231 cells. **b,** Correlation of EGFR levels to K_D as calculated by densitometry after treatment with 100 nM CXCL12-Depa, Nimo, Pani, Neci, Matu, or Ctx for 24 hrs in HeLa cells. **c,** PD-L1 levels after treatment with 100 nM aglycosylated or glycosylated CXCL12-Atz for 24 hr in MDA-MB-231 cells. **d,** Schematic of CXCL12-Atz Fab fusion construct where CXCL12 chemokine is fused to the N-terminus of atezolizumab Fab via an Avi tag linker. **e,** Multipoint BLI measurement of CXCL12-Atz Fab fusion shows high affinity to PD-L1 Fc fusion. **f,** PD-L1 levels after treatment with 100 nM CXCL12-Atz bispecific or Fab fusion for 24 hr in MDA-MB-231 cells shows that the bispecific construct is superior in degrading PD-L1. Data are representative of at least two independent biological replicates. Densitometry was used to calculate protein levels and normalized to PBS control.

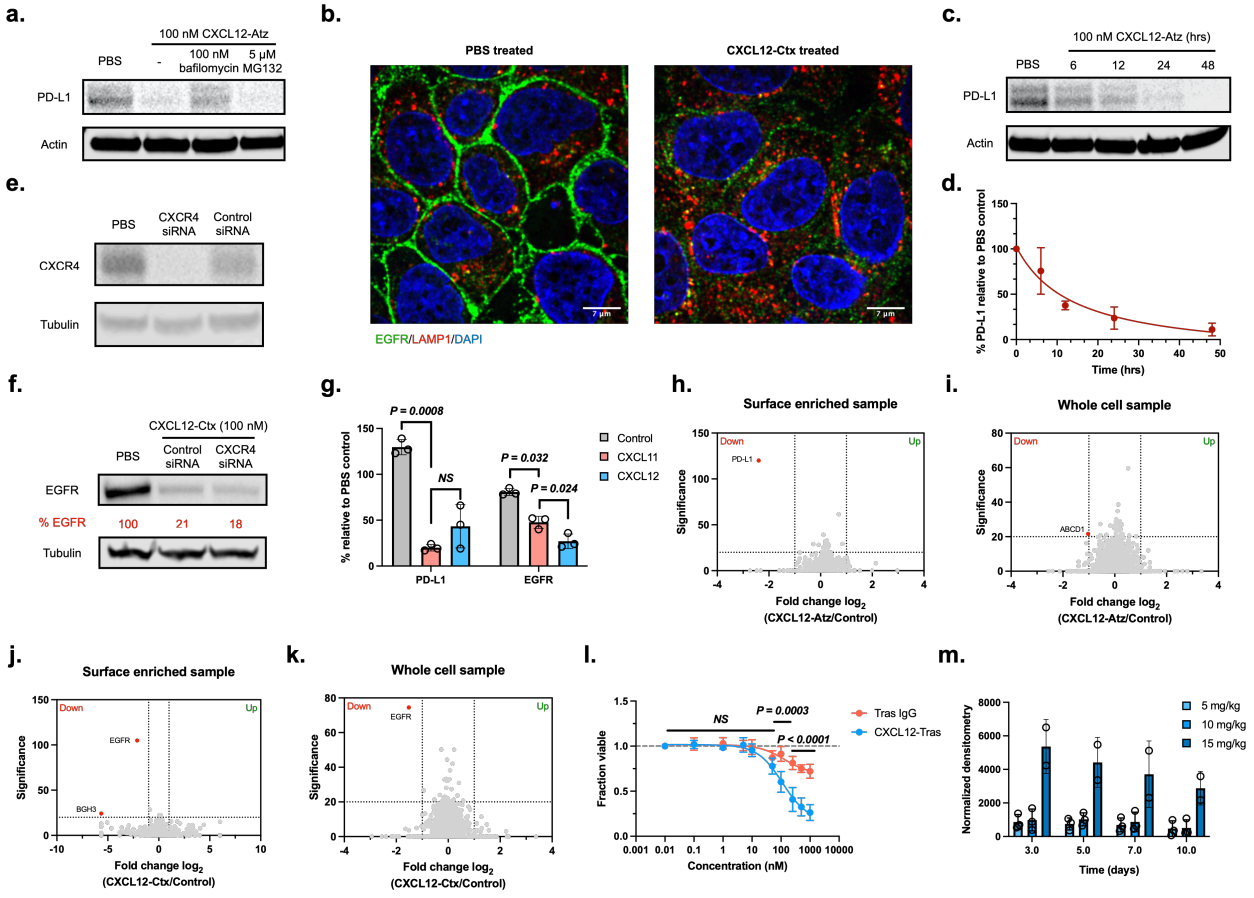

Figure 1.7: KineTACs mediate target degradation in a highly selective, lysosome-, time-, and CXCR7-dependent manner.

a, 1 hr pre-treatment of MDA-MB-231 cells with either 100 nM bafilomycin or 5 µM MG-132 followed by 24 hr treatment with 100 nM CXCL12-Atz indicates that CXCL12-Atz degrades PD-L1 in a lysosome-dependent manner. **b,** Confocal microscopy images of HeLa cells treated for 24 hr with 100 nM CXCL12-Ctx shows near complete removal of EGFR from the cell surface. **c-d,** Time course experiment showing degradation of PD-L1 at various time points after treatment with 100 nM CXCL12-Atz. Error bars represent the standard deviation of three biological replicates. **e,** siRNA knockdown of CXCR4 in HeLa cells after 48 hr transfection is dependent on CXCR4-targeting siRNA pool. **f,** EGFR levels are unchanged after siRNA knockdown of CXCR4 for 48 hrs followed by 24 hr treatment with 100 nM CXCL12-Ctx in HeLa cells. **g,** PD-L1 in MDA-MB-231 or EGFR in HeLa cells are degraded after 24 hr treatment with 100 nM CXCL11-Atz or CXCL11-Ctx, respectively, at levels similar to CXCL12 KineTACs. Fold change in abundance of **h,** surface enriched or **i,** whole cell MDA-MB-231 proteins detected using quantitative proteomics analysis after 48 hr treatment with 100 nM CXCL12-Atz reveals highly selective PD-L1 degradation. Fold change in abundance of **j,** surface enriched or **k,** whole cell HeLa proteins detected using quantitative proteomics analysis after 48 hr treatment with 100 nM CXCL12-Ctx reveals highly selective EGFR degradation. Data are the mean of two biological replicates and two technical replicates. **l,** *In vitro* potency of CXCL12-Tras in HER2-expressing breast cancer cell line MDA-MB-175VII demonstrates superior cell killing compared to trastuzumab IgG. Six biological replicate data points are shown. **m,** Quantification of CXCL12-Tras plasma levels in

male nude mice injected intravenously at 5, 10, or 15 mg/kg. Data are representative of three independent mice. Densitometry was used to calculate protein levels and normalized to whole protein levels. P-values were determined by unpaired two-tailed *t*-tests.

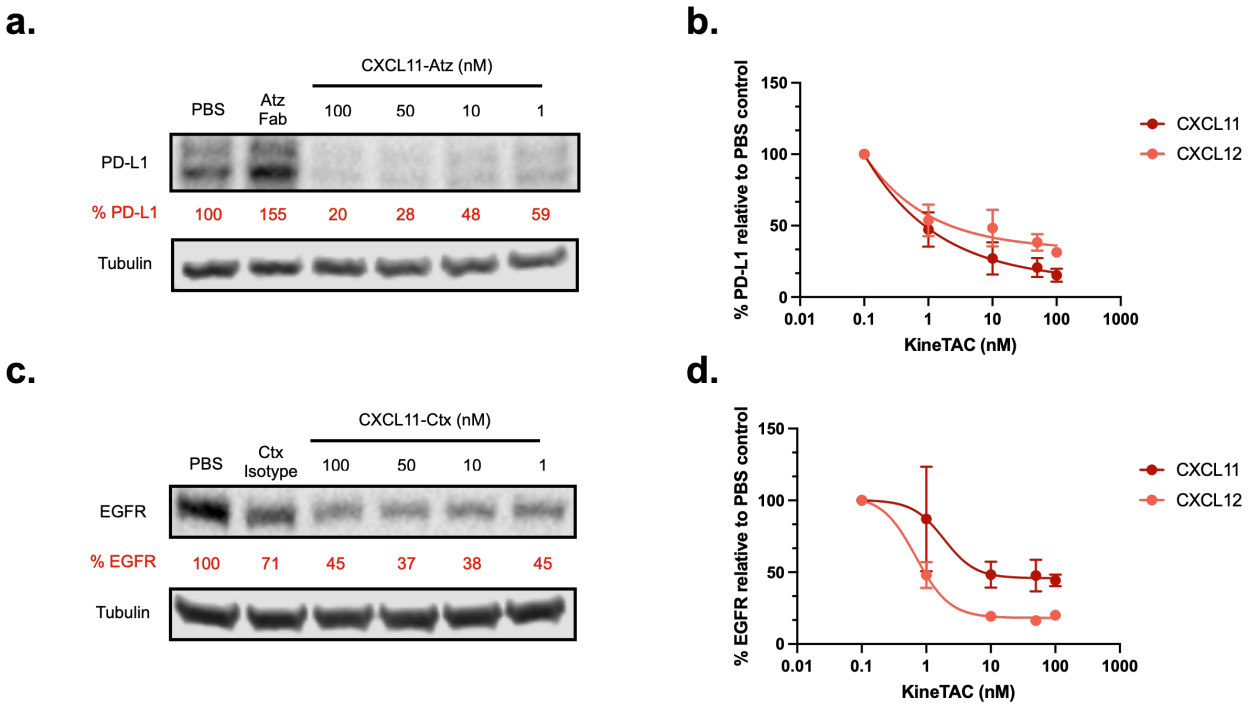

Figure 1.8: CXCL11 is an alternative CXCR7-targeting KineTAC that degrades PD-L1 and EGFR.

a, Representative western blot showing PD-L1 degradation in MDA-MB-231 cells following 24 hr treatment with various doses of CXCL11-Atz or 100 nM atezolizumab Fab. **b,** Comparison of dose response of PD-L1 degradation in MDA-MB-231 cells following 24 hr treatment with CXCL11- or CXCL12-Atz. **c,** Representative western blot showing EGFR degradation in HeLa cells following 24 hr treatment with various doses of CXCL11-Ctx or 100 nM cetuximab isotype. **d,** Comparison of dose response of EGFR degradation in HeLa cells following 24 hr treatment with CXCL11- or CXCL12-Ctx. Data are representative of at least three independent biological replicates. Densitometry was used to calculate protein levels and normalized to PBS control.

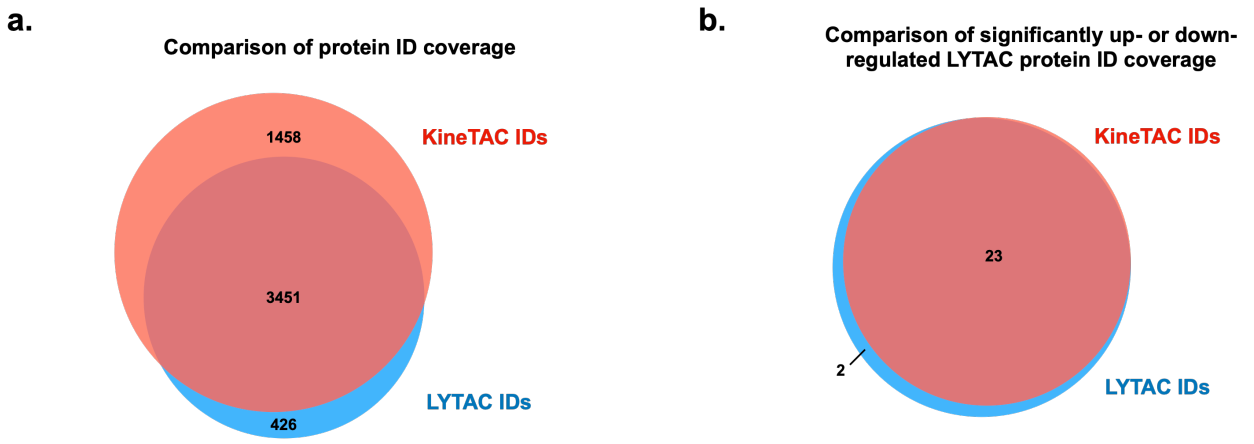

Figure 1.9: Comparison of KineTAC and LYTAC proteomics datasets for EGFR lysosomal degradation.
a, Comparison between KineTAC and LYTAC whole cell quantitative proteomics experiments in HeLa cells shows large overlap in total proteins identified. **b,** 23 of 25 proteins that were significantly up- or down-regulated in the LYTAC dataset were identified in the KineTAC whole cell dataset.

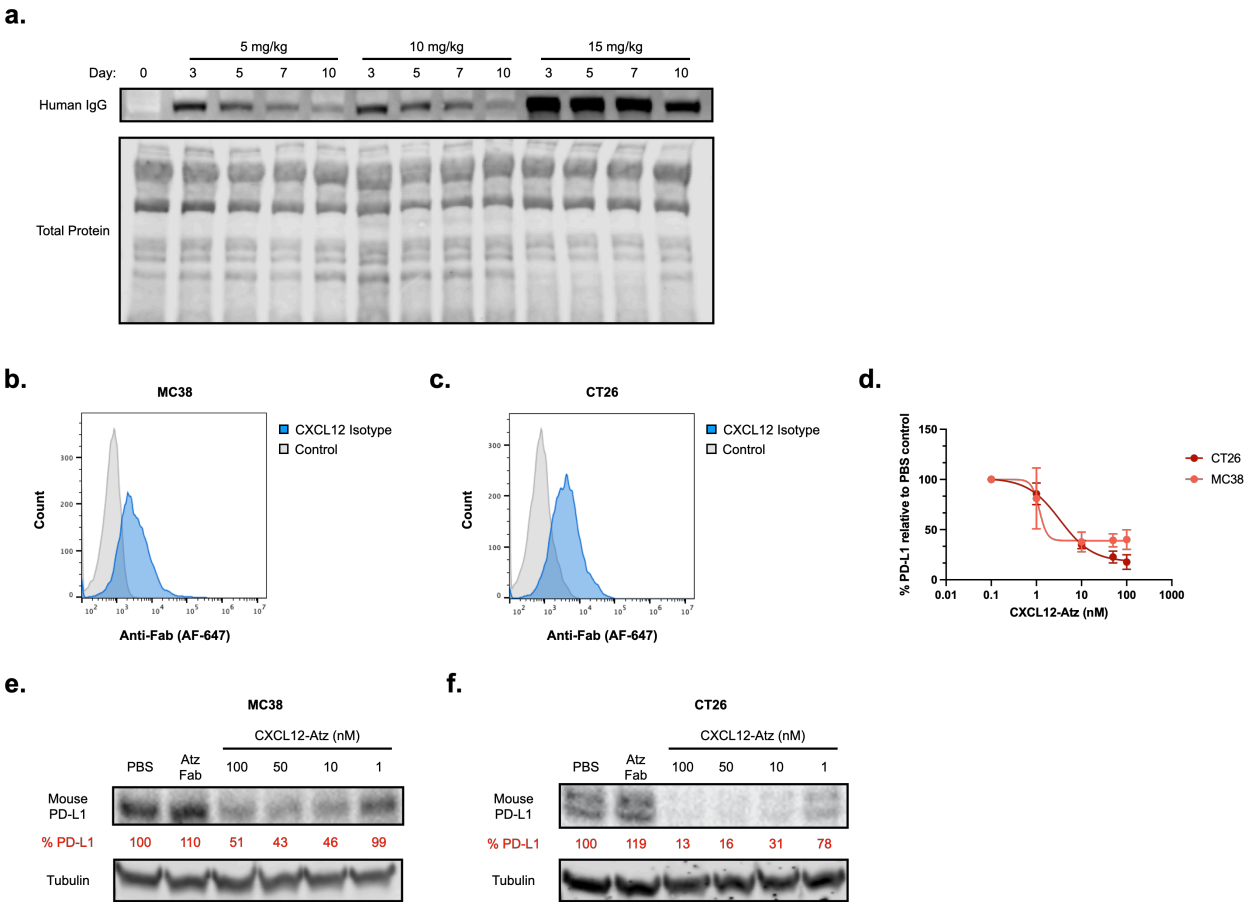

Figure 1.10: CXCL12-Atz is cross-reactive to mouse cell lines and stable *in vivo*.
Flow cytometry showing that human CXCL12 is cross reactive and binds to the surface of **a,** MC38 and **b,** CT26 mouse cell lines. **c,** Dose escalation showing mouse PD-L1 degradation in MC38 and CT26 cells following 24 hr treatment with CXCL12-Atz. Representative western blot of dose escalation showing mouse PD-L1 degradation in **d,** MC38 or **e,** CT26 mouse cells following 24 hr treatment with CXCL12-Atz and mouse IFNg. **f,** Representative western blot showing plasma levels of CXCL12-Tras in male nude mice injected intravenously with 5, 10, or 15 mg/kg. Data are representative of three independent biological replicates or mice. Densitometry was used to calculate protein levels and normalized to PBS control.

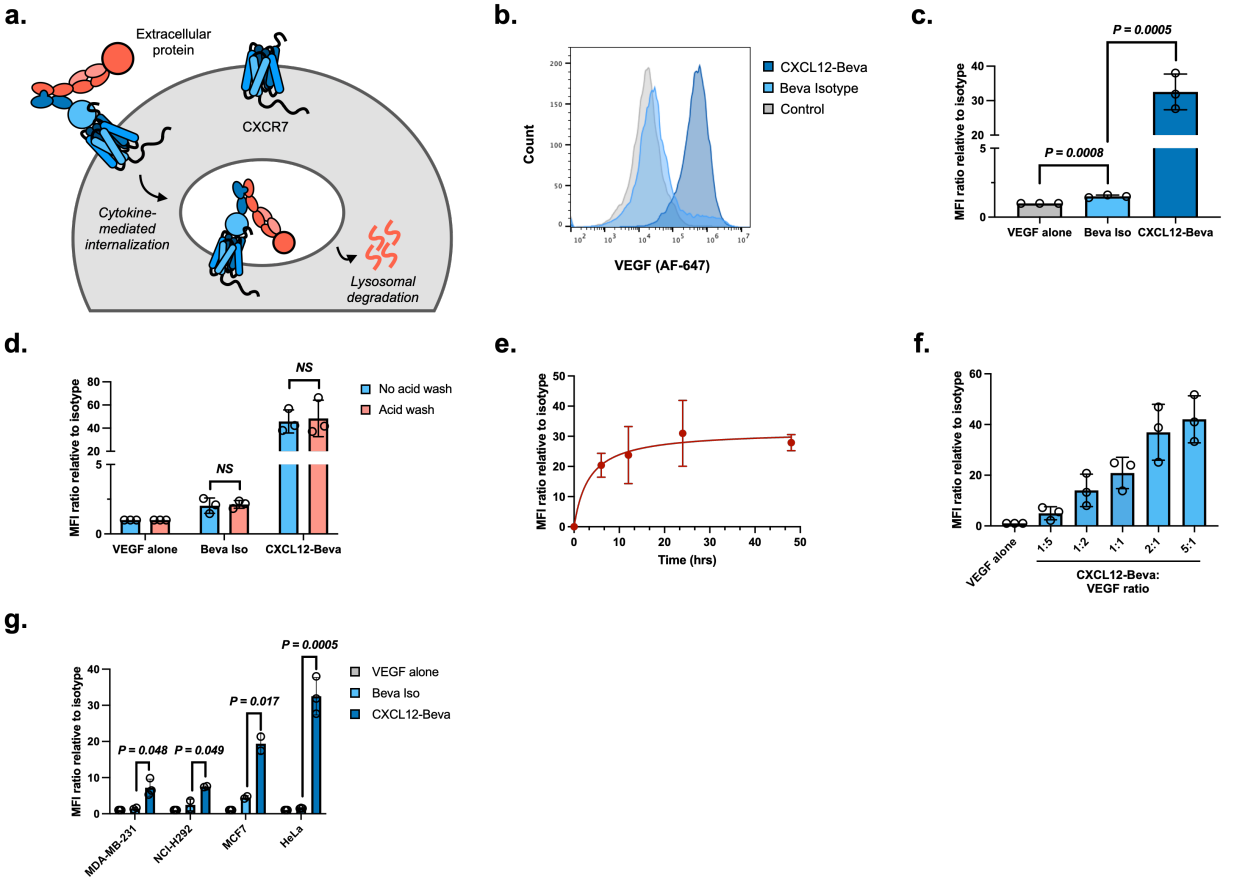

Figure 1.11: KineTACs enable intracellular uptake of soluble extracellular proteins.
a, Schematic of KineTAC concept for targeting extracellular proteins for lysosomal degradation. **b,** Representative flow cytometry showing shift in median fluorescence intensity in HeLa cells treated for 24 hr with 50 nM CXCL12-Beva and 25 nM VEGF-647 compared to VEGF alone. **c,** Summary of flow cytometry demonstrating shift in median fluorescence intensity in HeLa cells following 24 hr treatment with 50 nM CXCL12-Beva or isotype controls and 25 nM VEGF-647 compared to VEGF alone. **d,** Comparison of HeLa cells washed with PBS or acid wash buffer (0.2M glycine, 0.15M NaCl, pH 3.0) following 24 hr treatment with 50 nM CXCL12-Beva or isotype controls and 25 nM VEGF-647. No significant change in median fluorescence intensity suggests that fluorescence shift represents intracellular VEGF-647. **e,** Time course experiment showing increase in VEGF-647 uptake overtime in HeLa cells treated with 50 nM CXCL12-Beva and 25 nM VEGF-647. **f,** HeLa cells treated for 24 hr with varying ratios of CXCL12-Beva to VEGF, at constant 25 nM VEGF-647, demonstrate that increasing the KineTAC:VEGF ratio increases VEGF uptake. **g,** Panel of cell lines for VEGF-647 uptake experiments, demonstrating increased VEGF-647 uptake for CXCL12-Beva treated cells compared to bevacizumab isotype or VEGF alone. Median fluorescence intensity (MFI) was measured using live cell flow cytometry. Data are representative of at least three independent biological replicates and error bars show standard deviation between replicates. P-values were determined by unpaired two-tailed *t*-tests. Fold changes are reported relative to incubation with soluble ligand alone.

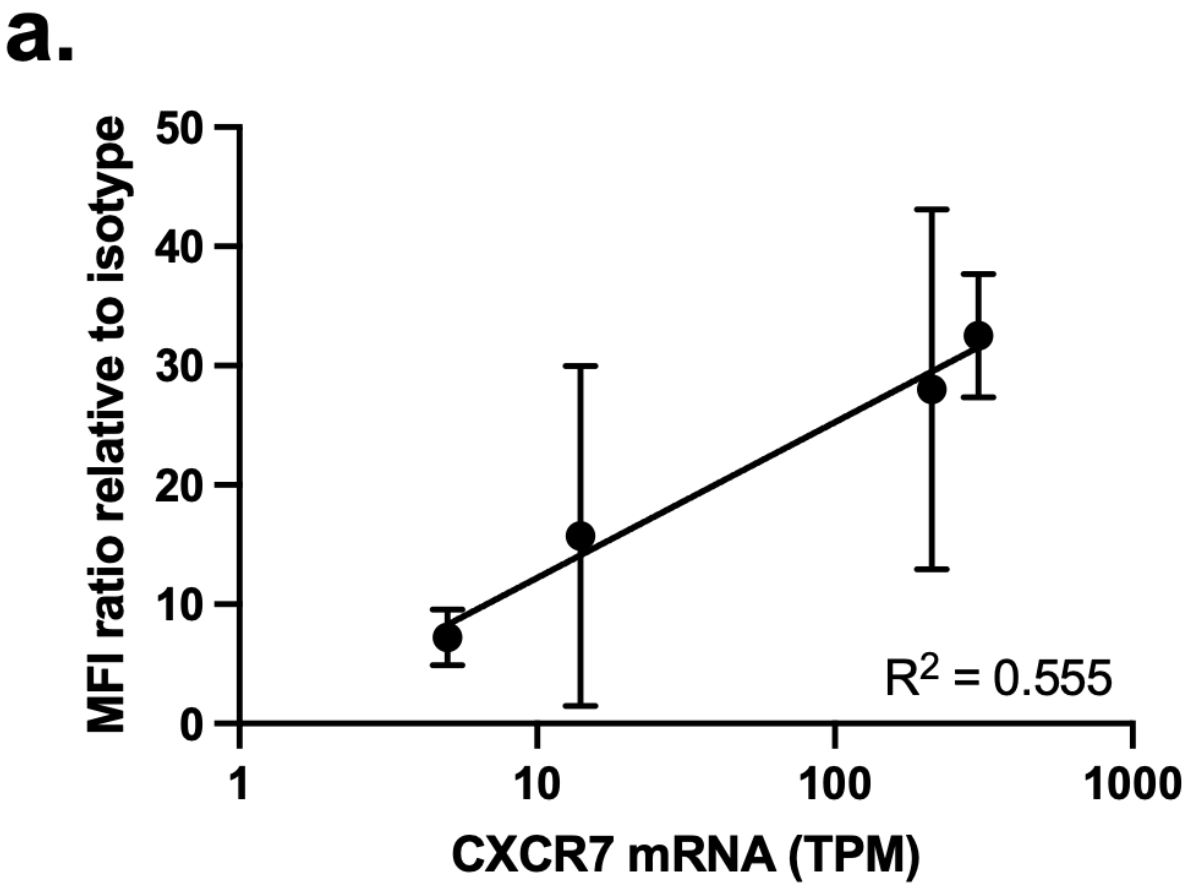

Figure 1.12: Intracellular uptake of VEGF is correlated to CXCR7 transcript levels.
a, Correlation of VEGF uptake as calculated by flow cytometry to CXCR7 transcript levels. Error bars represent the standard deviation of three biological replicates. Linear regression analysis using GraphPad Prism was used to calculate the coefficient of determination (R^2) to determine correlation.

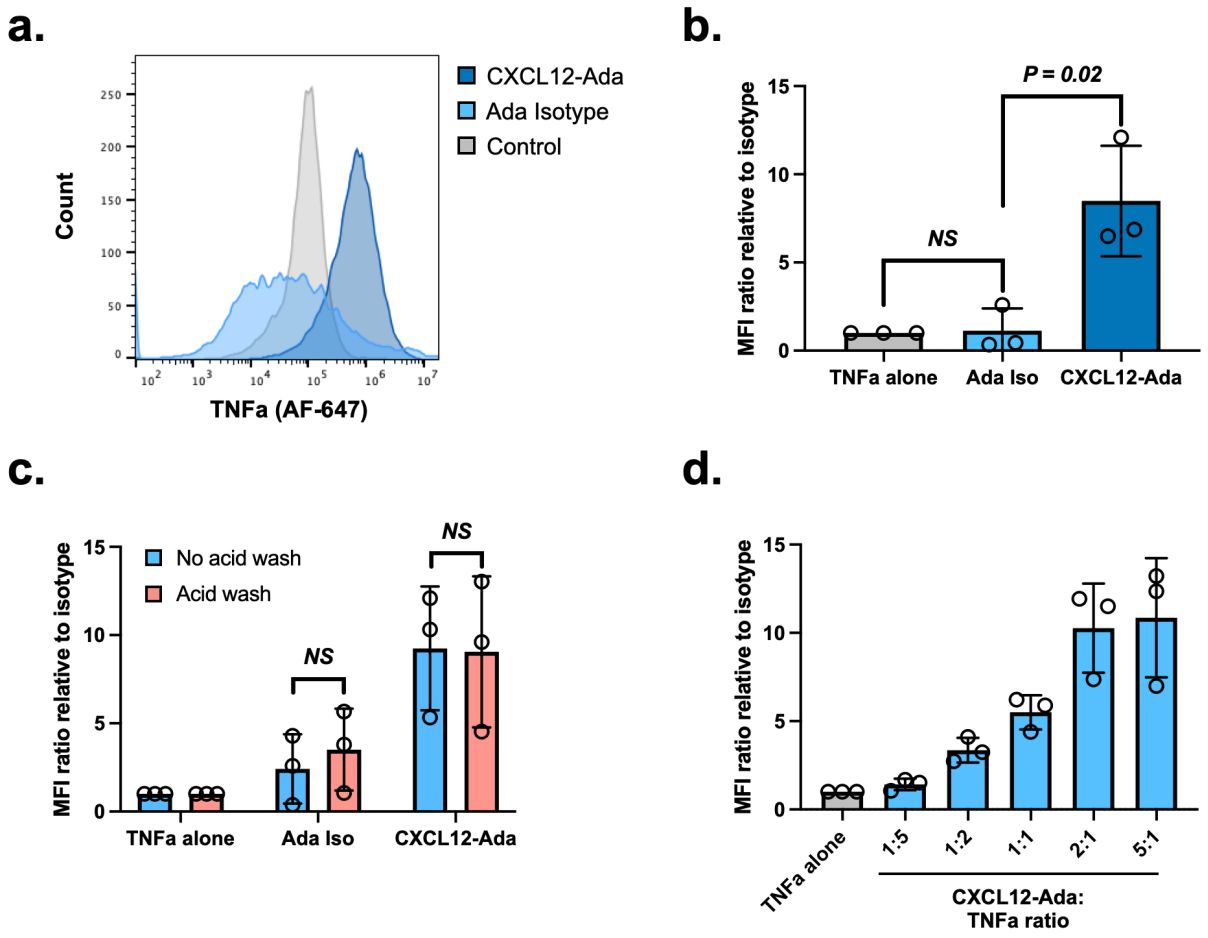

Figure 1.13: KineTACs mediate the uptake of extracellular TNFa.
a, Representative flow cytometry showing shift in median fluorescence intensity in HeLa cells treated for 24 hr with 50 nM CXCL12-Ada and 25 nM TNFa-647 compared to TNFa alone. **b,** Summary of flow cytometry demonstrating shift in median fluorescence intensity in HeLa cells following 24 hr treatment with 50 nM CXCL12-Ada or adalimumab isotype, and 25 nM TNFa-647 compared to TNFa alone. **c,** Comparison of HeLa cells washed with PBS or acid wash buffer (0.2M glycine, 0.15M NaCl, pH 3.0) following 24 hr treatment with 50 nM CXCL12-Ada or adalimumab isotype and 25 nM TNFa-647. No significant change in median fluorescence intensity demonstrates that fluorescence shift represents intracellular TNFa-647. **d,** HeLa cells treated for 24 hr with varying ratios of CXCL12-Ada to TNFa, at constant 25 nM TNFa-647, demonstrate that increasing the KineTAC:TNFa ratio increases TNFa uptake. P-values were determined by unpaired two-tailed *t*-tests. Fold changes are reported relative to incubation with soluble ligand alone.

Table 1.1: Summary of CXCR7:target ratios and maximal degradation (D_{max}) for each cell surface KineTAC target.

Target Protein	Cell Line	CXCR7:Target mRNA Ratio[1]	D_{max} (%)
PD-L1	MDA-MB-231	0.5	69
HER2	MCF7	8.6	51
HER2	MDA-MB-175VII	1.3	62
HER2	SK-BR-3	0.03	26
EGFR	HeLa	6.0	84
EGFR	A431	0.4	54
EGFR	MDA-MB-231	0.2	66
EGFR	NCI-H292	0.1	74
PD-1	Primary CD8+ T cells	N/A	82
CDCP1	HeLa	5.6	94
TROP2	MCF7	1.8	51

[1] mRNA levels are from the Cancer Cell Line Encyclopedia RNA-seq of 934 cancer cell lines and Genentech's RNA-seq of 675 commonly used human cancer cells.

Table 1.2: *In vitro* binding affinities of atezolizumab alanine mutants to PD-L1.

Mutant	K_D (nM)	k_{on} ($M^{-1}s^{-1}$)	k_{off} (s^{-1})
WT	0.33	1.87×10^{5}	6.24×10^{-5}
S57A HC	0.52	2.53×10^{5}	1.31×10^{-4}
D31A HC	4.93	1.10×10^{5}	5.44×10^{-4}
S30A HC	1.40	4.36×10^{4}	6.09×10^{-5}
W33A HC	N.D.	N.D.	N.D.
W50A HC	63.1	1.38×10^{5}	8.69×10^{-3}
W101A HC	458	1.10×10^{4}	5.02×10^{-3}
S30A LC	1.23	8.48×10^{4}	1.05×10^{-4}
Y93A LC	5.12	2.16×10^{5}	1.10×10^{-3}
L92A LC	2.73	2.88×10^{5}	7.86×10^{-4}

Chapter 2

Antibody-drug conjugates for the targeted degradation of multi-pass membrane proteins

Abstract

Targeted protein degradation has become an effective strategy to block the function of a malignant protein and presents a rival to conventional inhibition approaches. Most degraders are currently limited to targeting cytoplasmic or nuclear proteins due to the recruitment of intracellular E3 ligases and thus dependence on an intracellular mechanism of action. Recently, various approaches have been described which expand targeted degradation to the extracellular proteome, including KineTACs (described in Chapter 1), AbTACs, and LYTACs. However, all these approaches use antibodies as the target binding molecule. Multi-pass membrane proteins are a class of cell surface proteins that have traditionally been difficult to target with antibody binders. This is due to lack of a large, structured ectodomain, conformational flexibility, and lack of specificity when targeting a conserved N-terminal region. Despite the lack of antibody therapies, there have been a wealth of small molecule binders described for various multi-pass membrane proteins. Here, we describe a novel approach, termed antibody-drug conjugate PROTACs (ADC-TACs), that enables the targeted lysosomal degradation of multi-pass membrane proteins. ADC-TACs are comprised of a selective small molecule, which binds to a multi-pass membrane protein, conjugated to an antibody, which binds to and recruits a cell surface E3 ligase. Simultaneous engagement of the membrane protein and the E3 ligase leads to lysosomal degradation of the target protein. We demonstrate proof-of-concept for ADC-TACs targeting the G protein-coupled receptor adenosine 2a receptor (A2AR). We find that conjugation site and linker length can influence the extent of A2AR degradation. Overall, this strategy is generalizable to targeting various classes of multi-pass membrane proteins and other membrane proteins lacking antibody binders.

Introduction

The concept of targeted degradation has emerged in the last two decades as an attractive alternative to conventional inhibition. Small molecule inhibitors primarily work through occupancy-driven pharmacology, resulting in temporary inhibition in which the therapeutic effect is largely dependent on high potency. On the other hand, PROteolysis TArgeting Chimeras (PROTACs) utilize event-driven pharmacology to degrade proteins in a catalytic manner.[7] Traditionally, PROTACs are heterobifunctional small molecules composed of a ligand binding a protein of interest chemically linked to a ligand binding an E3 ligase. The recruitment of an E3 ligase enables the transfer of ubiquitin onto the protein of interest, which is subsequently polyubiquitinated and recognized by the proteasome for degradation (**Figure 2.1**). In many cases, PROTACs have proven efficacious over the small molecule inhibitors alone, and several candidate PROTACs have progressed to clinical trials for treating human cancers and other diseases.[10,42,43] Despite these successes, small molecule PROTACs are largely limited to targeting intracellular proteins. Given this challenge, there is a need for novel technologies that expand the scope of targeted degradation to membrane proteins.

Recently, our lab has developed a method termed antibody-based PROTACs (AbTACs) which utilize bispecific antibody scaffolds to bring membrane-bound E3 ligases in proximity to a membrane protein of interest for targeted degradation.[3] Thus far, AbTACs have shown success in using bispecific IgGs to recruit E3 ligase RNF43[44] to programmed death ligand 1 (PD-L1) for efficient lysosomal degradation. This data suggests that it is possible to use bispecific antibodies to degrade membrane proteins for which antibodies already exist or that have characteristics amenable to recombinant antibody selection strategies.[45] However, the ability to degrade multi-pass membrane proteins, such as GPCRs, remains challenging due to few extracellular-binding

antibodies existing for this target class. Here, we describe a novel approach to expand the scope of AbTACs to targeting multi-pass membrane proteins. This approach, termed antibody-drug conjugate PROTACs (ADC-TACs), comprises of an antibody targeting a cell surface E3 ligase chemically conjugated to a small molecule that specifically binds the protein of interest (**Figure 2.2**). We demonstrate proof-of-concept that conjugation of an adenosine 2a receptor (A2AR) agonist to an RNF43 targeting antibody leads to efficient degradation of A2AR *in vitro*. Furthermore, we find that A2AR degradation is dependent on site of conjugation on the antibody scaffold and linker length between the small molecule and antibody. Overall, this strategy has the potential to convert any GPCR-directed small molecule into an effective degradation-based antagonist. Importantly, ADC-TACs can be generally applied to the targeted degradation of other multi-pass membrane protein classes.

Results

To determine whether it is possible to degrade GPCRs using ADC-TACs, A2AR was first targeted as a proof-of-concept. A2AR is expressed on the surface of natural killer and $CD8^+$ T cells and is primarily involved in responding to levels of adenosine in the extracellular environment. Binding of adenosine agonizes A2AR to activate a downstream signaling cascade, resulting in an increase in intracellular cyclic AMP (cAMP) levels and overall immunosuppression. This is especially evident in the tumor microenvironment, where high levels of extracellular ATP decompose to generate excess adenosine.[46] Along with the immunosuppressive role, A2AR agonism is thought to contribute to cell proliferation via the MAPK/ERK/JNK signaling pathways.[47] Given this role in cell proliferation, there has been an effort to develop antagonists to counteract agonism of the receptor in both the immune and cancer cell context. As such, A2AR is an appealing first target for applying our ADC-TAC approach towards the targeted degradation of GPCRs.

To this end, A2AR agonist CGS21680 was chosen for conjugation as it had previously been conjugated onto an Fc domain, and the crystal structure indicated that our proposed conjugation site off the solvent exposed carboxylic acid was unlikely to interfere with small molecule binding (**Figure 2.3a,** PDB: 4UHR).[48,49] Three analogs of CGS21680 with DBCO-$(PEG)_n$-NH_2 linkers of varying lengths (n=4, 6, and 9) were synthesized (**Figure 2.3b**). We hypothesized that conjugation of CGS21680 onto the variable domain of an antibody with the indicated linker lengths would be capable of spanning the interface between A2AR and RNF43. Final compounds were confirmed by LC/MS and purified by HPLC before conjugation onto previously described anti-RNF43 Fabs. To enable site-specific labeling, methionine conjugation chemistry involving oxaziridine labeling of methionines was chosen due to its high selectivity.[50] Sites were chosen that have been previously demonstrated to have both high labeling percentage and stability to hydrolysis of the sulfimide for methionine mutations.[51] To prevent off-target labeling, a methionine that was present in the H1 complementarity determining region (CDR) of the anti-RNF43 Fab was mutated to leucine. Two additional methionines that are buried in the Fab scaffold were also removed to limit unwanted labeling. As seen by multi-point biolayer interferometry (BLI), removing the endogenous methionine had little effect on binding to RNF43 Fc fusion (**Figure 2.4a**). Five sites of methionine mutation were then each incorporated into the scaffold (**Figure 2.4b**). Sites were chosen in the variable domain under the assumption that conjugation closer to the CDRs would require shorter linker lengths to the small molecule to allow simultaneous binding of E3 ligase and target protein. These mutants were expressed as Fabs in the periplasm of the C43 *E. coli* strain. Multi-point BLI confirmed that introduction of methionine at the five sites had little to no effect on binding to RNF43 Fc fusion (**Figure 2.4a**).

Next, we sought to determine whether the anti-RNF43 Fab mutants could be selectively labeled with the azide derivative of the piperidine-derived oxaziridine 8 and the CGS21680-DBCO conjugates (**Figure 2.5a**). All mutants showed robust and rapid labeling with the oxaziridine reagent after 30 min incubation, with little unlabeled antibody remaining in solution (**Figure 2.5b, Figure 2.6a**). Furthermore, all mutants showed robust click chemistry labeling after overnight incubation with CGS21680-DBCO, with near complete conversion to agonist-labeled product (**Figure 2.5c, Figure 2.6b**). Ability of oxaziridine- and agonist-labeled Fabs to bind RNF43 Fc fusion was confirmed with multi-point BLI as compared to unlabeled Fabs (**Figure 2.5d**). Furthermore, we find that the conjugation sites are highly stable at both room temperature and 37ºC after 3 days (**Figure 2.7a-c**). These conjugates were used for testing $A_{2a}R$ degradation *in vitro*.

To determine if an ADC-TACs could degrade endogenous A2AR, a MOLT-4 derived line that co-expresses A2AR and RNF43 was used for degradation experiments. Cells were dosed with either PBS control, 100 nM CGS21680 alone, or varying concentrations of ADC-TAC (1-100 nM) and A2AR levels analyzed by western blotting. Excitingly, dose-dependent degradation of endogenous A2AR was observed for multiple antibody-small molecule conjugates tested, with maximal degradation of 50-60% observed (**Figure 2.8a-b**). Interestingly, a "hook effect", characteristic of over saturation by bispecific molecules,[52] was observed in which higher concentrations of conjugate led to decreased degradation of A2AR. We also observed a dependence on the site of antibody conjugation as well as linker length. Specifically, LC S7M and R66M conjugation sites show dose-dependent degradation while other labeling sites do not. Furthermore, the PEG4 linker length conjugates at these sites show successful degradation while the slightly longer PEG6 and 9 conjugates do not. Going forward, conjugates that show efficient

degradation in preliminary experiments will be triaged for further validation and understanding of degradation mechanism using pathway inhibitors. Successful degraders will be tested in other cell lines known to co-express A2AR and RNF43. Future studies will also focus on expanding the ADC-TAC target scope to other therapeutically relevant GPCRs, such as chemokine receptors CXCR4 and CCR5.

Methods

Cell lines

Cell lines were grown and maintained in T75 (Thermo Fisher Scientific) flasks at 37ºC and 5% CO2. MOLT-4 CCR5+ cells were grown in RPMI-1640 supplemented with 10% fetal bovine serum (FBS) and 2% geneticin. MOLT-4 CCR5+ cells were obtained from the NIH AIDS Reagent Program.

Antibody cloning, expression, and purification

Anti-RNF43 Fab LC S7M single mutation was introduced using Gibson Assembly. Fabs were expressed in *E. coli* C43(DE3) Pro+ using an optimized autoinduction media and purified by Protein A affinity chromatography. Purity and integrity of Fabs were assessed by SDS-PAGE and intact mass spectrometry.

Synthesis of DBCO-CGS21680

Commercially available CGS21680 (Cayman Chemical, 17126, 5 mg, 0.01 mmol) was added to 1.5 equivalents of 1-[Bis(dimethylamino)methylene]-1H-1,2,3-triazolo[4,5-b]pyridinium 3-oxide hexafluorophosphate (HATU, 6 mg, 0.015 mmol) and 4 equivalents of 4 equivalents N,N-

diisopropylethylamine (7 µL, 0.04 mmol) in 2 mL of dimethylformamide and stirred at room temperature for 10 min. Then, 1.5 equivalents DBCO-PEG4-amine (BroadPharm, BP-23958, 5 mg, 0.015 mmol) was added to reaction flask and stirred at room temperature overnight. The reaction mixture was concentrated under reduced pressure. Crude product was purified by high performance liquid chromatography (HPLC). The final product was lyophilized and isolated as a pale yellow powder (4.8 mg, 48% yield). ESI-HRMS calculated $[M+H^+]$ = 1005.48; found 1005.54.

Conjugation of engineered anti-RNF43 Fab with oxaziridine and DBCO-CGS21680

For conjugation with oxaziridine, 50 µM Fab was incubated with 5 molar equivalents of oxaziridine azide for 30 min at room temperature in phosphate-buffer saline (PBS). The reaction was quenched with 10 molar equivalents methionine. The antibody was buffer exchanged into PBS and desalted using a 0.5-mL Zeba 7-kDa desalting column (Thermo Fisher Scientific). Then, 10 molar equivalents of DBCO-CGS21680 was added and incubated at room temperature overnight. The agonist-labeled conjugate was desalted using the 0.5-mL Zeba 7-kDa desalting column to remove excess DBCO-CGS21680. Full conjugation at each step was monitored by intact mass spectrometry using a Xevo G2-XS Mass Spectrometer (Waters).

Stability experiments

Labeled anti-RNF43 Fabs were incubated either at room temperature (25ºC) or 37ºC for 3 days. Conjugation was monitored by intact mass spectrometry using a Xevo G2-XS Mass Spectrometer (Waters).

Degradation assays

Cells at 1 million cells/mL were treated with antibody-drug conjugate, agonist, or antagonist in complete growth medium. After 24 hrs, cells were pelleted by centrifugation (300xg, 5 min, 4ºC). Cell pellets were lysed with RIPA buffer containing cOmplete mini protease inhibitor cocktail on ice for 40 min. Lysates were spun at 16,000xg for 10 min at 4ºC and protein concentrations were normalized using BCA assay. 4x NuPAGE LDS sample buffer and 2-mercaptoethanol (BME) was added to the lysates. Equal amounts of lysates were loaded onto a 4-12% Bis-Tris gel and ran at 200V for 37 min. The gel was incubated in 20% ethanol for 10 min and then transferred onto a polyvinylidene difluoride (PVDF) membrane. The membrane was blocked in PBS with 0.1% Tween20 + 5% bovine serum albumin (BSA) for 30 min at room temperature with gentle shaking. Membranes were co-incubated overnight with rabbit-anti-A2aR (Abcam, ab3461, 1:1000) and mouse-anti-tubulin (Cell Signaling Technologies, DM1A, 1:1600) at 4ºC with gentle shaking in PBS + 0.2% Tween20 + 5% BSA. Membranes were washed four times with tris-buffered saline (TBS) + 0.1% Tween20 and then co-incubated with HRP-anti-rabbit IgG (Cell Signaling Technologies, 7074S, 1:2000) and 680RD goat anti-mouse IgG (LI-COR, 926-68070, 1:10000) in PBS + 0.2% Tween20 + 5% BSA for 1 hr at room temperature. Membranes were washed four times with TBS + 0.1% Tween20, then washed with PBS. Membranes were first imaged using an OdysseyCLxImager (LI-COR). SuperSignal West Pico PLUS Chemiluminescent Substrate was then added and image using a ChemiDoc Imager (BioRad). Band intensities were quantified using Image Studio Software (LI-COR).

Figures and Tables

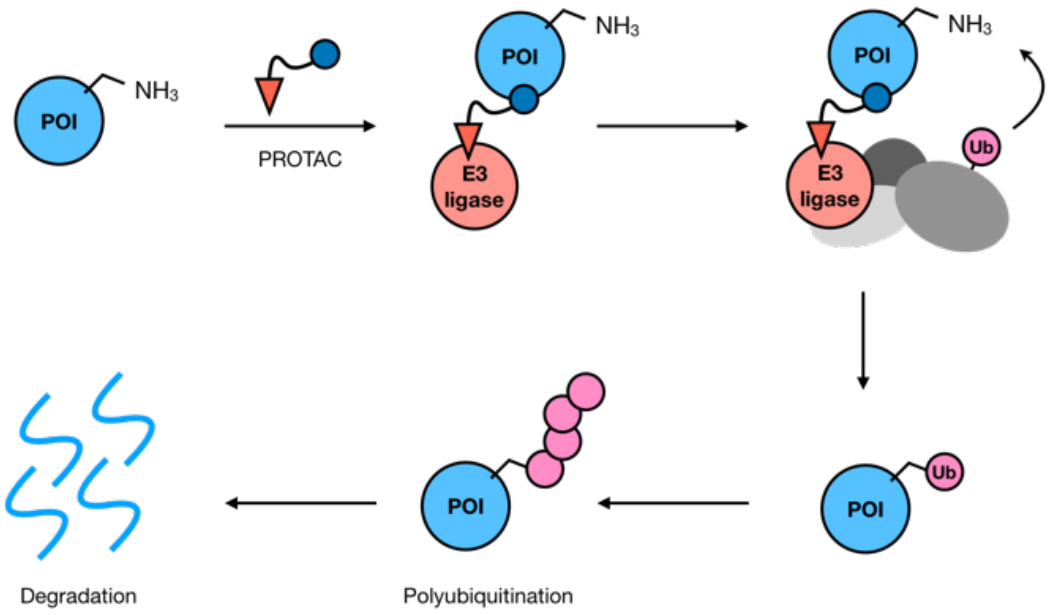

Figure 2.1: Mechanism of action of traditional bifunctional small molecule degraders. Schematic of targeted protein degradation by proteolysis targeting chimeras (PROTACs). The heterobifunctional PROTAC small molecule engages the protein of interest (POI) and E3 ligase simultaneously. Ternary complex formation between the POI and the E3 ligase enables the transfer of ubiquitin onto the POI, which is then subsequently polyubiquitinated and degraded by the proteasome.

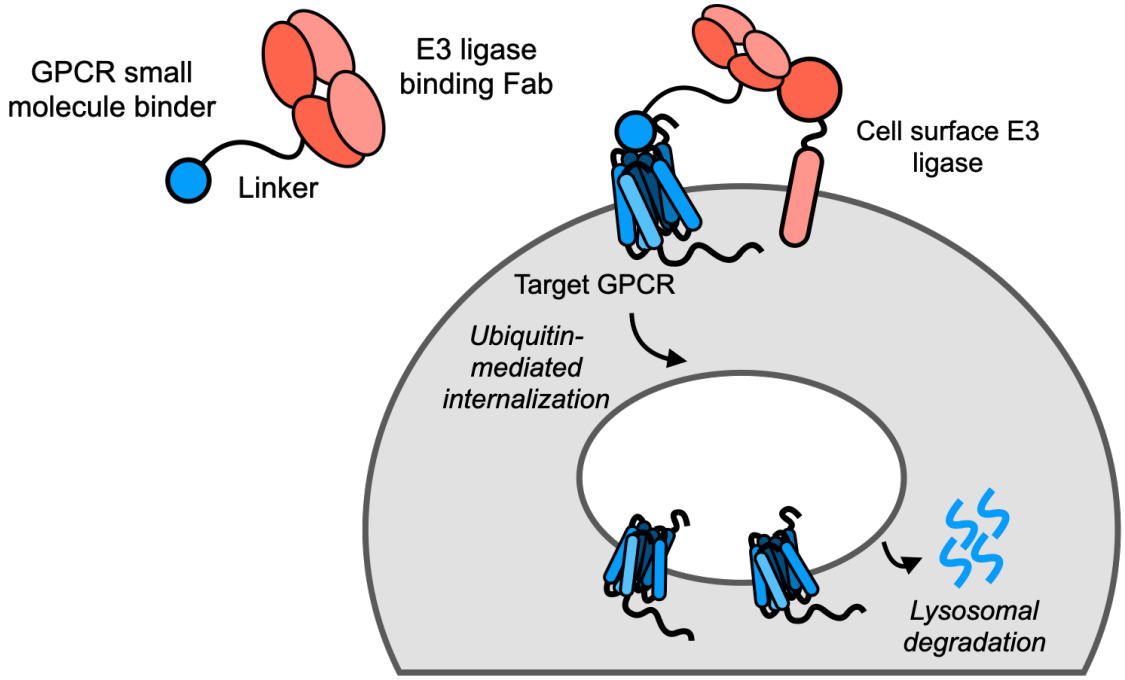

Figure 2.2: ADC-TACs for the targeted degradation of multi-pass membrane proteins. Schematic of ADC-TAC concept in which a small molecule binding the multi-pass membrane protein of interest is chemically fused to an antibody targeting a membrane tethered E3 ligase. Recruitment of the E3 ligase to the protein of interest enables ubiquitination of the target protein and subsequent internalization and lysosomal degradation.

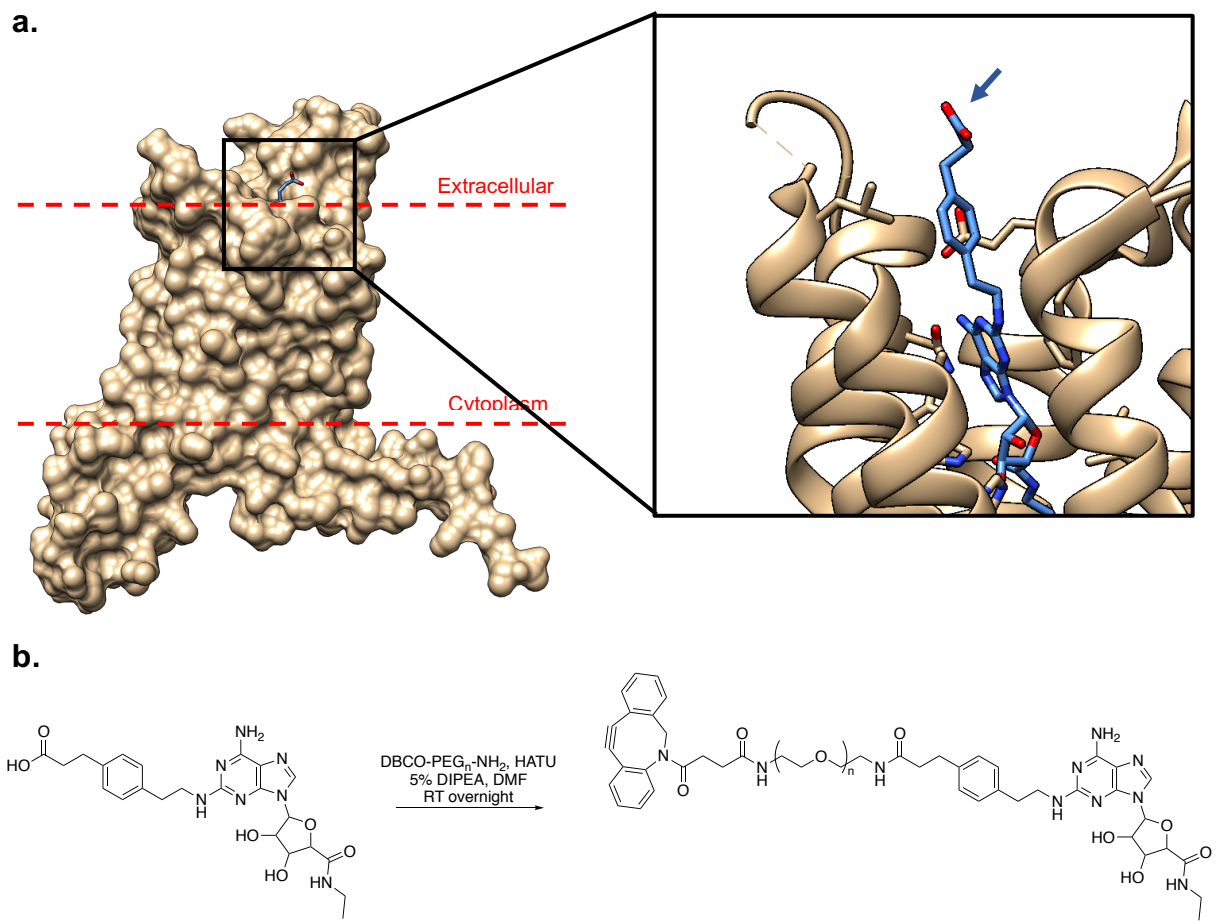

Figure 2.3: Synthesis of CGS21680-PEG$_n$-DBCO derivatives for click chemistry.
a, Crystal structure of CGS21680 bound to the adenosine 2a receptor (PDB: 4UHR) shows that the carboxylic acid on CGS21680 is solvent exposed out of the ligand binding pocket. **b,** Schematic for the synthesis of CGS21680 derivatives for click chemistry onto the anti-RNF43 Fabs. DBCO-PEG amine was coupled to the carboxylic acid on CGS21680 via HATU coupling with 5% DIPEA and DMF overnight at room temperature.

a.

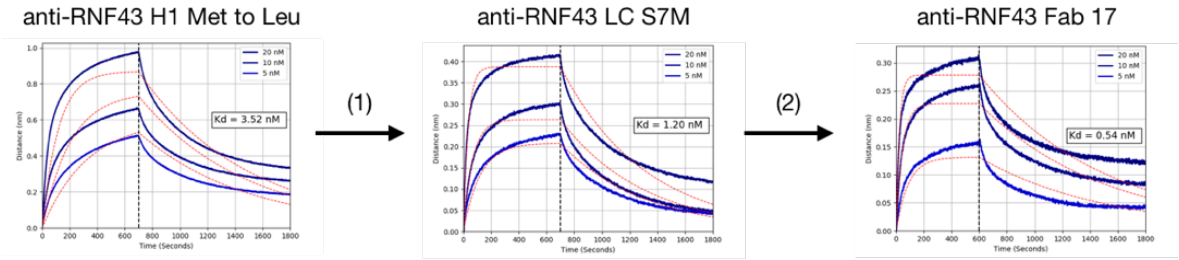

b.

Mutation site	Labeling %	Stability %
LC S7M	100	56
LC T20M	100	58
LC R66M	68	99
LC T74M	47	96
HC S21M	52	87
HC S85M	100	40

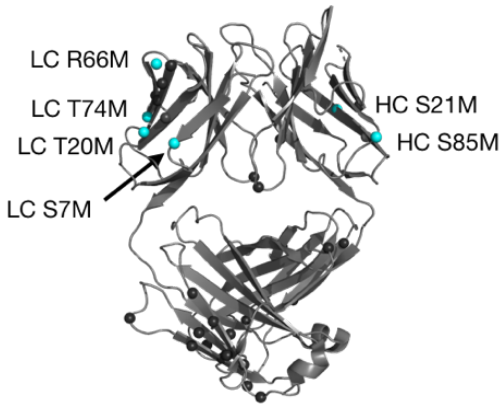

Figure 2.4: Engineering of anti-RNF43 Fab methionine mutations for bioconjugation.
a, Multipoint BLI traces of anti-RNF43 Fabs binding to immobilized RNF43 Fc fusion after introduction of various point mutations. Mutation of H1 methionine to leucine does not impact binding to RNF43. Further introduction of site-specific methionine into anti-RNF43 Fab does not alter binding affinity. **b,** Sites of methionine mutations introduced into anti-RNF43 Fab scaffold. Stability is percent labeling after 3 days at 37ºC. Trastuzumab with sites highlighted in teal for visualization (PDB: 1FVE).

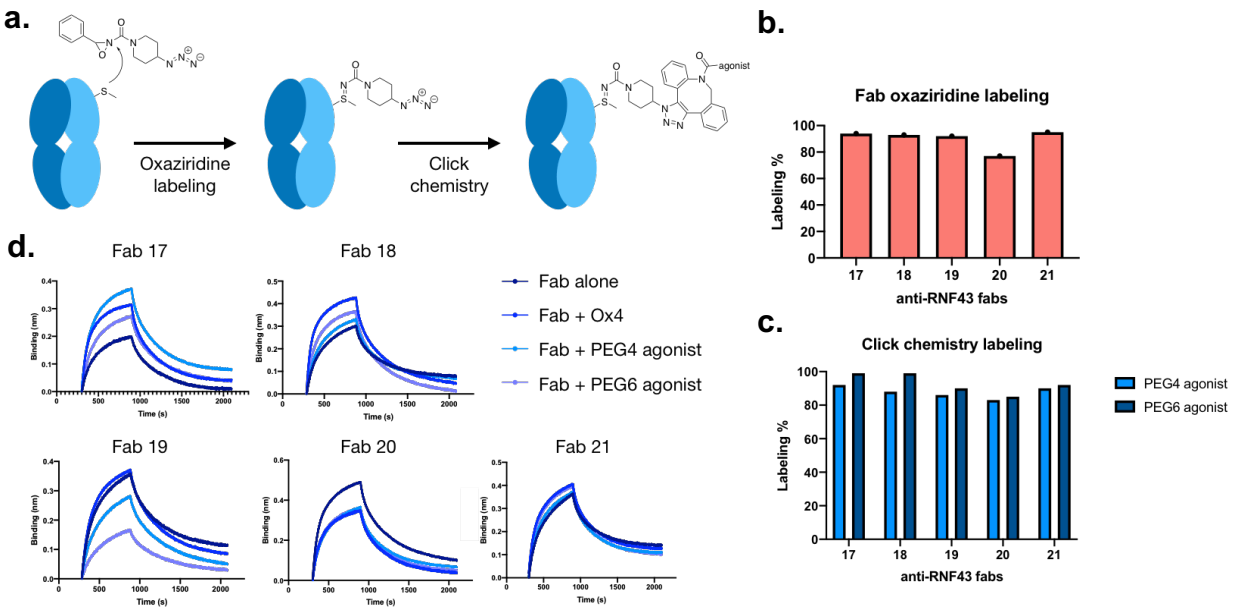

Figure 2.5: Bioconjugation labeling and characterization of A2AR targeting ADC-TACs. **a,** Schematic of ADC-TAC conjugation strategy where anti-RNF43 Fabs with site-specific methionine mutations are first labeled with oxaziridine azide followed by click chemistry labeling with CGS21680-DBCO conjugates. **b,** Labeling percentage of anti-RNF43 Fabs following 30 min incubation with 5 equivalents oxaziridine azide as monitored by LC/MS. **c,** Labeling percentage of oxaziridine labeled anti-RNF43 Fabs following overnight incubation with 10 equivalents CGS21680-DBCO conjugates as monitored by LC/MS. **d,** Single point BLI traces of various labeled and unlabeled anti-RNF43 Fab constructs binding to immobilized RNF43 Fc fusion show that Fab labeling does not impact binding.

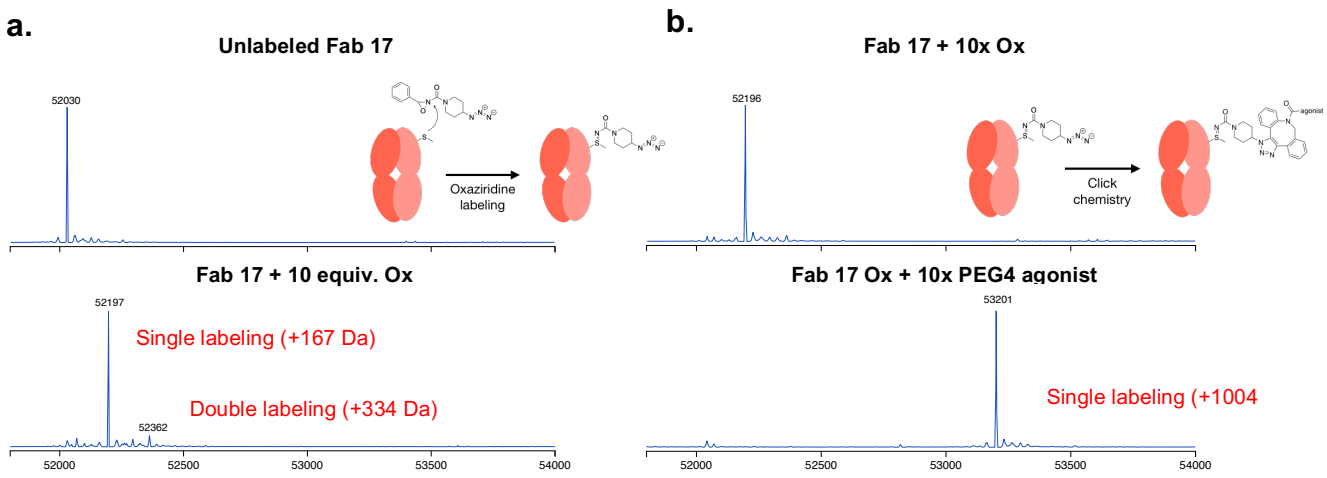

Figure 2.6: Representative mass spectrometry traces of anti-RNF43 Fab labeling.
a, Representative LC/MS data showing mass of unlabeled Fab 17 (52030 Da) compared to mass of oxaziridine labeled Fab 17 (52197 Da), demonstrating successful labeling of anti-RNF43 Fabs. **b,** Representative LC/MS data showing mass of oxaziridine labeled Fab 17 (52196 Da) compared to mass of PEG4 CGS21680-DBCO labeled Fab 17 (53201 Da), demonstrating successful click chemistry reaction to make final ADC-TACs.

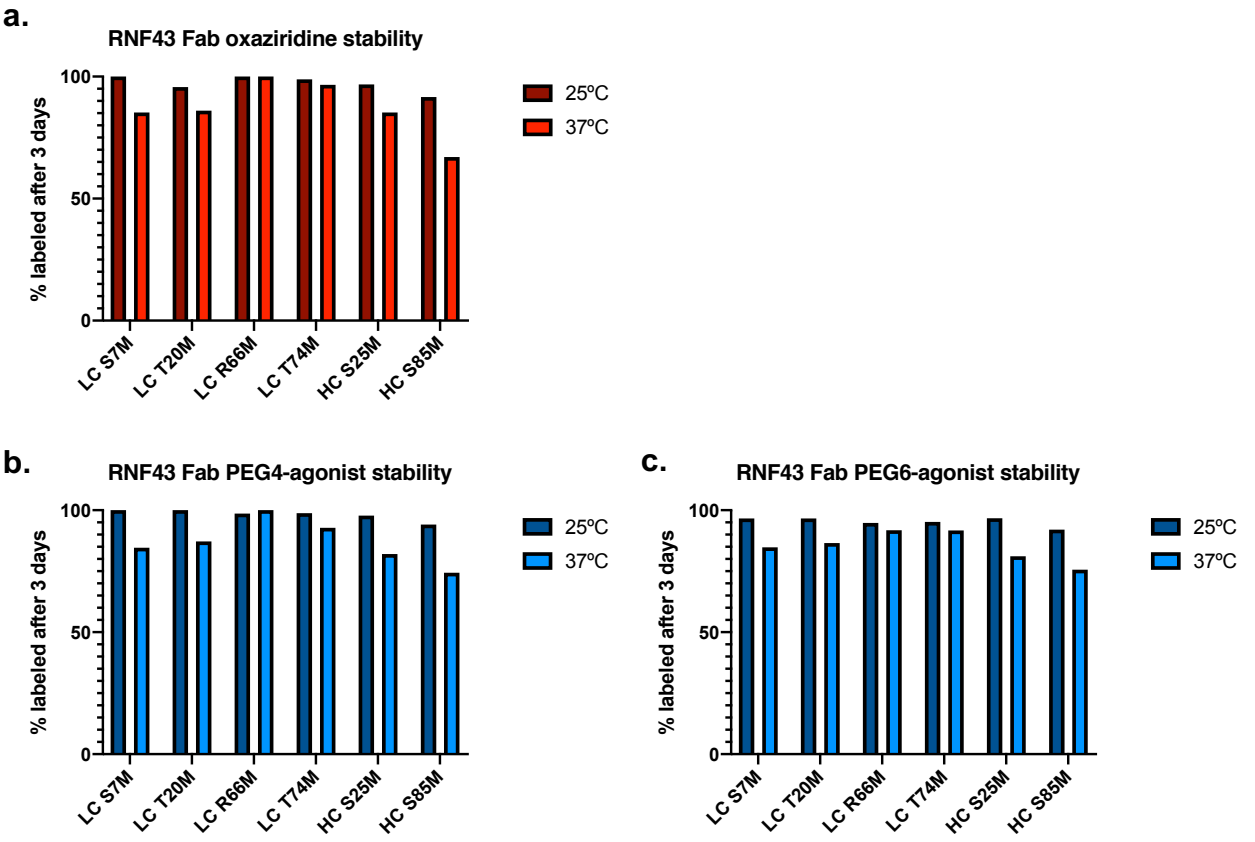

Figure 2.7: Anti-RNF43 Fab conjugation sites are stable after 3 days.
Stability data showing percent labeling remaining of anti-RNF43 Fabs conjugated with **a,** oxaziridine, **b,** PEG4 CGS21680-DBCO, or **c,** PEG6 CGS21680-DBCO after 3 days at either room temperature or 37ºC.

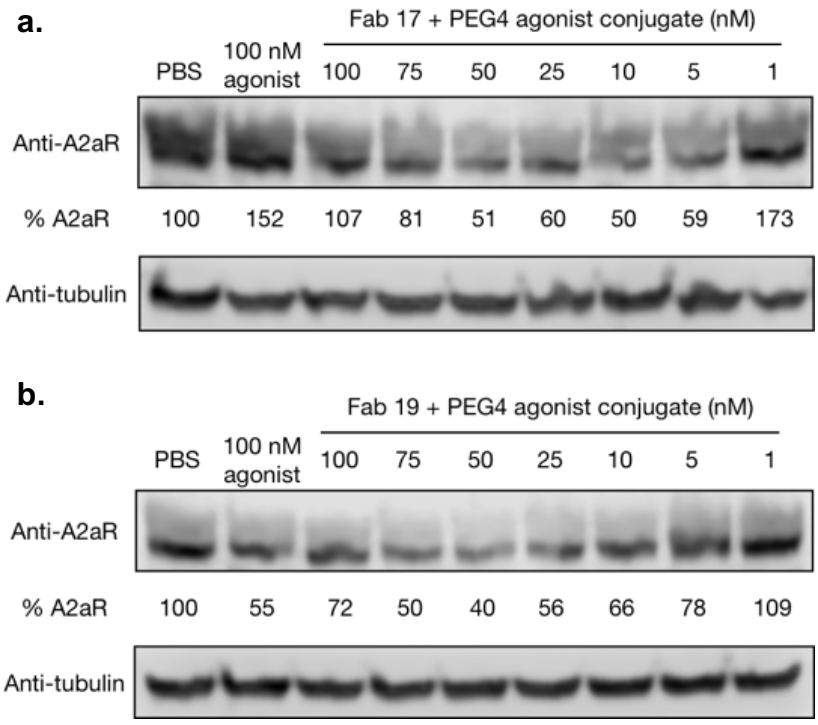

Figure 2.8: ADC-TACs mediate the degradation of A2AR.
a, Western blot showing A2AR levels following 24 hr treatment with various concentrations of LC S7M PEG4 ADC-TAC shows dose dependent degradation of A2AR in the presence of ADC-TAC but not agonist alone. **b,** Western blot showing A2AR levels following 24 hr treatment with various concentrations of LC R66M PEG4 ADC-TAC shows greater levels of A2AR degradation compared to S7M labeling site. Densitometry was used to calculate protein levels and normalized to PBS control.

Chapter 3

Bi-specific VH/Fab antibodies targeting neutralizing and non-neutralizing Spike epitopes demonstrate enhanced potency against SARS-CoV-2

Abstract

A large number of neutralizing antibodies against SARS-CoV-2 has been reported, and most directly block binding of the viral Spike receptor binding domain (RBD) to angiotensin-converting enzyme II (ACE2). Here, we deliberately exploit non-neutralizing RBD antibodies, showing they can dramatically assist in neutralization when linked to neutralizing binders. We identified Fabs by phage display that bind RBD but do not block ACE2 nor neutralize virus as IgGs. When these non-neutralizing Fabs were assembled into bi-specific VH/Fab IgGs with a neutralizing VH domain, we observed a ~25-fold potency improvement in neutralizing SARS-CoV-2 compared to the mono-specific bi-valent VH-Fc alone or the cocktail of the VH-Fc and IgG. This effect was epitope-dependent, reflecting the unique geometry of the bi-specific antibody towards Spike. Our results show that a bi-specific antibody that combines both neutralizing and non-neutralizing epitopes on Spike-RBD is a promising and rapid engineering strategy to improve the potency of SARS-CoV-2 antibodies.

Introduction

SARS-CoV-2 has emerged as a global health concern and effective therapeutics are necessary to curb the COVID-19 pandemic. Many potential therapeutic options for treating COVID-19 have been explored, from small molecules,[53] convalescent patient sera,[54] decoy receptors,[55–58] neutralizing antibodies,[59–70] and other protein scaffolds.[71–73] In particular, antibodies are advantageous due to their specific and potent binding, demonstrated pharmacokinetics, and ability to be recombinantly produced and manufactured at scale. SARS-CoV-2 antibodies have been derived from several sources, including B-cells of convalescent patients,[59,62,63,67] animal immunization,[68,70] prior coronavirus infections,[64,65] and synthetic libraries or de novo

design.[60,61,66,69,71] Most of the antibodies reported to date potently target the receptor binding domain (RBD) in the trimeric Spike protein on the surface of SARS-CoV-2,[74,59,63,75,76] which is highly immunogenic and is the key protein that mediates cellular entry via interaction with the host angiotensin-converting enzyme II (ACE2) receptor.[77] However, given the widespread global impact of this pandemic and limitations in biologic manufacturing capacities, means to further increase the potency of these antibodies and thereby decrease the dose required will be critical in meeting the global demand for therapeutics.[78] Additionally, testing different scaffolds and targeting mechanisms against coronavirus could lead to a better understanding of the most effective modalities and ultimately lead to a more resilient therapeutic arsenal against viral infections.

Following identification of an initial candidate antibody, various methods for improving antibody affinity and potency are typically employed, each with their advantages and drawbacks. Affinity maturation using mutagenesis or library display is a powerful tool to improve candidate antibodies and can screen large sequence spaces.[79] However, this process is labor intensive and may result in an antibody sequence with altered biophysical or pharmacokinetic properties that requires additional optimization. A parallel strategy to improve potency is to target multiple epitopes, either by engineering bi-specific or multi-specific molecules or by combining multiple antibodies into a cocktail.[73,80] Targeting multiple epitopes has the added benefit of decreasing the likelihood of viral escape and resistance,[68,81] and has shown promise as a powerful viral immunotherapy against viruses such as influenza[82] and HIV.[83] Indeed, several cocktails[62,81] and engineered multi-specific binders[71,84] have been shown to be effective against SARS-CoV-2. Recently, our lab demonstrated the benefits of linking multiple neutralizing epitopes on the SARS-CoV-2 Spike using bi-paratopic binders derived from variable heavy (VH) domains.[60] By linking

multiple neutralizing VH together in tandem, we were able to improve antibody potency through avidity.

Here we explored whether linking non-neutralizing binders to neutralizing binders in a bi-specific scaffold could be used as a means to rapidly improve neutralization potency. Using phage display, we identified Fabs that bind RBD but do not block ACE2 binding, and then assembled them in a knob-in-hole bi-specific IgG scaffold with VH binders that block ACE2. These VH/Fab bi-specifics have the additional advantage of avoiding the light-chain mispairing problem common to bi-specific IgGs that utilize Fabs on both arms.[85] Remarkably, the resulting VH/Fab bi-specifics are ~20 to 25-fold more potent in neutralizing both pseudotyped and authentic SARS-CoV-2 virus than the mono-specific bi-valent VH-Fc or IgG alone or as a cocktail. This effect is epitope dependent, illustrating the unique geometry that bi-specific VH/Fab IgGs could capture on the trimeric Spike protein. Our findings highlight how targeting multiple epitopes within a single therapeutic molecule, both neutralizing and non-neutralizing, can confer significant gains in efficacy, and could potentially be generalized to other therapeutic targets to rapidly enhance antibody potency.

Results

Identification and characterization of Fabs against SARS-CoV-2 Spike

Recently, we reported the identification and engineering of human variable heavy chain (VH) binders against SARS-CoV-2 Spike from an in-house VH-phage library, using a masked phage selection strategy to enrich for binders to Spike-RBD that compete with ACE2. From this process, we identified VH domains against two epitopes (sites A and B) that bind within the ACE2 binding site of SARS-CoV-2 Spike. In the bi-valent VH-Fc format, both site A and site B binders block

binding of ACE2 to Spike and neutralize pseudotyped and authentic SARS-CoV-2. VH domains that bind outside of the ACE2 binding site were not identified with this selection campaign.[60]

Here, we utilized an in-house Fab-phage library to identify unbiased Fab binders that recognize Spike-RBD. Briefly, for each round of selection, the Fab-phage pool was pre-cleared with biotinylated Fc immobilized on streptavidin (SA)-coated magnetic beads before incubating with SA-beads conjugated with biotinylated Spike-RBD-Fc (**Figure 3.1A**). After 3-4 rounds of selection, significant enrichment was observed for Fab-phage that bound Spike-RBD-Fc over Fc alone. Individual phage clones were isolated and phage ELISA was used to characterize binding to Spike-RBD-Fc alone and in complex with ACE2-Fc. We hypothesized that Fab-phage that can bind similarly to Spike-RBD-Fc alone or when masked with ACE2-Fc would bind an epitope outside of the ACE2 binding site and would therefore occupy a unique epitope from the VH. From here, we identified over 200 unique Fab-phage sequences that bound Spike-RBD-Fc, a majority of which did not bind at the Spike-ACE2 interface (**Figure 3.1B**). We characterized a subset of these and identified two lead Fabs, C01 and D01, which bound Spike-RBD-Fc and the trimeric Spike full ectodomain (S_{ecto}) with high affinity (**Figure 3.1C-D, Table 3.1**). Conversion of these Fabs into a traditional bi-valent IgG scaffold further improved affinity to S_{ecto} to single-digit nanomolar K_D (**Figure 3.1F-G**). The increased affinity of the IgG compared to the Fab is driven by the avidity of the two binding arms. Due to the challenges of modeling the interaction between a bi-valent binder and a conformationally dynamic, trimeric Spike, we have reported affinities as apparent K_Ds ($K_{D,app}$) derived from a 1:1 binding model of the data.

We proceeded to characterize the epitopes of Fab C01 and Fab D01 by sequential bio-layer interferometry (BLI), where one binder is incubated with the antigen until saturation, followed by incubation with the second binder. Robust binding of the second binder in the presence of the first

suggests that the two binders occupy non-overlapping epitopes on the same antigen. Both Fab C01 and Fab D01 do not overlap with ACE2-Fc, indicating that they bind outside of the ACE2 binding site (**Figure 3.1E**). Interestingly, while Fab C01 and D01 compete for binding on Spike-RBD, on S_{ecto} their epitopes appear to not overlap (**Figure 3.2A**). Additionally, we observe that pre-saturation with Fab D01 blocks binding of Fab C01 on S_{ecto}, while pre-saturation with Fab C01 does not block Fab D01 (**Figure 3.2B-C**). These data suggest that although C01 and D01 have overlapping epitopes on isolated Spike-RBD, these Fabs have different binding mechanisms and could be influenced by the dynamics and accessibility of the RBDs in the context of the Spike trimer. Therefore, we assign site C (for Fab C01) and site D (for Fab D01) to unique epitopes on S_{ecto} though they overlap on Spike-RBD. Additionally, we compared the epitopes of Fab C01 and Fab D01 to a previously described antibody CR3022,[64] and found that Fab D01 competes with CR3022 while Fab C01 does not (**Figure 3.2D**). CR3022 has been shown to recognize the RBD outside of the ACE2 binding site at an epitope only accessible when the RBD is in the "up" conformation.[64] Fab D01 appears to bind an overlapping epitope, but with higher affinity to Spike-RBD-Fc compared to CR3022 (K_D = 115 nM). Thus, from these studies, we have identified binders against 4 unique epitopes on Spike-RBD: site A (VH A01), site B (VH B01), site C (Fab C01), and site D (Fab D01).

Generation of bi-specific knob-in-hole IgGs using Fab and VH against SARS-CoV-2 Spike

We wondered whether combining VH and Fab binders directed at different Spike epitopes into a bi-specific antibody scaffold could improve potency. One of the most straightforward and successful methods to make bi-specific IgG-type binders is the classic Knob-In-Hole (KIH) strategy, pioneered by Paul Carter's Group at Genentech.[86] In this approach, a complementary set

of mutations in the CH3 domains of the Fc promotes the heterodimerization between a "knob" Fc and a "hole" Fc. A KIH bi-specific IgG modality has not been reported for COVID-19 to date but has been previously developed for other viral infections such as HIV and showed improved potency compared to the mono-specific parental binders.[87] Therefore, generating KIH bi-specifics against Spike could present a novel, effective modality against SARS-CoV-2.

When the KIH strategy is applied for two Fab arms, the individual half IgGs must be separately expressed and purified before they can be assembled into a bi-specific IgG molecule due to the presence of two different light chains. This process is required to circumvent the problem of light chains and heavy chain mispairing that can occur when the antibodies are co-expressed in the same cell. While many strategies have been developed to try and address this issue, including using common light chains, additional purifications, or scaffold engineering, they all require additional labor-intensive steps.[88–90] However, since the VH/Fab bi-specific molecules contain only one light chain in the Fab arm, co-expression of the VH-Fc knob with Fab-Fc hole should generate the proper VH/Fab bi-specific IgG (**Figure 3.3A**).

Using this strategy, we generated 4 different VH/Fab bi-specifics to explore combinations of targeting sites A and B with sites C and D; Bis1 is VH(A01)/Fab(C01) fusion, Bis2 is VH(B01)/Fab(C01), Bis3 is VH(A01)/Fab(D01), and Bis4 is VH(B01)/Fab(D01). For each bi-specific, the VH was cloned into the "knob" Fc, and the heavy chain of the Fab was cloned into the "hole" Fc. All four bi-specific IgGs were successfully expressed and purified and shown by gel to be bi-specific, containing both a VH-Fc and Fab-Fc arm on each molecule (**Figure 3.4**). All 4 bi-specifics bound S_{ecto} with higher affinity than their parental mono-specific counterparts (**Figure 3.3B-E, Table 3.1**). In particular, Bis3 and Bis4, which both utilize Fab(D01), bound S_{ecto} with highest affinity with $K_{D,app}$ of 395 pM and 127 pM, respectively. Reversing the orientation

and immobilizing the bi-specific IgG on the biosensor and probing with soluble S_{ecto} did not significantly change the measured affinity (**Figure 3.5**).

Bi-specific Knob-In-Hole IgGs show enhanced neutralization against pseudotyped and authentic SARS-CoV-2 compared to mono-specific binders

We then tested the neutralization potency of these VH/Fab bi-specifics using HIV-1-derived lentivirus pseudotyped with SARS-CoV-2 Spike to compare their potencies to the mono-specific bi-valent VH-Fc and IgGs. Spike pseudotypes were generated and used in neutralization assays with HEK293T cells expressing ACE2 on the surface using established vectors and protocols.[91] VH-Fc A01 and VH-Fc B01 neutralized Spike pseudotypes with half-maximal inhibitory concentration (IC50) of 2.86 nM (0.23 μg/mL) and 2.01 nM (0.16 μg/mL), respectively. In contrast, we found that IgG C01 and IgG D01 did not neutralize pseudovirus at the concentrations tested (up to 100 nM). This is likely due to the fact that these two IgGs do not target the ACE2 binding site, and there are likely epitope and geometry-specific mechanisms that determine whether and to what extent non-blocking binders neutralize virus. Indeed, anti-Spike antibodies that do not compete with ACE2 binding, including CR3022, have been reported but with mixed and variable success in neutralizing SARS-CoV-2 depending on the specific antibody and its epitope.[64,67,92–95]

Next, we tested the neutralization profile of the bi-specific VH/Fab IgGs. To our surprise, we found that bi-specifics that utilize the non-neutralizing Fab D01 neutralized significantly more potently than the parental mono-specific binders. Bis3 and Bis4 neutralized with IC50s of 0.128 nM (0.015 μg/mL) and 0.107 nM (0.012 μg/mL), respectively, which is ~20-fold more potent than the VH-Fc alone (**Figure 3.6C-D, Table 3.2**). This indicates that a bi-specific antibody, even if

one of the arms is non-neutralizing, can show enhanced potency compared to the mono-specific counterparts. In contrast, the bi-specific antibodies that utilized Fab C01 (Bis1, Bis2) did not show such improved potency and neutralized with similar IC50s to the parental VH-Fc (**Figure 3.6A-B**). This suggests that the enhanced potency provided by a non-neutralizing binder is epitope-specific. Interestingly, we observe no significant correlation between IC50 and binding affinity against S_{ecto} of the bi-specifics and VH-Fcs ($R^2 = 0.06$) (**Figure 3.7**). This suggests that an increase in neutralization potency of anti-Spike binders is not highly predictive from affinity alone, and that the specific mechanism and geometry of epitopes targeted by the bi-specific IgG scaffold likely play an important role in increasing potency. Additionally, we find that a cocktail of the mono-specific antibodies (IgG + VH-Fc) does not improve potency (**Figure 3.8**), which suggests that a bi-specific IgG, where two epitopes are targeted by a single agent, has unique mechanisms and advantages.

Lastly, we examined the neutralization profile of the bi-specific IgGs and VH-Fc on authentic SARS-CoV-2 virus with Vero E6 cells as the host cell. Each binder was assayed for its ability to decrease the cytopathic effect (CPE) of Vero E6 cells caused by SARS-CoV-2 infection. Consistent with the pseudovirus neutralization results, bi-specific IgGs Bis3 and Bis4 neutralized authentic SARS-CoV-2 significantly more potently (~25-fold) than the VH-Fcs (**Figure 3.9, Table 3.3**). The IC50s of VH-Fc A01 and VH-Fc B01 against authentic SARS-CoV-2 were 25-30 nM. These values are similar to a previously reported IC50 of VH-Fc B01 of 33.5 nM, which used qPCR to read out intracellular viral RNA.[60] The neutralization IC50s of Bis3 and Bis4 against authentic SARS-CoV-2 were 1.00 nM (0.11 μg/mL) and 1.19 nM (0.14 μg/mL), respectively. Interestingly, Bis1 and Bis2, which did not show a significant improvement over the VH-Fcs in the pseudovirus neutralization assays, were about 2.5 to 3-fold more potent than the VH-Fcs when

assayed on authentic virus. Taken together, we find that bi-specific IgGs, particularly Bis3 and Bis4, are significantly more potent in neutralizing both pseudotyped and authentic SARS-CoV-2 virus than their mono-specific counterparts.

Structural modeling of the epitopes targeted by bi-specific IgG Bis4 (VH B01/Fab D01)

Bis4, which uses the combination of VH B01 and Fab D01 was one of the most potent molecules we tested in this study. The epitope of VH B01 was determined previously by cryo-EM.[60] In the absence of a high-resolution structure of Fab D01 bound to Spike, we utilized the structure of CR3022[64] as a surrogate to model how the two arms on Bis4 could engage Spike. We find that in the context of the same RBD, the VH and Fab bind at separate, non-overlapping epitopes (**Figure 3.10A-B**). The CR3022 epitope is fully exposed only in the RBD "up" conformation, while the VH B01 epitope is largely accessible regardless of the RBD conformation. VH B01 and Fab CR3022 point away from each other at an angle of 133 degrees, with a distance of 134.5 Å between the C-termini of the VH and heavy chain of the Fab. Although the exact epitope and angle of engagement of Fab D01 may differ from CR3022, it appears challenging for both arms of Bis4 to engage the same RBD. However, it could be possible for the Bis4 VH arm to bind one RBD, and the Fab arm to bind a neighboring RBD in the context of the Spike trimer when one or more RBDs are in the "up" conformation (**Figure 3.10C**). We hypothesize that simultaneous engagement of two RBDs on Spike by Bis4 could explain its potent neutralization mechanism, although there could be other unexplored mechanisms at play. Determining the exact epitope and binding mechanism of Fab D01 would shed further light into how these bi-specific IgGs engage Spike and neutralize SARS-CoV-2.

Discussion

Here, we report the generation of bi-specific IgG antibodies against SARS-CoV-2 Spike that combine neutralizing and non-neutralizing binders against different epitopes on the Spike-RBD as a promising protein engineering strategy to rapidly improve the potency of antibodies against COVID-19. We show that certain combinations of these binders into a bi-specific IgG scaffold are significantly more potent in neutralizing pseudotyped and authentic SARS-CoV-2 virus than the mono-specific bi-valent counterparts and may enable efficacy increases not predicted by affinity alone. Additionally, we show that non-blocking, non-neutralizing epitopes can provide an unexpected benefit and boost the potency of molecules when combined into a bi-specific format with neutralizing epitopes. Combing neutralizing and non-neutralizing epitopes can be a useful approach to rescue binders that would have been deprioritized due to their lack of neutralization. Exploring the use of this strategy in parallel with other affinity maturation campaigns on some of the most potent antibodies reported against SARS-CoV-2 to date could enable the generation of even more potent neutralizing binders. This can decrease the effective dose necessary for therapeutic effect, thus lessen the burden on manufacturing capacity and enable the wider distribution of these treatments.

In aggregate, we have produced binders against 4 distinct epitopes within the RBD of Spike. This is somewhat remarkable given the small size of the RBD (206 amino acids, ~23 kDa). Binders to many epitopes on Spike have been reported,[67,71,92,94–96] showing that this antigen is highly immunogenic both *in vivo* and *in vitro*. It will be interesting to map them relative to those we have found. Our results show that combinations via a KIH bi-specific scaffold is particularly useful to improve potency through avidity and multi-epitope targeting and could be less labor and time intensive than affinity maturation.

Our study also highlights how different epitopes on Spike differ in their neutralization potency and their engineering potential. To what extent an antibody neutralizes SARS-CoV-2 is likely influenced by its binding mechanism, affinity, and scaffold, and is made more complex by the oligomeric and dynamic nature of the target antigen Spike. It is well established that the RBDs of Spike proteins of the coronavirus family are capable of adopting various conformations and that the trimer can undergo large conformational changes.[97] These structural dynamics likely affect the accessibility and orientation of the different binding epitopes, which can then influence the potency of binders and how they behave when engineered into multi-specific modalities. This may help explain why bi-specifics that use Fab D01 are superior to bi-specifics that use Fab C01. Additionally, even binders that overlap in epitope, such as Fab D01 and CR3022, may differ in their properties. Fab D01 has much higher affinity to Spike than CR3022 and was non-neutralizing. CR3022 was also non-neutralizing (IC50 >> 400 μg/mL),[64] although another recent study contradicts this observation[93], and showed that CR3022 can neutralize SARS-CoV-2, possibly through the destabilization of the Spike trimer. Which combinations of binders will synergize and what antibody scaffolds are optimal for efficacy remain unclear, and provides a wide latitude for protein engineer to explore how these different factors affect antibody potency. A deeper biophysical understanding of Spike dynamics will also be important for rational engineering of potent biologics to this therapeutically important target. We believe these principles for design of bi-specific and bi-paratopic binders combining neutralizing and non-neutralizing binders can apply to other therapeutic targets even in the absence of high-resolution structures.

Methods

Cloning

Spike-RBD-Fc and trimeric Spike ectodomain (S_{ecto}), and ACE2-Fc were produced as biotinylated proteins as previously described.[98] Fabs were subcloned from the Fab-phagemid into an *E. coli* expression vector pBL347. VH-Fc were cloned into a pFUSE (InvivoGen) vector with a human IgG1 Fc domain as previously described.[60] The heavy chain of the IgG were cloned from the Fab plasmid into a pFUSE (InvivoGen) vector with a human IgG1 Fc domain. The light chain of the IgG was cloned from the Fab plasmid into the same vector but lacking the Fc domain. All constructs were sequence verified by Sanger sequencing.

Protein Expression and Purification

Fabs were expressed in *E. coli* C43(DE3) Pro + using an optimized autoinduction media and purified by protein A affinity chromatography.[45] VH-Fc, IgGs, and bi-specifics were expressed in Expi293 BirA cells using transient transfection (Expifectamine, Thermo Fisher Scientific). 3-5 days after transfection, media was harvested, and VH-Fc and IgGs were purified using protein A affinity chromatography. Bi-specific antibodies were purified by Ni-NTA affinity chromatography. The bi-specifics were then buffer exchanged into PBS containing 20% glycerol, concentrated, and flash frozen for storage. All other proteins were buffer exchanged into PBS by spin concentration and stored in aliquots at -80ºC. Purity and integrity of all proteins were assessed by SDS-PAGE.

Fab-phage selection

Phage selections were done according to previously established protocols.[45] Selections were performed using biotinylated antigens captured with streptavidin-coated magnetic beads (Promega). In each round, the phage pool was first cleared by incubation with beads loaded with Fc domain only. The unbound phage were then incubated with beads loaded with Spike-RBD-Fc. After washing, the bound phage was eluted by the addition of 2 μg/mL of TEV protease. In total, four rounds of selection were performed with decreasing amounts of Spike-RBD-Fc. All steps were done in PBS buffer + 0.02% Tween-20 + 0.2% BSA (PBSTB). Individual phage clones from the third and fourth round of selections were analyzed by phage ELISA.

Phage ELISA

For each phage clone, 4 different conditions were tested—Direct: Spike-RBD-Fc, Competition: Spike-RBD-Fc with equal concentration of Spike-RBD-Fc in solution, Negative selection: ACE2-Fc/Spike-RBD-Fc complex, and Control: Fc. 384-well Nunc Maxisorp flat-bottom clear plates (Thermo Fisher Scientific) were coated with 0.5 μg/mL of NeutrAvidin in PBS overnight at 4ºC and subsequently blocked with PBS + 0.02% Tween-20 + 2% BSA for 1 hr at room temperature. Plates were washed 3X with PBS containing 0.05% Tween-20 (PBST) and were washed similarly between each of the steps. 20 nM of biotinylated Spike-RBD-Fc, ACE2-Fc/Spike-RBD-Fc complex, or Fc diluted in PBSTB was captured on the NeutrAvidin-coated wells for 30 min, then blocked with PBSTB + 10 μM biotin for 30 min. Phage supernatant diluted 1:5 in PBSTB were added for 20 min. For the competition samples, the phage supernatant was diluted into PBSTB with 20 nM Spike-RBD-Fc. Bound phage were detected by incubation with anti-M13-HRP conjugate (Sino Biologics, 1:5000) for 30 min, followed by addition of TMB substrate (VWR

International). The reaction was quenched with addition of 1 M phosphoric acid and the absorbance at 450 nm was measured using a Tecan M200 Pro spectrophotometer.

Bio-layer Interferometry

Bio-layer interferometry data (BLI) were measured using an Octet RED384 (ForteBio) instrument. Spike-RBD-Fc or S_{ecto} were immobilized on a streptavidin (SA) biosensor and loaded until 0.4 nm signal was achieved. After blocking with 10 μM biotin, purified binders in solution was used as the analyte. PBSTB was used for all buffers. Data were analyzed using the ForteBio Octet analysis software and kinetic parameters were determined using a 1:1 monovalent binding model.

Pseudovirus generation

HEK293T-ACE2 cells were a gift from Arun Wiita's laboratory at the University of California, San Francisco. Cells were cultured in D10 media (DMEM + 1% Pen/Strep + 10% heat-inactivated FBS). Plasmids to generate pseudotyped HIV-1-derived lentivirus were a gift from Peter Kim's lab at Stanford University and pseudovirus displaying SARS-CoV-2 Spike was prepared as previously described.[91] Briefly, plasmids at the designated concentrations were added to OptiMEM media with FuGENE HD Transfection Reagent (Promega) at a 3:1 FuGENE:DNA ratio, incubated for 30 minutes, and subsequently transfected into HEK-293T cells. After 24 hrs, the supernatant was removed and replaced with D10 culture media. Virus was propagated for an additional 48 hrs, and the supernatant was harvested and filtered. Virus was stored in flash-frozen aliquots at -80ºC and thawed prior to use.

HEK-ACE2 were seeded at 10,000 cells/well on 96-well white plates (Corning, cat. 354620). After 24 hrs, pseudovirus stocks were titered via a two-fold dilution series in D10 media and 40 µL were added to cells. After 60 hrs, infection and intracellular luciferase signal was determined using Bright-Glo™ Luciferase Assay (Promega), and the dilution achieving maximal luminescent signal within the linear range, ~3-5 x 10^5 luminescence units, was chosen as the working concentration for neutralization assays.

Pseudovirus neutralization assay

HEK-ACE2 were seeded at 10,000 cells/well in 40 µL of D10 on 96-well white plates (Corning, cat. 354620) 24 hrs prior to infection. To determine IC_{50} for pseudovirus neutralization, dose series of each VH binder were prepared at 3x concentration in D10 media and 50 µL were aliquoted into each well in 96-well plate format. Next, 50 µL of virus were added to each well, except no virus control wells, and the virus and blocker solution was allowed to incubate for 1 hr at 37ºC. Subsequent to pre-incubation, 80 µL of the virus and blocker inoculum were transferred to HEK-ACE2. After 60 hrs of infection at 37ºC, intracellular luciferase signal was measured using the Bright-Glo™ Luciferase Assay. Luminescence was normalized to the no binder control and plotted using Prism 8 software. A non-linear 4-parameter regression was used to determine the IC50.

Authentic SARS-CoV-2 virus neutralization assay

Handling of authentic SARS-CoV-2 virus and neutralization assays were conducted using biosafety level 3 containment with approved protocols. SARS-CoV-2 isolate USA-WA1/2020 (NR-52281) was obtained from BEI resources[99] and expanded with minimal passage in Vero E6 cells. SARS-CoV-2 at 10^3 $TCID_{50}$/ml was incubated with 3-fold serially diluted binder at 37°C for

1 hr prior to infection of Vero E6 cell monolayer in 96-well-plates. Virus/binder mixtures were added to 10 replicate wells at 100 μL per well. The plates were incubated for 7 days at 37°C with 5% CO_2 until clear cytopathic effect (CPE) developed. The experiment was repeated twice. Wells with clear CPE were counted positive and percentage of positive wells for each concentration of binder were plotted and analyzed using Prism 8 software. A non-linear 4-parameter regression was used to determine the IC50.

Figures and Tables

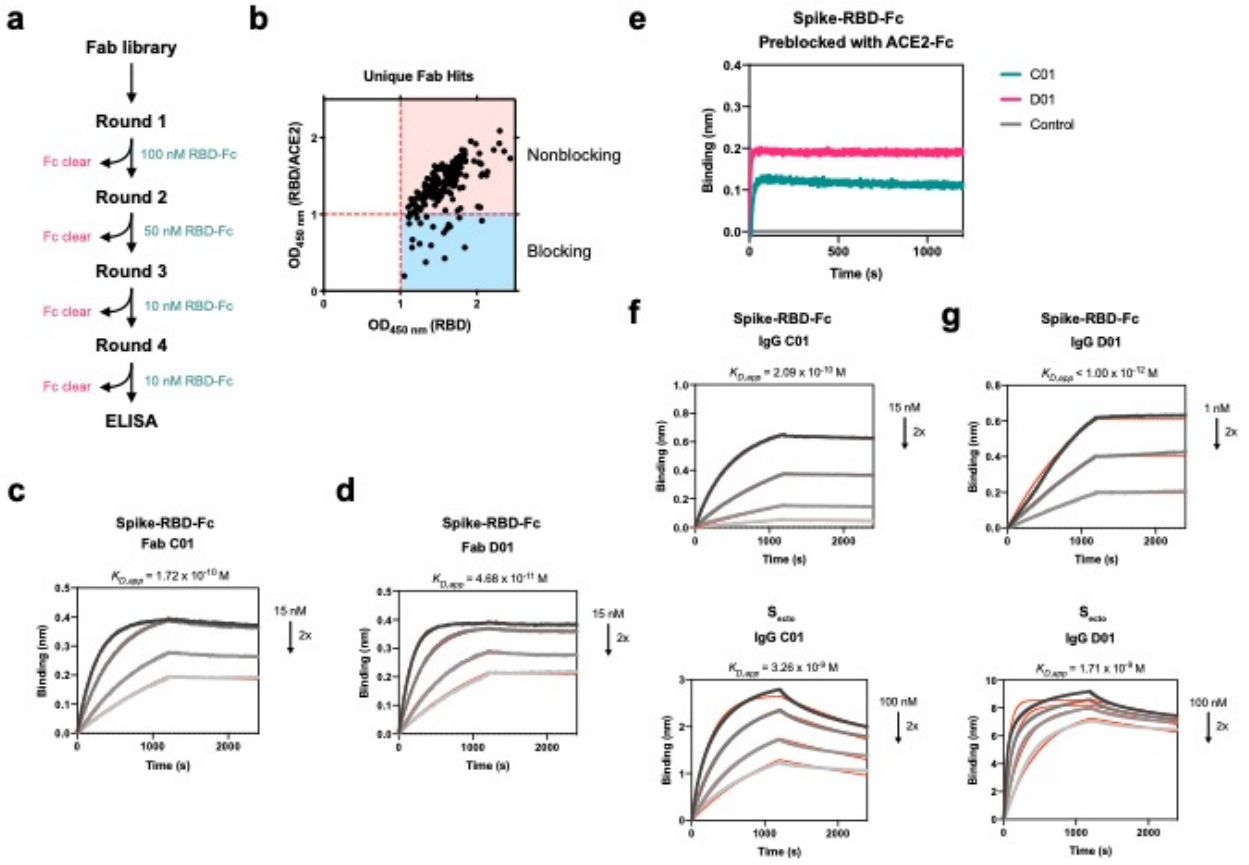

Figure 3.1: Fabs identified by phage display bind Spike RBD and S_{ecto} with high affinity outside of the ACE2 binding site.

a, Schematic of phage display used to isolate binders to Spike RBD-Fc from an in-house Fab-phage library. **b**, Phage ELISA used to characterize binders shows that a majority of binders isolated did not bind similarly to Spike RBD in complex with ACE2 as to RBD alone. Multipoint BLI measurements of **c**, Fab C01 and **d**, Fab D01 on Spike RBD-Fc demonstrate high affinity binding. **e**, Sequential epitope binning BLI demonstrates when Spike RBD-Fc is pre-saturated with ACE2-Fc, both Fabs C01 and D01 can still bind, indicating a non-overlapping epitope with ACE2-Fc. Multipoint BLI measurements of **f**, IgG C01 and **g**, IgG D01 show that conversion of Fab to IgG increases affinity to both Spike RBD-Fc (top) and trimeric S_{ecto} (bottom).

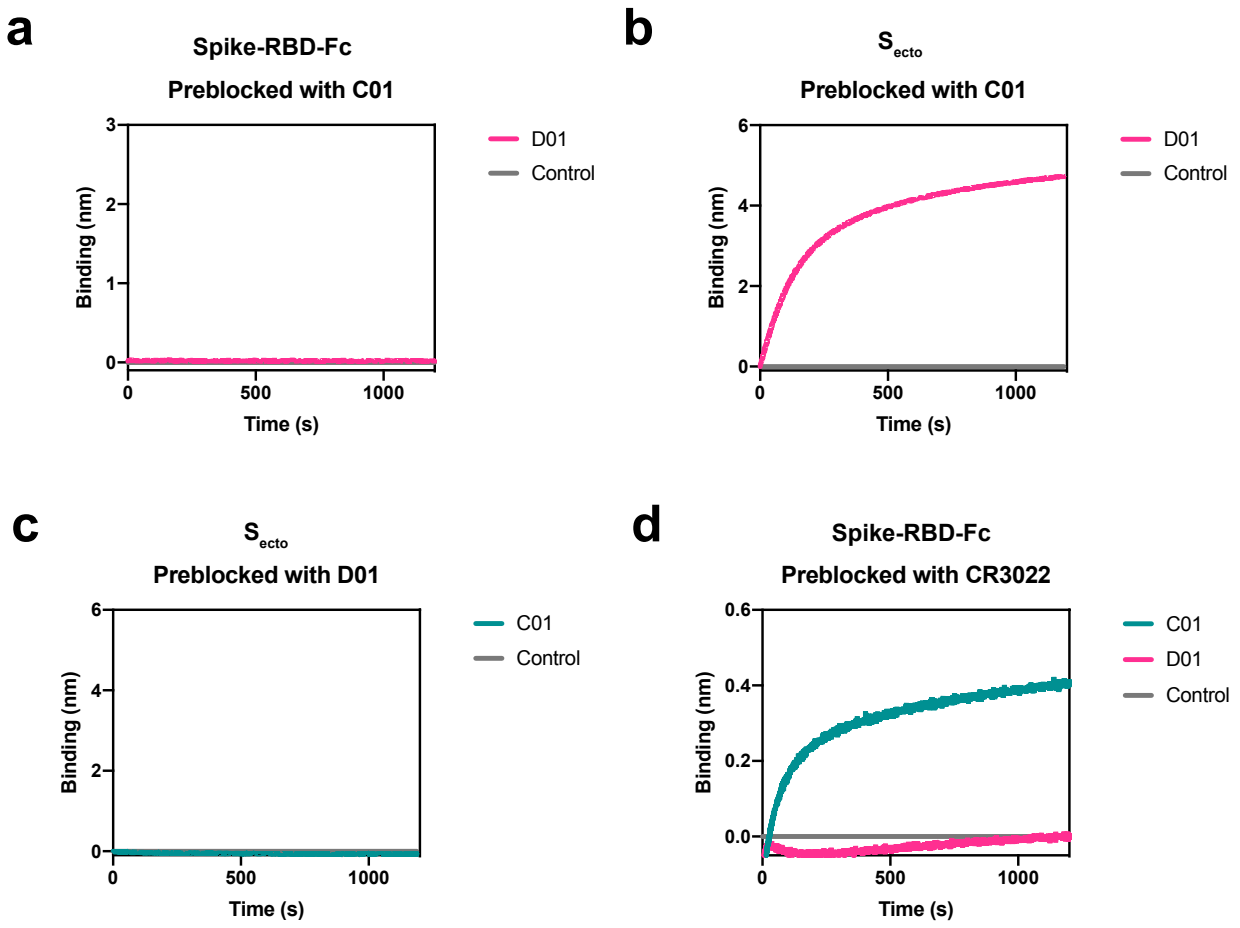

Figure 3.2: Sequential epitope binning of lead Fabs reveal unique epitopes on S_{ecto}.
Sequential BLI epitope binning was performed in which antigen was pre-saturated with the first binder and then exposed to the second binder. **a**, Fab C01 and Fab D01 overlap in epitope on Spike-RBD-Fc. **b**, On S_{ecto}, Fab D01 is able to bind after preblocking with Fab C01. **c**, In contrast, Fab C01 is not able to bind S_{ecto} that is preblocked with Fab C01. **d**, Fab D01, but not Fab C01, shares an overlapping epitope with CR3022 when Spike-RBD-Fc is pre-saturated with CR3022.

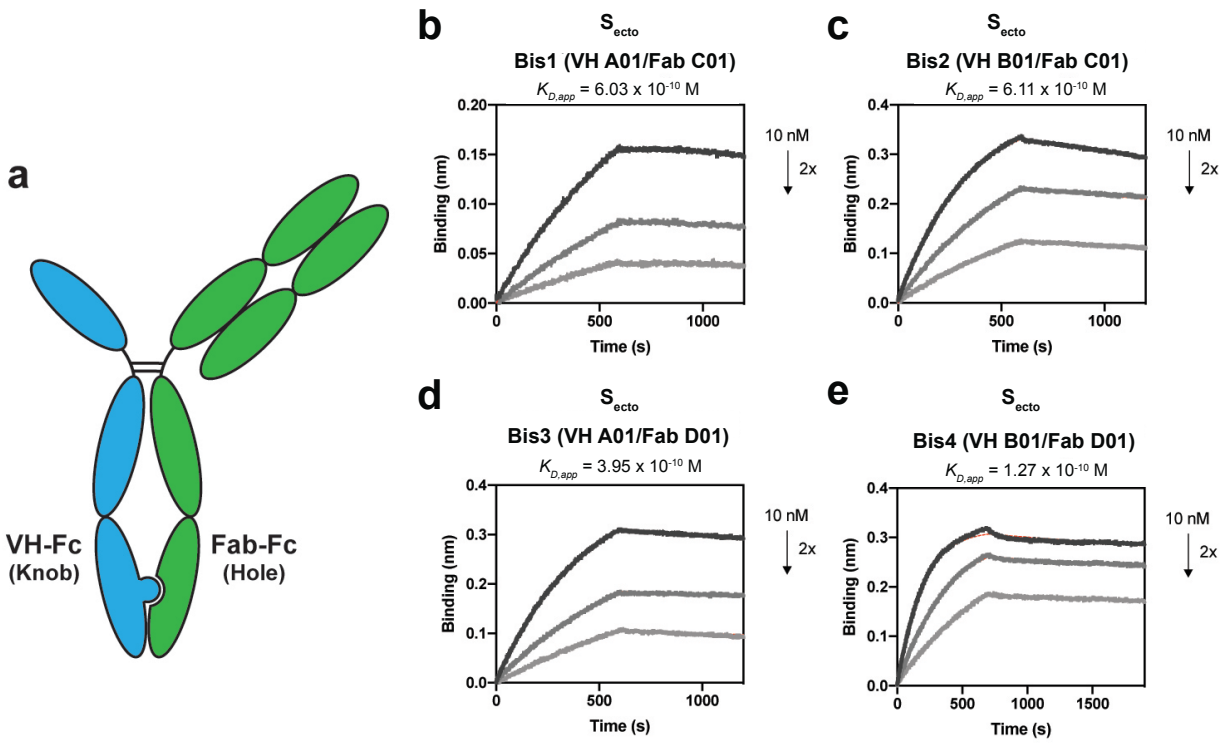

Figure 3.3: Bi-specific VH/Fab IgGs bind with high affinity to trimeric S_{ecto}.
a, Cartoon schematic of the bi-specific VH/Fab IgG antibody scaffold utilized in this study. **b-e,** Multipoint BLI measurements (10 nM, 5 nM, and 2.5 nM) of the indicated bi-specific antibody on S_{ecto}. **b,** Bis1 (VH A01/ FabC01) **c,** Bis2 (VH B01/FabC01) **d,** Bis3 (VH A01/ FabD01) **e,** Bis4 (VH B01/FabD01).

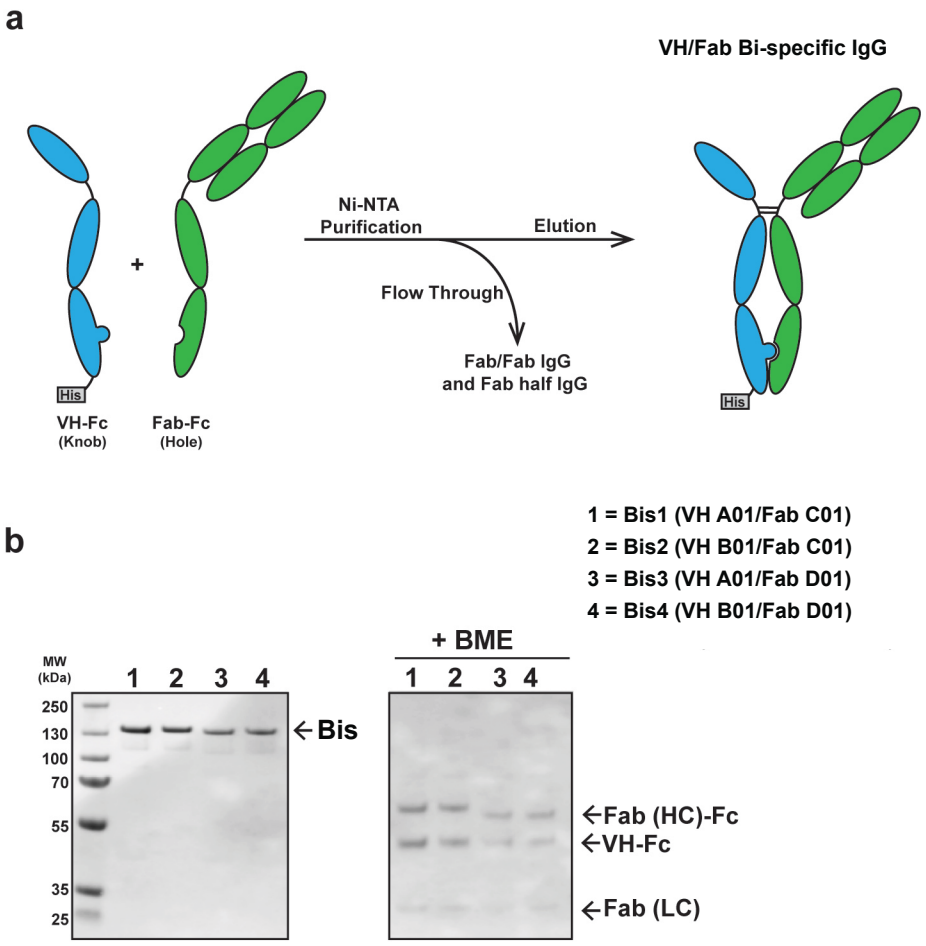

Figure 3.4: Purification of VH/Fab bi-specific IgGs.
a, Cartoon schematic of the process by which the bi-specific antibodies are purified. **b,** SDS-PAGE gel of the indicated purified bi-specific antibodies. (BME = 2-mercaptoethanol)

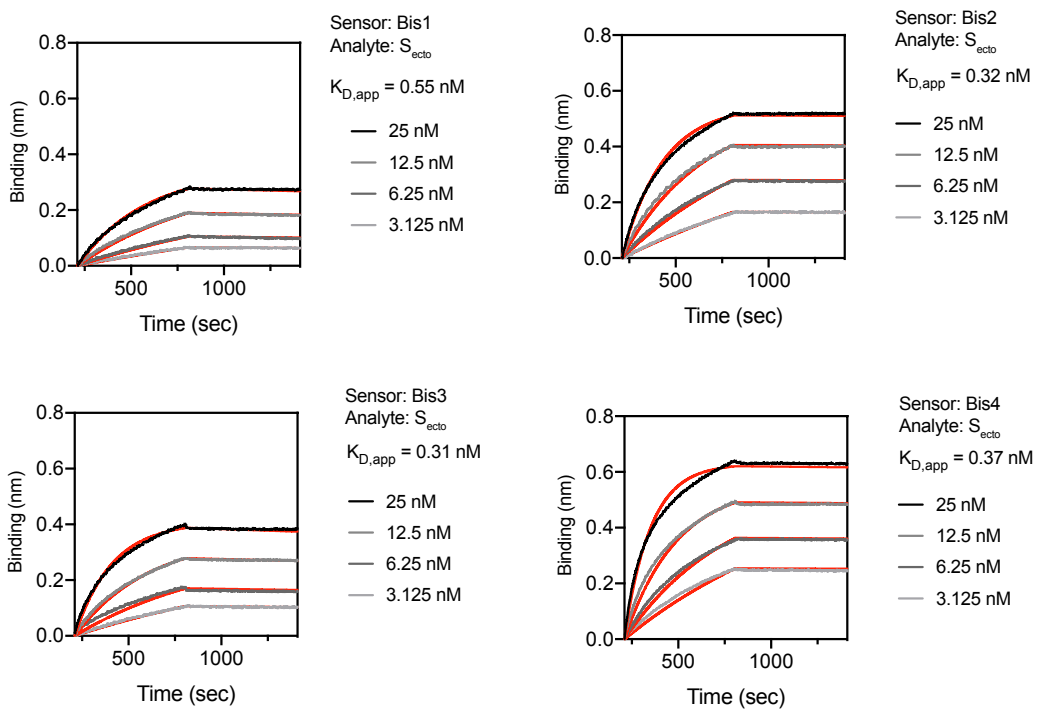

Figure 3.5: Binding of S_{ecto} to immobilized bi-specific VH/Fab IgGs.
Bi-specific VH/Fab IgGs (Bis1, Bis2, Bis3, Bis4) were immobilized on an anti-human Fc capture (AHC) biosensor and probed with soluble S_{ecto} at varying concentrations. Data were fit to a 1:1 binding interaction and $K_{D,app}$ are reported.

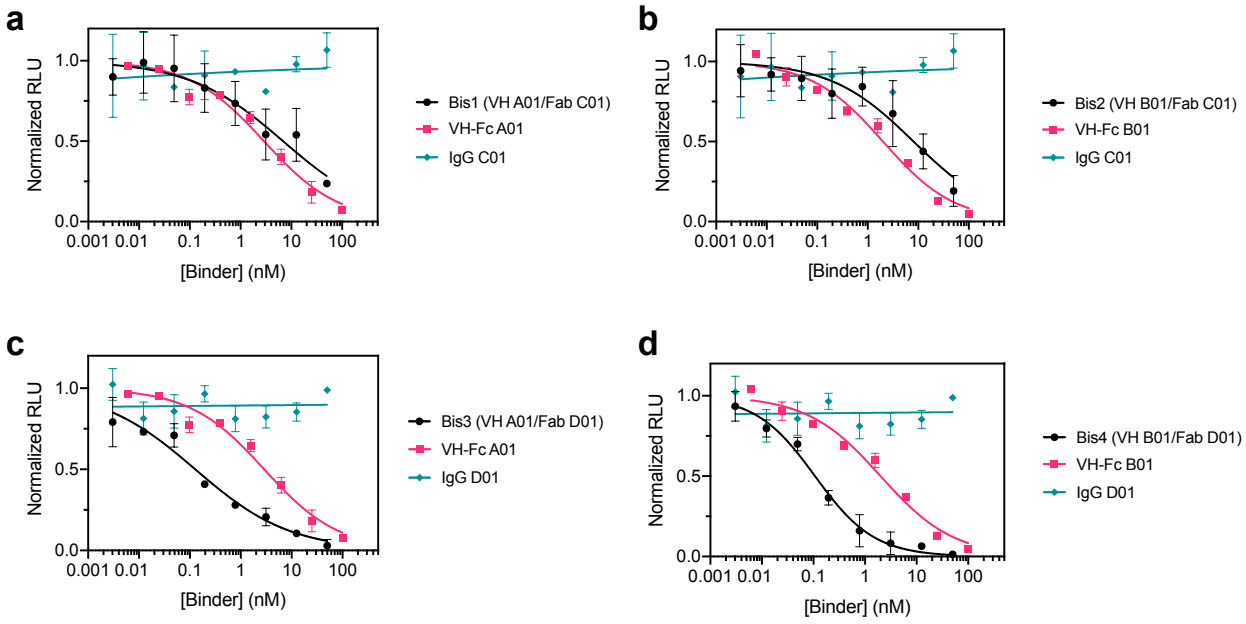

Figure 3.6: Bi-specific VH/Fab IgGs are more potent in neutralizing SARS-CoV-2 pseudovirus than the mono-specific counterparts.
Pseudovirus neutralization curves for **a,** Bis1 (VH A01/Fab C01) compared to VH-Fc A01 and IgG C01, **b,** Bis2 (VH B01/Fab C01) compared to VH-Fc B01 and IgG C01, **c,** Bis3 (VH A01/Fab D01) compared to VH-Fc A01 and IgG D01, **d,** Bis4 (VH B01/Fab D01) compared to VH-Fc A01 and IgG D01. Data represent average and standard deviation of three independent experiments and were fit to a non-linear regression using Prism 8 software to obtain IC50 values.

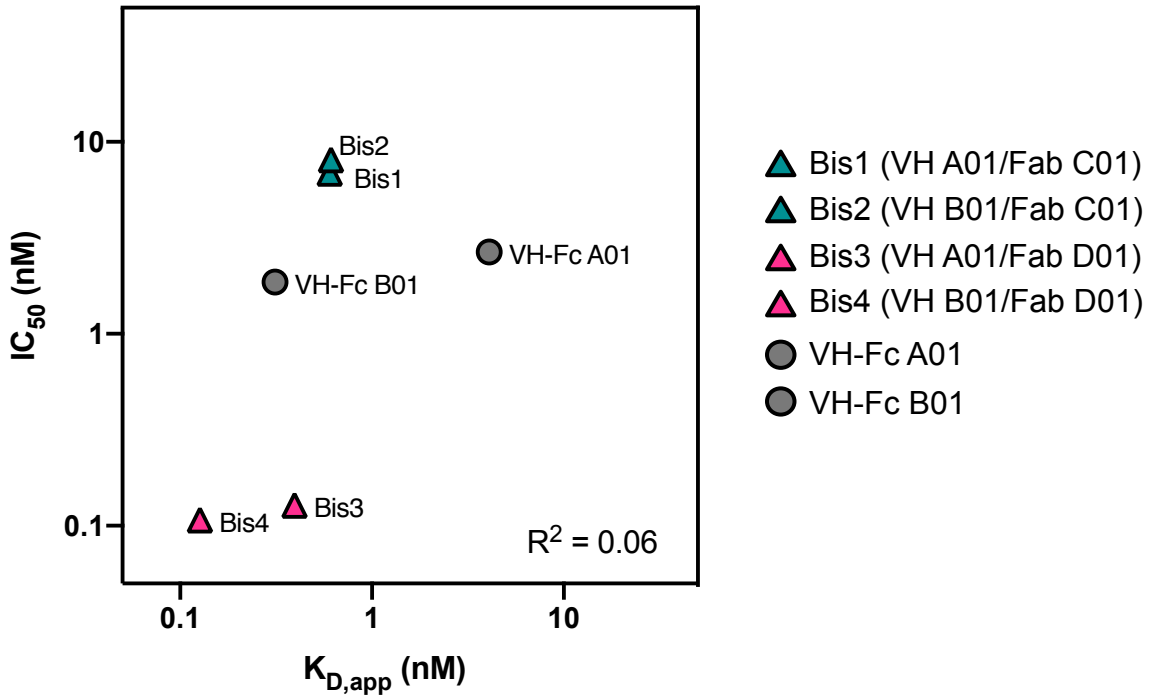

Figure 3.7: Binding affinity ($K_{D,app}$) and neutralization IC50 do not correlate for bi-specifics and VH-Fcs.
Correlation of *in vitro* binding affinity ($K_{D,app}$) against S_{ecto} and pseudotyped virus neutralization IC50 was determined by fitting data to a log-log linear extrapolation using Prism software. Bi-specifics utilizing Fab C01 are in teal triangles, bi-specifics utilizing Fab D01 are in pink triangles, and VH-Fcs are in grey circles.

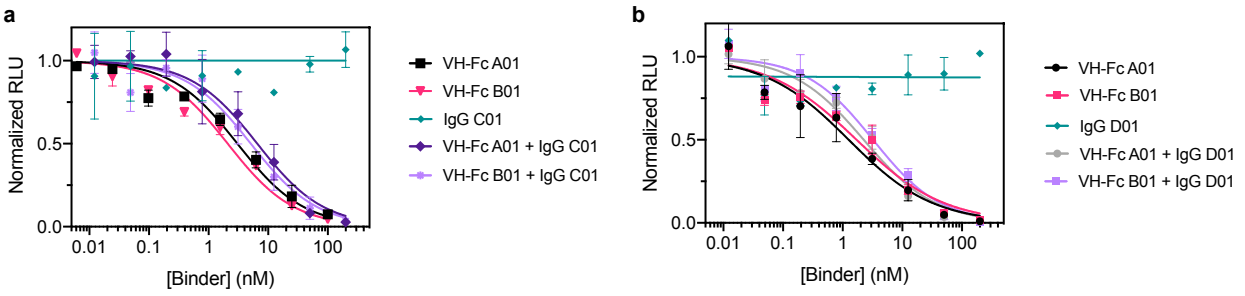

Figure 3.8: Cocktails of VH-Fc and IgGs do not show synergy in pseudotyped virus neutralization assays.
Pseudotyped neutralization curves of VH-Fc A01 or B01 in combination with **a**, IgG C01 or **b**, IgG D01 do not show enhanced neutralization activity compared to the VH-Fc alone. Data represent average and standard deviation of three separate experiments and were fit to a non-linear, 4-parameter sigmoidal function using Prism 8 software to obtain IC50 values.

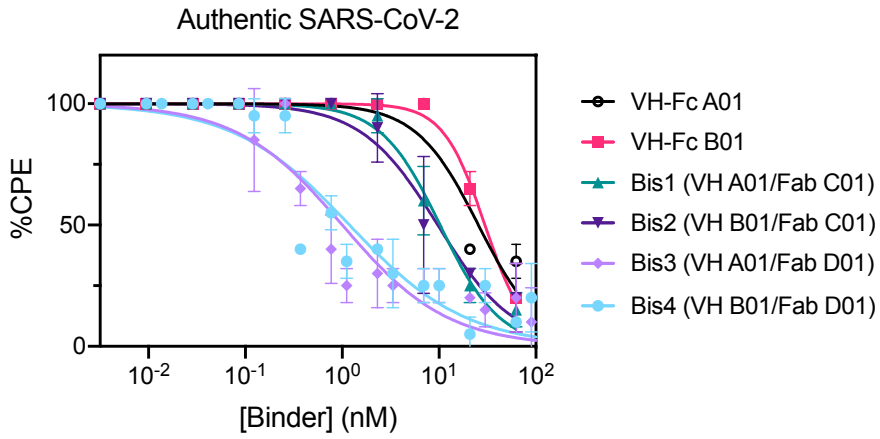

Figure 3.9: Bi-specific VH/Fab IgGs neutralize authentic SARS-CoV-2 virus more potently than the mono-specific VH-Fcs.
Authentic SARS-CoV-2 virus neutralization curves of VH-Fc A01, VH-Fc B01, Bis1 (VH A01/Fab C01), Bis2 (VH B01/Fab C01), Bis3 (VH A01/Fab D01), Bis4 (VH B01/Fab D01). Vero E6 cells were incubated with virus and 3-fold dilution of binder and assessed for cytopathic effect (CPE) 7 days after infection. Data represent average and standard deviation of two independent experiments. Data were fit to a non-linear regression using Prism 8 software to obtain IC50 values.

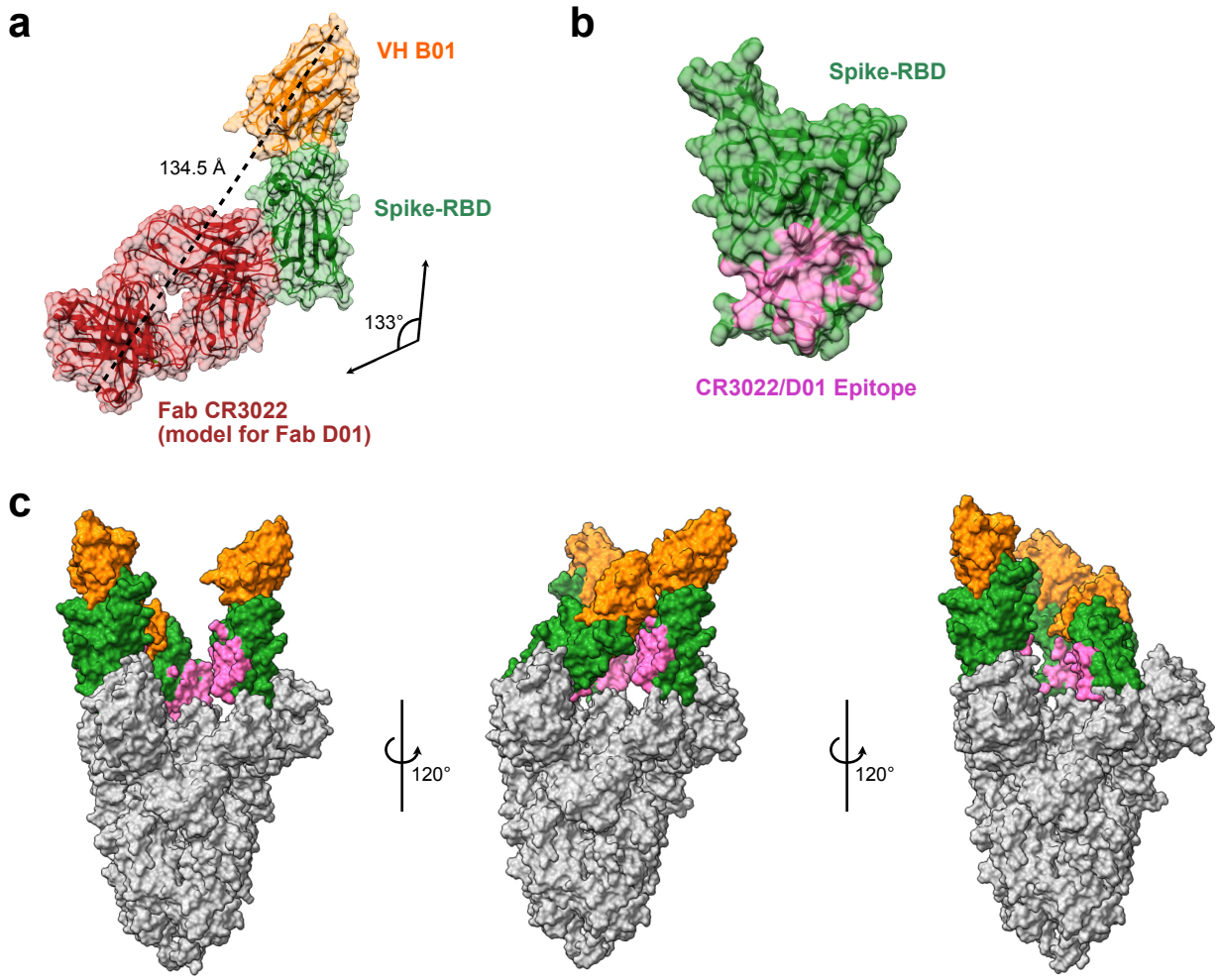

Figure 3.10: Structure modeling of Bis4 (VH B01/Fab D01) on Spike.
a, Structure model of how the two arms of Bis4 (VH B01/Fab D01) could interact with Spike-RBD. Since Fab CR3022 overlaps in epitope as Fab D01, the crystal structure of CR3022 bound to SARS-CoV-2 Spike-RBD (PDB: 6WGI) was used as a surrogate in conjunction with the cryo-EM structure of a trivalent form of VH B01 bound to SARS-CoV-2 Spike (PDB: 7JWB). Dashed line denotes distance between C-termini of VH B01 and heavy chain of Fab CR3022 to approximate the distance between the two arms of the bi-specific IgG. **b**, Surface model of Spike-RBD (PDB: 6WGI) showing the binding interface of CR3022/D01 in pink. **c**, Cryo-EM structure of trivalent VH B01 (orange) bound to SARS-CoV-2 Spike receptor binding domain (green) (PDB: 7JWB) with the CR3022/Fab D01 epitope (pink) shown. The CR3022/Fab D01 epitope may be accessible for simultaneous engagement of the two arms of the bi-specific IgG Bis4 when more than one RBDs on Spike is in the "up" conformation.

Table 3.1: *In vitro* binding affinities of antibodies against SARS-CoV-2 Spike.

	$K_{D,app}$ (nM)	
Antibody	Spike-RBD-Fc	S_{ecto}
Fab C01	0.172	29.9
Fab D01	0.047	92.0
IgG C01	0.209	3.26
IgG D01	<0.001[a]	1.71
VH-Fc A01	<0.001[a]	4.09
VH-Fc B01	0.056	0.313
Bis1 (VH A01/Fab C01)	<0.001[a]	0.603
Bis2 (VH B01/Fab C01)	<0.001[a]	0.611
Bis3 (VH A01/Fab D01)	<0.001[a]	0.395
Bis4 (VH B01/Fab D01)	<0.001[a]	0.127

[a] k_{off} was below the limit of detection (<1 x 10^{-7} sec^{-1}) and could not be fit.

Table 3.2: SARS-CoV-2 Pseudovirus Neutralization IC50.

	IC50	
Antibody	nM (95% CI)	μg/mL (95% CI)
VH-Fc A01	2.86 (1.63 – 5.03)	0.23 (0.13 – 0.40)
VH-Fc B01	2.01 (1.22 – 3.34)	0.16 (0.10 – 0.27)
IgG C01	>>100	>>15
IgG D01	>>100	>>15
VH-Fc A01 + IgG C01	6.63 (4.57 – 9.58)	0.75 (0.52 – 1.09)
VH-Fc B01 + IgG C01	5.13 (3.48– 7.57)	0.58 (0.39 – 0.86)
VH-Fc A01 + IgG D01	2.25 (1.66 – 3.04)	0.26 (0.19 – 0.35)
VH-Fc B01 + IgG D01	3.23 (2.34 – 4.42)	0.37 (0.27 – 0.50)
Bis1 (VH A01/Fab C01)	6.87 (3.41 – 17.07)	0.78 (0.39 – 1.94)
Bis2 (VH B01/Fab C01)	8.07 (4.63 – 16.00)	0.92 (0.53 – 1.82)
Bis3 (VH A01/Fab D01)	0.128 (0.080 – 0.201)	0.015 (0.009 – 0.023)
Bis4 (VH B01/Fab D01)	0.107 (0.080 – 0.143)	0.012 (0.009 – 0.016)

Table 3.3: Authentic SARS-CoV-2 Virus Neutralization IC50.

	IC50	
Antibody	nM (95% CI)	μg/mL (95% CI)
VH-Fc A01	25.5 (18.8 – 36.0)	2.04 (1.50 – 2.88)
VH-Fc B01	29.8 (26.5 – 33.5)	2.38 (2.12 – 2.68)
Bis1 (VH A01/Fab C01)	10.3 (8.5 – 12.4)	1.16 (0.95 – 1.40)
Bis2 (VH B01/Fab C01)	9.70 (6.80 – 14.2)	1.10 (0.77 – 1.61)
Bis3 (VH A01/Fab D01)	1.00 (0.67 – 1.54)	0.11 (0.08 – 0.17)
Bis4 (VH B01/Fab D01)	1.19 (0.80 – 1.80)	0.14 (0.09 – 0.20)

References

1. J. Bond, M. & M. Crews, C. Proteolysis targeting chimeras (PROTACs) come of age: entering the third decade of targeted protein degradation. *RSC Chem. Biol.* **2**, 725–742 (2021).
2. Uhlén, M. *et al.* Tissue-based map of the human proteome. *Science* **347**, (2015).
3. Cotton, A. D., Nguyen, D. P., Gramespacher, J. A., Seiple, I. B. & Wells, J. A. Development of Antibody-Based PROTACs for the Degradation of the Cell-Surface Immune Checkpoint Protein PD-L1. *J. Am. Chem. Soc.* **143**, 593–598 (2021).
4. Banik, S. M. *et al.* Lysosome-targeting chimaeras for degradation of extracellular proteins. *Nature* **584**, 291–297 (2020).
5. Caianiello, D. F. *et al.* Bifunctional small molecules that mediate the degradation of extracellular proteins. *Nat. Chem. Biol.* **17**, 947–953 (2021).
6. Zhou, Y., Teng, P., Montgomery, N. T., Li, X. & Tang, W. Development of Triantennary N-Acetylgalactosamine Conjugates as Degraders for Extracellular Proteins. *ACS Cent. Sci.* **7**, 499–506 (2021).
7. Pettersson, M. & Crews, C. M. PROteolysis TArgeting Chimeras (PROTACs) — Past, present and future. *Drug Discov. Today Technol.* **31**, 15–27 (2019).
8. Sakamoto, K. M. *et al.* Protacs: Chimeric molecules that target proteins to the Skp1–Cullin–F box complex for ubiquitination and degradation. *Proc. Natl. Acad. Sci.* **98**, 8554–8559 (2001).
9. Krönke, J. *et al.* Lenalidomide Causes Selective Degradation of IKZF1 and IKZF3 in Multiple Myeloma Cells. *Science* **343**, 301–305 (2014).
10. Mullard, A. First targeted protein degrader hits the clinic. *Nat. Rev. Drug Discov.* d41573-019-00043–6 (2019) doi:10.1038/d41573-019-00043-6.

11. Ahn, G. *et al.* LYTACs that engage the asialoglycoprotein receptor for targeted protein degradation. *Nat. Chem. Biol.* **17**, 937–946 (2021).
12. Janssens, R., Struyf, S. & Proost, P. The unique structural and functional features of CXCL12. *Cell. Mol. Immunol.* **15**, 299–311 (2018).
13. Freeman, G. J. *et al.* Engagement of the Pd-1 Immunoinhibitory Receptor by a Novel B7 Family Member Leads to Negative Regulation of Lymphocyte Activation. *J. Exp. Med.* **192**, 1027–1034 (2000).
14. Ridgway, J. B. B., Presta, L. G. & Carter, P. 'Knobs-into-holes' engineering of antibody C $_{H}$ 3 domains for heavy chain heterodimerization. *Protein Eng. Des. Sel.* **9**, 617–621 (1996).
15. Joshi, K. K. *et al.* Elucidating heavy/light chain pairing preferences to facilitate the assembly of bispecific IgG in single cells. *mAbs* **11**, 1254–1265 (2019).
16. Ovacik, A. M. *et al.* Single cell-produced and in vitro-assembled anti-FcRH5/CD3 T-cell dependent bispecific antibodies have similar in vitro and in vivo properties. *mAbs* **11**, 422–433 (2019).
17. Lim, S. A. *et al.* Bispecific VH/Fab antibodies targeting neutralizing and non-neutralizing Spike epitopes demonstrate enhanced potency against SARS-CoV-2. *mAbs* **13**, 1893426 (2021).
18. Wang, J. & Xu, B. Targeted therapeutic options and future perspectives for HER2-positive breast cancer. *Signal Transduct. Target. Ther.* **4**, 34 (2019).
19. Barretina, J. *et al.* The Cancer Cell Line Encyclopedia enables predictive modeling of anticancer drug sensitivity. *Nature* **483**, 603–607 (2012).
20. Sharma, S. V., Bell, D. W., Settleman, J. & Haber, D. A. Epidermal growth factor receptor mutations in lung cancer. *Nat. Rev. Cancer* **7**, 169–181 (2007).

21. Spano, J.-P. *et al.* Impact of EGFR expression on colorectal cancer patient prognosis and survival. *Ann. Oncol.* **16**, 102–108 (2005).
22. Arienti, C., Pignatta, S. & Tesei, A. Epidermal Growth Factor Receptor Family and its Role in Gastric Cancer. *Front. Oncol.* **9**, (2019).
23. Martinko, A. J. *et al.* Targeting RAS-driven human cancer cells with antibodies to upregulated and essential cell-surface proteins. *eLife* **7**, e31098 (2018).
24. Goldenberg, D. M., Stein, R. & Sharkey, R. M. The emergence of trophoblast cell-surface antigen 2 (TROP-2) as a novel cancer target. *Oncotarget* **9**, 28989–29006 (2018).
25. Hsu, E.-C. *et al.* Trop2 is a driver of metastatic prostate cancer with neuroendocrine phenotype via PARP1. *Proc. Natl. Acad. Sci.* **117**, 2032–2042 (2020).
26. Saad, E. B., Oroya, A. & Rudd, C. E. Abstract 6528: Anti-PD-1 induces the endocytosis of the co-receptor from the surface of T-cells: Nivolumab is more effective than Pembrolizumab. *Cancer Res.* **80**, 6528–6528 (2020).
27. Chatterjee, S., Azad, B. B. & Nimmagadda, S. The Intricate Role of CXCR4 in Cancer. *Adv. Cancer Res.* **124**, 31–82 (2014).
28. Stephens, B. S., Ngo, T., Kufareva, I. & Handel, T. M. Functional anatomy of the full-length CXCR4-CXCL12 complex systematically dissected by quantitative model-guided mutagenesis. *Sci. Signal.* **13**, (2020).
29. Liu, H. *et al.* Identification of a hotspot on PD-L1 for pH-dependent binding by monoclonal antibodies for tumor therapy. *Signal Transduct. Target. Ther.* **5**, 158 (2020).
30. Tan, S. *et al.* Distinct PD-L1 binding characteristics of therapeutic monoclonal antibody durvalumab. *Protein Cell* **9**, 135–139 (2018).

31. Fuentes, G., Scaltriti, M., Baselga, J. & Verma, C. S. Synergy between trastuzumab and pertuzumab for human epidermal growth factor 2 (Her2) from colocalization: an in silico based mechanism. *Breast Cancer Res. BCR* **13**, R54 (2011).
32. Cai, W.-Q. *et al.* The Latest Battles Between EGFR Monoclonal Antibodies and Resistant Tumor Cells. *Front. Oncol.* **10**, 1249 (2020).
33. Jefferis, R. Glycosylation as a strategy to improve antibody-based therapeutics. *Nat. Rev. Drug Discov.* **8**, 226–234 (2009).
34. Naumann, U. *et al.* CXCR7 Functions as a Scavenger for CXCL12 and CXCL11. *PLOS ONE* **5**, e9175 (2010).
35. Yamazaki, T. *et al.* Role of Grb2 in EGF-stimulated EGFR internalization. *J. Cell Sci.* **115**, 1791–1802 (2002).
36. Zheng, Y. *et al.* Temporal regulation of EGF signalling networks by the scaffold protein Shc1. *Nature* **499**, 166–171 (2013).
37. Ginestier, C. *et al.* ERBB2 phosphorylation and trastuzumab sensitivity of breast cancer cell lines. *Oncogene* **26**, 7163–7169 (2007).
38. Vieira, P. & Rajewsky, K. The half-lives of serum immunoglobulins in adult mice. *Eur. J. Immunol.* **18**, 313–316 (1988).
39. Attwood, M. M., Jonsson, J., Rask-Andersen, M. & Schiöth, H. B. Soluble ligands as drug targets. *Nat. Rev. Drug Discov.* **19**, 695–710 (2020).
40. Roth, T. L. *et al.* Reprogramming human T cell function and specificity with non-viral genome targeting. *Nature* **559**, 405–409 (2018).

41. Leung, K. K. *et al.* Multiomics of azacitidine-treated AML cells reveals variable and convergent targets that remodel the cell-surface proteome. *Proc. Natl. Acad. Sci.* **116**, 695–700 (2019).

42. Burslem, G. M. *et al.* The Advantages of Targeted Protein Degradation Over Inhibition: An RTK Case Study. *Cell Chem. Biol.* **25**, 67-77.e3 (2018).

43. Salami, J. *et al.* Androgen receptor degradation by the proteolysis-targeting chimera ARCC-4 outperforms enzalutamide in cellular models of prostate cancer drug resistance. *Commun. Biol.* **1**, 100 (2018).

44. Koo, B.-K. *et al.* Tumour suppressor RNF43 is a stem-cell E3 ligase that induces endocytosis of Wnt receptors. *Nature* **488**, 665–669 (2012).

45. Hornsby, M. *et al.* A High Through-put Platform for Recombinant Antibodies to Folded Proteins. *Mol. Cell. Proteomics* **14**, 2833–2847 (2015).

46. Vijayan, D., Young, A., Teng, M. W. L. & Smyth, M. J. Targeting immunosuppressive adenosine in cancer. *Nat. Rev. Cancer* **17**, 709–724 (2017).

47. Sek, K. *et al.* Targeting Adenosine Receptor Signaling in Cancer Immunotherapy. *Int. J. Mol. Sci.* **19**, 3837 (2018).

48. Chiang, M.-J. *et al.* An Fc Domain Protein–Small Molecule Conjugate as an Enhanced Immunomodulator. *J. Am. Chem. Soc.* **136**, 3370–3373 (2014).

49. Lebon, G., Edwards, P. C., Leslie, A. G. W. & Tate, C. G. Molecular Determinants of CGS21680 Binding to the Human Adenosine A2A Receptor. *Mol. Pharmacol.* **87**, 907–915 (2015).

50. Lin, S. *et al.* Redox-based reagents for chemoselective methionine bioconjugation. *Science* **355**, 597–602 (2017).

51. Elledge, S. K. *et al.* Systematic identification of engineered methionines and oxaziridines for efficient, stable, and site-specific antibody bioconjugation. *Proc. Natl. Acad. Sci.* **117**, 5733–5740 (2020).

52. Douglass, E. F., Miller, C. J., Sparer, G., Shapiro, H. & Spiegel, D. A. A Comprehensive Mathematical Model for Three-Body Binding Equilibria. *J. Am. Chem. Soc.* **135**, 6092–6099 (2013).

53. Grein, J. *et al.* Compassionate use of remdesivir for patients with severe Covid-19. *N. Engl. J. Med.* **382**, 2327–2336 (2020).

54. Joyner, M. J. *et al.* Effect of Convalescent Plasma on Mortality among Hospitalized Patients with COVID-19: Initial Three-2 Month Experience. *medRxiv* 2020.08.12.20169359 (2020) doi:10.1101/2020.08.12.20169359.

55. Chan, K. K. *et al.* Engineering human ACE2 to optimize binding to the spike protein of SARS coronavirus 2. *Science* **1265**, eabc0870 (2020).

56. Monteil, V. *et al.* Inhibition of SARS-CoV-2 infections in engineered human tissues using clinical-grade soluble human ACE2. *Cell* **181**, 905–913 (2020).

57. Glasgow, A. *et al.* Engineered ACE2 receptor traps potently neutralize SARS-CoV-2. *bioRxiv* (2020) doi:10.1101/2020.07.31.231746.

58. Guo, L. *et al.* Engineered Trimeric ACE2 Binds and Locks “Three-up” Spike Protein to Potently Inhibit SARS-CoVs and Mutants. *bioRxiv* (2020) doi:10.1101/2020.08.31.274704.

59. Robbiani, D. F. *et al.* Convergent antibody responses to SARS-CoV-2 in convalescent individuals. *Nature* **584**, 437–442 (2020).

60. Bracken, C. J. *et al.* Bi-paratopic and multivalent human VH domains neutralize SARS-CoV-2 by targeting distinct epitopes within the ACE2 binding interface of Spike. *bioRxiv* (2020) doi:10.1101/2020.08.08.242511.

61. Schoof, M. *et al.* An ultra-potent synthetic nanobody neutralizes SARS-CoV-2 by locking Spike into an inactive conformation. *bioRxiv* (2020) doi:10.1101/2020.08.08.238469.

62. Liu, L. *et al.* Potent neutralizing antibodies against multiple epitopes on SARS-CoV-2 spike. *Nature* **584**, 450–456 (2020).

63. Cao, Y. *et al.* Potent Neutralizing Antibodies against SARS-CoV-2 Identified by High-Throughput Single-Cell Sequencing of Convalescent Patients' B Cells. *Cell* **182**, 73–84 (2020).

64. Yuan, M. *et al.* A highly conserved cryptic epitope in the receptor-binding domains of SARS-CoV-2 and SARS-CoV. *Science* **368**, 630–633 (2020).

65. Pinto, D. *et al.* Cross-neutralization of SARS-CoV-2 by a human monoclonal SARS-CoV antibody. *Nature* **583**, 290–295 (2020).

66. Miersch, S. *et al.* Synthetic antibodies neutralize SARS-CoV-2 infection of mammalian cells. *bioRxiv* 2020.06.05.137349 (2020) doi:10.1101/2020.06.05.137349.

67. Noy-Porat, T. *et al.* A panel of human neutralizing mAbs targeting SARS-CoV-2 spike at multiple epitopes. *Nat. Commun.* **11**, 1–7 (2020).

68. Hansen, J. *et al.* Studies in humanized mice and convalescent humans yield a SARS-CoV-2 antibody cocktail. *Science* **1014**, eabd0827 (2020).

69. Wang, B. *et al.* Bivalent binding of a fully human IgG to the SARS-CoV-2 spike proteins reveals mechanisms of potent neutralization. *bioRxiv* 2020.07.14.203414 (2020) doi:10.1101/2020.07.14.203414.

70. Lv, Z. *et al.* Structural basis for neutralization of SARS-CoV-2 and SARS-CoV by a potent therapeutic antibody. *Science* **1509**, eabc5881 (2020).

71. Walser, M. *et al.* Highly potent anti-SARS-CoV-2 multi-DARPin therapeutic candidates. *bioRxiv* (2020) doi:10.1101/2020.08.25.256339 .

72. Cao, L. *et al.* De novo design of picomolar SARS-CoV-2 miniprotein inhibitors. *bioRxiv* (2020) doi:doi: 10.1101/2020.08.03.234914.

73. Miao, X. *et al.* A novel biparatopic hybrid antibody-ACE2 fusion that blocks SARS-CoV-2 infection: implications for therapy. *mAbs* **12**, e1804241 (2020).

74. Byrnes, J. R. *et al.* Competitive SARS-CoV-2 Serology Reveals Most Antibodies Targeting the Spike Receptor-Binding Domain Compete for ACE2 Binding. *mSphere* **5**, e00802-20 (2020).

75. Huo, J. *et al.* Neutralizing nanobodies bind SARS-CoV-2 spike RBD and block interaction with ACE2. *Nat. Struct. Mol. Biol.* **27**, 846–854 (2020).

76. Shi, R. *et al.* A human neutralizing antibody targets the receptor binding site of SARS-CoV-2. *Nature* **584**, 120–124 (2020).

77. Wrapp, D. *et al.* Cryo-EM structure of the 2019-nCoV spike in the prefusion conformation. *Science* **367**, 1260–1263 (2020).

78. Sharma, I., Wosińska, M., Kroetsch, A., Sullivan, H. & McClellan, M. *COVID-19 Manufacturing for Monoclonal Antibodies*. *Duke Margolis Center for Health Policy* (2020).

79. Daugherty, P. S., Chen, G., Olsen, M. J., Iverson, B. L. & Georgiou, G. Antibody affinity maturation using bacterial surface display. *Protein Eng.* **11**, 825–832 (1998).

80. Logtenberg, T. Antibody cocktails: next-generation biopharmaceuticals with improved potency. *Trends Biotechnol.* **25**, 390–394 (2007).

81. Baum, A. *et al.* Antibody cocktail to SARS-CoV-2 spike protein prevents rapid mutational escape seen with individual antibodies. *Science* **369**, 1014–1018 (2020).

82. Zanin, M. *et al.* An Anti-H5N1 Influenza Virus FcDART Antibody Is a Highly Efficacious Therapeutic Agent and Prophylactic against H5N1 Influenza Virus Infection. *J. Virol.* **89**, 4549–4561 (2015).

83. Asokan, M. *et al.* Bispecific Antibodies Targeting Different Epitopes on the HIV-1 Envelope Exhibit Broad and Potent Neutralization. *J. Virol.* **89**, 12501–12512 (2015).

84. Dong, J. *et al.* Development of multi-specific humanized llama antibodies blocking SARS-CoV-2/ACE2 interaction with high affinity and avidity. *Emerg. Microbes Infect.* **9**, 1034–1036 (2020).

85. Joshi, K. K. *et al.* Elucidating heavy/light chain pairing preferences to facilitate the assembly of bispecific IgG in single cells. *mAbs* **11**, 1254–1265 (2019).

86. Ridgway, J. B. B., Presta, L. G. & Carter, P. 'Knobs-into-holes' engineering of antibody C(H)3 domains for heavy chain heterodimerization. *Protein Eng.* **9**, 617–621 (1996).

87. Davis-Gardner, M. E., Alfant, B., Weber, J. A., Gardner, M. R. & Farzan, M. A bispecific antibody that simultaneously recognizes the V2-and V3-glycan epitopes of the hiv-1 envelope glycoprotein is broader and more potent than its parental antibodies. *mBio* **11**, 1–16 (2020).

88. Merchant', A. M. *et al.* An efficient route to human bispecific IgG. *Nat. Biotechnol.* **16**, 677–681 (1998).

89. Klein, C. *et al.* Progress in overcoming the chain association issue in bispecific heterodimeric IgG antibodies. *mAbs* **4**, 653–663 (2012).

90. Bönisch, M. *et al.* Novel CH1:CL interfaces that enhance correct light chain pairing in heterodimeric bispecific antibodies. *Protein Eng. Des. Sel.* **30**, 685–696 (2017).

91. Crawford, K. H. D. *et al.* Protocol and reagents for pseudotyping lentiviral particles with SARS-CoV-2 spike protein for neutralization assays. *Viruses* **12**, 513 (2020).

92. Pinto, D. *et al.* Cross-neutralization of SARS-CoV-2 by a human monoclonal SARS-CoV antibody. *Nature* **583**, 290–295 (2020).

93. Huo, J. *et al.* Neutralization of SARS-CoV-2 by Destruction of the Prefusion Spike. *Cell Host Microbe* **28**, 1–10 (2020).

94. Chi, X. *et al.* A potent neutralizing human antibody reveals the N-terminal domain of the Spike protein of SARS-CoV-2 as a site of vulnerability. *bioRxiv* 2020.05.08.083964 (2020) doi:10.1101/2020.05.08.083964.

95. Brouwer, P. J. M. *et al.* Potent neutralizing antibodies from COVID-19 patients define multiple targets of vulnerability. *Science* **369**, 643–650 (2020).

96. Wang, C. *et al.* A human monoclonal 1 antibody blocking SARS-CoV-2 infection. *Nat. Commun.* **11**, 2251 (2020).

97. Ke, Z. *et al.* Structures and distributions of SARS-CoV-2 spike proteins on intact virions. *Nature* (2020) doi:10.1038/s41586-020-2665-2.

98. Lui, I. *et al.* Trimeric SARS-CoV-2 Spike interacts with dimeric ACE2 with limited intra-Spike avidity. *bioRxiv* 2020.05.21.109157 (2020) doi:10.1101/2020.05.21.109157.

99. Rogers, T. F. *et al.* Isolation of potent SARS-CoV-2 neutralizing antibodies and protection from disease in a small animal model. *Science* **7520**, eabc7520 (2020).

Publishing Agreement

It is the policy of the University to encourage open access and broad distribution of all theses, dissertations, and manuscripts. The Graduate Division will facilitate the distribution of UCSF theses, dissertations, and manuscripts to the UCSF Library for open access and distribution. UCSF will make such theses, dissertations, and manuscripts accessible to the public and will take reasonable steps to preserve these works in perpetuity.

I hereby grant the non-exclusive, perpetual right to The Regents of the University of California to reproduce, publicly display, distribute, preserve, and publish copies of my thesis, dissertation, or manuscript in any form or media, now existing or later derived, including access online for teaching, research, and public service purposes.

DocuSigned by:
Katarina Pance
ED390912150A4A1...
Author Signature

12/6/2021
Date